Linear Atom Guides: Guiding Rydberg Atoms and Progress Toward an Atom Laser

by

Mallory A. Traxler

A dissertation submitted in partial fulfillment
of the requirements for the degree of
Doctor of Philosophy
(Physics)
in The University of Michigan
2013

Doctoral Committee:

Professor Georg A. Raithel, Chair
Professor Paul R. Berman
Assistant Professor Aaron E. Leanhardt
Assistant Professor Vanessa Sih
Professor Kim A. Winick

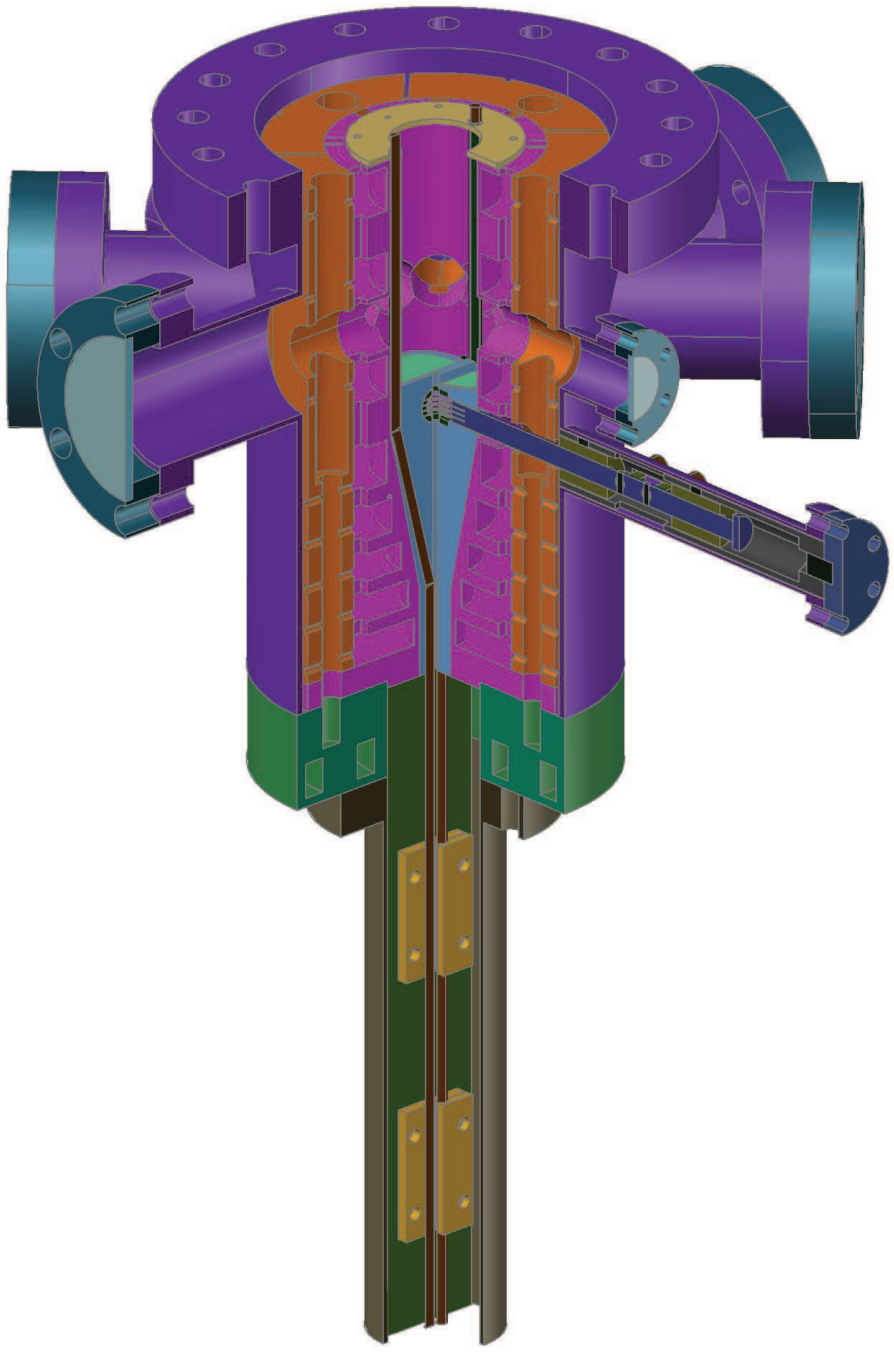

Cross section of the secondary MOT and magneto-optic injection unit.

For Alan, without whom this would not have been possible.

and

For Daisy, who has more lab experience than anyone else her age.

and

For #2, who helped me write.

ACKNOWLEDGEMENTS

I would like to acknowledge and thank the many people who have supported and encouraged me throughout my graduate school experience. First, I would like to thank my advisor, Georg Raithel. He allowed me to join the lab as an undergrad in the summer REU program, and welcomed me back to the group once I started grad school (which I likely was accepted to thanks to his letter of recommendation). Georg has an amazing sense of the lab equipment, the physics behind the observed phenomena, and often it seems like he performs magic in getting something to work. I would like to thank Aaron Reinhard and Tara Cubel Liebisch for getting me started in the lab while I was an undergraduate. Other labmates with whom I had discussions over my tenure as a grad student included Rui Zhang, Brenton Knuffman, Kelly Younge, David Anderson, Sarah Anderson, Andrew Schwarzkopf, Andrew Cadotte, Yun-Jhih Chen, Stephanie Miller, Kaitlin Moore, Nithiwadee Thaicharoen; postdocs Mudessar Shah and Betty Slama; and undergraduates Katie Crimmins, Robert van Wesep, Kareem Hegazy, Stefan Zigo, Tian Tian, Fei Wang, and William Huang.

Many thanks go to the people who worked on the Atom Laser project before me (Spencer Olson) or with me. Rahul Mhaskar and Cornelius Hempel taught me much about the workings of the lab. Melinda Morang spent a summer entertaining me with creative descriptions of what we saw on the screens together. Rachel Sapiro took over the project while I was on maternity leave. Erik Power generously shared many of the resources for his spiral guide, developed the DBR and TA laser systems that we both used, and set up the majority of the optics for guide β. Eric Paradis

headed the optical pumping portion of the experiments. I have been fortunate to have a series of wonderful undergraduates, without whom the project would not have advanced nearly as fast as it did: Varun Vaidya, Steven Moses, Karl Lundquist, and Matt Boguslawski.

I want to thank my parents, who have supported me in too many ways to count throughout my entire life. I ended many, many work days with a phone call to my Mom as I left the lab.

Most importantly, I want to thank my husband Alan for his support, encouragement, and love throughout the past several years. He has done and continues to do a wonderful job with our daughter Daisy, often taking on a majority share of the parenting duties throughout week.

This work has been supported by the Army Research Office. I also received individual support from an NDSEG (National Defense Science and Engineering Graduate) fellowship.

TABLE OF CONTENTS

LIST OF FIGURES

Figure

LIST OF TABLES

Table

LIST OF APPENDICES

Appendix

LIST OF ABBREVIATIONS

1MOT primary MOT for guide β

2MOT secondary MOT for guide β

BEC Bose-Einstein condensate

FI field ionization

IRFI initial remote field ionization

MCP micro channel plate

MI microwave ionization

MMOT moving magneto-optical trap (secondary MOT for guide α)

MOT magneto-optical trap

MS multichannel scaler

PI Penning ionization

PMOT primary (pyramidal) magneto-optical trap for guide α

RD radiative decay

RFI remote field ionization

TI thermal ionization

ABSTRACT

Linear Atom Guides: Guiding Rydberg Atoms and Progress Toward an Atom Laser

by

Mallory A. Traxler

Chair: Georg Raithel

In this thesis, I explore a variety of experiments within linear, two-wire, magnetic atom guides. Experiments include guiding of Rydberg atoms; transferring between states while keeping the atoms contained within the guide; and designing, constructing, and testing a new experimental apparatus. The ultimate goal of the atom guiding experiments is to develop a continuous atom laser.

The guiding of ^{87}Rb $59D_{5/2}$ Rydberg atoms is demonstrated. The evolution of the atoms is driven by the combined effects of dipole forces acting on the center-of-mass degree of freedom as well as internal-state transitions. Time delayed microwave and state-selective field ionization, along with ion detection, are used to investigate the evolution of the internal-state distribution as well as the Rydberg atom motion while traversing the guide. The observed decay time of the guided-atom signal is about five times that of the initial state. A population transfer between Rydberg states contributes to this lengthened lifetime, and also broadens the observed field ionization spectrum. The population transfer is attributed to thermal transitions and, to a lesser extent, initial state-mixing due to Rydberg-Rydberg collisions. Characteristic

signatures in ion time-of-flight signals and spatially resolved images of ion distributions, which result from the coupled internal-state and center-of-mass dynamics, are discussed.

Some groups [1] have used a scheme to make BECs where atoms are optically pumped from one reservoir trap to a final state trap, irreversibly transferring those atoms from one trap to the other. In this context, transfer from one guided ground state to another is studied. In our setup, before the atoms enter the guide, they are pumped into the $|F = 1, m_F = -1\rangle$ state. Using two repumpers, one tuned to the $F = 1 \rightarrow F' = 0$ transition (R10) and the other tuned to the $F = 1 \rightarrow F' = 2$ transition (R12), the atoms are pumped between these guided states. Magnetic reflections within the guide are also studied.

Design and construction of a new linear magnetic atom guide is detailed. This guide β has many improvements over the original guide α: a Zeeman slower, magnetic injection, a physical shutter, and surface adsorption evaporative cooling are some of the main changes. Testing of this new system is underway. It is hoped that the improvements to guide β will yield an atom density sufficient to reach degeneracy, thereby forming a continuous BEC at the end of the guide. The BEC, which will be continuously replenished by the atoms within the guide, will be outcoupled to form a continuous atom laser.

CHAPTER I

Introduction

Laser trapping and cooling of atoms has opened the physics world to a wide variety of experiments that were not previously possible. As such, the field of atomic, molecular, and optical (AMO) physics has gained much popularity of late, including the award of three physics Nobel prizes in the last fifteen years (1997, 2001, and 2012).

There are numerous exciting experiments within the overarching branch of AMO physics that utilize laser trapping and cooling. This thesis focuses on experimentally achieving a continuous atom laser, and also details some of the other experiments one can perform within a linear magnetic atom guide, somewhat linearly following the timeline of my experiences in the lab. We have three versions of magnetic guides in the lab, which I will refer to as guide α, guide β, and the spiral guide. The remainder of this chapter introduces several of the necessary ideas needed later on. Chapter II introduces the setup of guide α and includes discussion of the ion imaging method that we developed. It was already known that guide α is not capable of achieving the necessary atomic density for an atom laser. Therefore, experiments in guide α took a detour, first into the realm of Rydberg atom guiding (Chapter III) and then optical pumping (Chapter IV). Meanwhile, I designed and built guide β, which was not completed and tested until after the majority of these detour experiments took

place (funding and other such considerations came into play in the decision that I should focus on the detour experiments of guide α instead of completing guide β for quite some time). Therefore, Chapter V details the design and progress of guide β. The thesis concludes with Chapter VI about the current status and future plans of the Atom Laser experiment.

1.1 Introduction to Atom Laser

There have been many attempts to define what exactly is meant by the term "atom laser" [2, 3]. One characteristic that nearly every definition agrees on is that of coherence, both temporally and spatially. I narrow this down even further; my personal definition of atom laser is a continuous, coherent stream of atoms.

A continuous atom laser, with continuous-wave phase- and amplitude-stable coherent matter-wave fields, is formed by continuously and coherently extracting atoms from a Bose-Einstein condensate (BEC). Atom lasers have many similarities to the optical lasers that they were named after (somewhat incorrectly, since the "L" in the LASER acronym stands for light). The main similarity is a coherent output beam of bosons: photons in the case of optical lasers and de Broglie matter waves in atom lasers. One possible method–the one that we use in this work–for achieving a continuous atom laser is to begin with a magnetic atom guide and increase the phase space density of the atomic beam as it travels until it reaches degeneracy, forming a BEC that can be outcoupled. By mapping the evaporative cooling necessary to achieve BEC into space rather than time, it will be possible to realize a truly continuous BEC. Conventionally, BECs are created as a function of time. By spreading the process out in space, we will allow the atoms to have time to rethermalize between different physical locations in which the BEC steps occur, making the process more continuous than the standard method. In order to make a continuous atom laser, the BEC must have stable number statistics, meaning that it needs to be both phase- and

amplitude-stable. This is analogous to having a coherent state in an optical laser. With the correct output coupler, our system will provide continuous matter waves.

1.2 Applications of Atom Lasers

Though a continuous atom laser has not as yet been experimentally realized, there is a wide range of proposed applications once one is readily available.

1.2.1 Precision Measurement with Atom Lasers

Atoms, unlike their photonic counterparts, have mass. This gives atom lasers application abilities that optical lasers do not have, particularly in the realm of precision measurements.

Because of the small de Broglie wavelength of atoms in the velocity range of interest ($\lesssim$ 1 m/s to a few 10 m/s), atom interferometers [4, 5] are orders of magnitude more sensitive than their optical counterparts. Also, because atoms are particles, an interferometer utilizing an atom laser would allow for measurements that optical interferometers are not capable of performing. Relative phase shifts of the de Broglie matter waves could be used in an atom interferometer to measure atomic accelerations due to electromagnetic fields [6], gravitational fields [7], and interactions with other atoms [8, 9]. Some have proposed that atom lasers could also be used to measure changes in space-time, such as gravitational waves. To maximize the resolving power of an atom interferometer for use in these types of sensors, it will be necessary to operate the atom laser continuously (pulsed atom laser interferometry experiments have already been performed). Additionally, atom lasers could be used in precision measurement gyroscopes [10] or for atomic holography [11].

1.2.2 Manufacturing with Atom Lasers

Atom lasers could be used for many exciting applications in the manufacturing sector. One such prominent application is that of nanofabrication. Because alkali metals such as rubidium cannot be exposed to air, all such experiments must be done in vacuum. However, it has been shown that a combination of an alkali beam and self-assembled monolayers (SAMs) can be used, along with a contact mask with 50-nm scale holes, to etch a surface with ∼70 nm-wide features. In this type of experiment, the SAM acts as a resist. This has several advantages, including the manufacture of a wide variety of materials, as well as offering contrast enhancement. In [12], a beam of cesium was used to expose the SAM, forming a pattern onto the SAM surface. Subsequently, a wet-chemical etch was used to transfer the features onto the underlying surface. A similar process could be used with a beam of rubidium from an atom laser. Though the mechanism by which the alkali atoms alter the SAMs is not yet understood, it is possible that the atom laser beam would reduce the time needed to expose the SAM, since the atoms forming the atom laser would be more dense than the thermal beam used in previous experiments and therefore would achieve the same atom buildup on the SAM in less time. The fundamental resolution limit of this technology with a coherent beam of atoms would be the de Broglie wavelength of the atomic beam (for 10 m/s velocity, this is on the order of 1 nm).

1.3 Introduction to BEC

In order to create a continuous atom laser, one must first have a BEC. The experimental achievement of creating BECs was a highlight of AMO in the 1990s [13, 14, 15]. A BEC is a macroscopic collection of atoms that act like a single "super-atom" since all atoms occupy the same, lowest-energy, quantum state. For a BEC, the wavefunctions of the bosonic particles within the sample begin to overlap, which occurs when

$n\lambda_{\rm th}^3$ is of order one. n is the local number density and $\lambda_{\rm th}$ is the thermal de Broglie wavelength. This is given by

$$\lambda_{\rm th} = \sqrt{\frac{2\pi\hbar^2}{mk_BT}} \tag{1.1}$$

where m is the mass, k_B is the Boltzmann constant, and T is the temperature of the ensemble. The necessary phase-space condition is $n\lambda_{th}^3 \geq 2.612$ for free space and $n\lambda_{th}^3 \geq 1.202$ for a 3D harmonic trap.

A number of exciting BEC experiments have taken place over the years. Most fall into two categories: making BECs bigger or faster, or applications of BECs. Experiments on improving BECs include creating a BEC in a quadrupole-Ioffe trap [16], optical confinement of BEC [17], and creating a 2D BEC [18]. Applications of BECs include interference of BECs [19, 20] and pulsed pumping of a BEC [1], among many others.

1.4 From BEC to Atom Laser

A BEC is the starting point for an atom laser. The atoms within the atom laser beam are outcoupled from a BEC. Many experiments have taken place with pulsed atom lasers, and several research groups are working toward developing a continuous atom laser.

1.4.1 Pulsed Atom Lasers

Most pulsed atom laser experiments involve forming a BEC, outcoupling the atoms in some fashion, then allowing the atoms to fall under the influence of gravity. The first recorded occurrences of an atom laser used pulses of radio-frequency (RF) fields to flip the spins of some of the atoms within a BEC from magnetically trapped to untrapped states [21, 22, 23]. Later, pulsed Raman outcoupling was used to create

multistate atomic beams [24, 25]. The first-order [26] and second-order [27] temporal coherence properties have been measured. With RF outcoupling, the coherence of the condensate is preserved [28, 29], though it has been found that Raman outcoupling provides a higher continuous output flux than an RF-based coupler [30]. The divergence of an atom laser pulse has been measured [31]. There has also been a real-time measurement of an atom laser's flux [32]. The Gross-Pitaevskii equation has been used [33] to investigate the atom laser within the semiclassical mean-field approximation, and some groups have compared this approximation to experimental data [34, 22].

1.4.2 Continuous Atom Lasers

Our scheme for making a continuous BEC, and from that an atom laser, is to create a BEC at the end of the linear atomic guide. We will use the atoms within the guide to refill the BEC at the end, and cool them sufficiently as they traverse the guide so that they do not disturb the BEC when they arrive. The guide itself easily operates continuously; keeping the flow rates of atoms going from the guide to the BEC and atoms being outcoupled from the BEC in equilibrium should result in a continuous outcoupling of an atom laser. Optimizing the tunneling rate to outcouple the BEC to achieve this is analogous to determining the optimum reflectivity for an output mirror in an optical laser.

1.4.2.1 Other Proposed Schemes for Continuous Atom Lasers

Many schemes for making an atom laser involve some type of atom guide, since this spreads the BEC process out in space. There have been many versions of magnetic guides [35, 36, 37, 38], miniature magnetic guides [39], and hollow fiber guides [40]. Another popular approach is to make a BEC, then outcouple it into a guide [41]. Much work has been done on this front with regard to relatively small setups on

chips [42, 43, 44]. In order to have a chip-based atom laser, the chip must be relatively large in order to have enough time for the atoms to rethermalize [45]. Each of these methods has advantages and disadvantages, but none have actually produced a truly continuous atom laser as yet.

The best record that I have seen for a continuous atom laser is about 100 ms [46], in a method that uses a BEC in a dipole trap. A different group that has also made significant progress toward a continuous atom laser has a setup that involves two BECs, where they use one to refill the other, which is then outcoupled for their atom laser [47]. Having only two BECs in this configuration does not result in a continuous BEC (or atom laser), but it is possibly a step in the right direction.

1.5 Introduction to Rydberg Atoms

Efficient detection of atoms is crucial to all experiments that take place within an atom guiding configuration, especially those involving atom interferometry. Within a guide, an efficient means of detection can be that of ionization, as detailed in Chapter II. The need for efficient detection led us to consider using Rydberg atoms within our linear guide. Thus, Chapter III focuses on the guiding and dynamics of Rydberg atoms within the guiding geometry.

A Rydberg atom is one with a large principal quantum number, n, and as such exhibits some amazing properties. For all of this work, I used $n = 59$. The size of Rydberg atoms scales with n^2, so the $n = 59$ atoms used in my experiments are about 3500 times as large as their ground state counterparts. For a sense of scale, most viruses have radii in the 10s to 100s of nm and transistors in consumer electronics have diameters of about 180 nm [48], so with a radius of $\sim$185 nm the $n = 59$ Rydberg atom is bigger than either of these. With the valence electron so far away from the core of the atom, Rydberg atoms are very susceptible to electric fields, with the electric polarizability scaling as n^7.

The radiative lifetime of a Rydberg atom is the inverse of its total radiative decay rate. This lifetime is the time to decay from the Rydberg state to the ground state. Rydberg atoms exhibit long lifetimes on the order of $\tau \sim n^3$ for low angular momentum states and $\tau \sim n^5$ for high angular momentum states. These long lifetimes allow for significantly longer experimental times than are possible with ground state atoms.

Rydberg atoms strongly interact with other Rydberg atoms, and with blackbody radiation. Both of these phenomena, along with the Stark effect and field ionization, are examined in Chapter III.

Let us now move on to the details of the experimental setup.

CHAPTER II

Guide α Setup

To make an atom laser, our approach is to use a long, high-gradient, magnetic guide. We have three iterations of experimental apparatuses; this thesis will focus on the two linear guides (though part of the setup of the spiral guide will be covered when discussing the shared portions). I will refer to these two linear guides as guide α and guide β.

2.1 Introduction to the Experimental Setup

Guide α is the first guide in the lab [49, 50, 51]. It predates my graduate school tenure. Because the atomic density within guide α is not high enough to allow enough collisions to achieve a BEC, this apparatus is unable to form an atom laser. Hence, we used the best features of guide α and redesigned the shortcomings to make guide β. I will discuss guide β in depth in Chapter V.

In the following, I will detail the features of guide α's setup. The highlights are shown in Fig. 2.1.

2.1.1 MOTs

As with most BEC-type experiments, we use more than one magneto-optical trap (MOT) in our setup. In our case, we have two MOTs. The first MOT is often used to

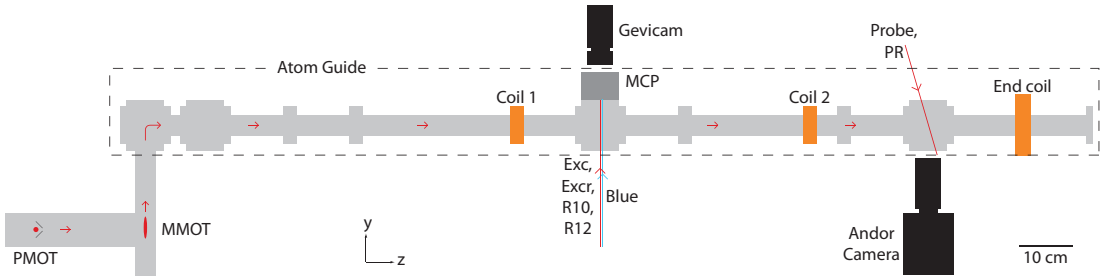

Figure 2.1: Overview of guide α. The guide is oriented such that gravity is in the $-y$ direction, so down in the figure is physically down. PMOT and MMOT are discussed in Section 2.1.1. Probe and PR, as well as the Andor camera, are discussed in Section 2.1.2. Exc and Excr are discussed in Section 3.2, along with the MCP and the Gevicam. R10 and R12 are discussed in Section 4.1. The use of coil 1, coil 2, and the end coil is discussed in Chapter IV. The dashed box indicates the horizontal section of the atom guide.

create a source of cold atoms to feed into the second MOT. Typically the first MOT does not have vacuum pressure that is as good as in the rest of the experimental chamber; often there is some kind of differential pumping stage between the two regions. The second MOT is typically at the location of the experiment for BECs made in time. We use the second MOT as a way to inject atoms into our guide.

Many lasers are used in getting the atoms into the guide. A level diagram with relevant transitions is shown in Fig. 2.2. This highlights the two detunings of the moving magneto-optical trap (secondary MOT for guide α) (MMOT) beams, as well as the repumper and the depumper.

Rubidium 87 atoms are first collected in a primary (pyramidal) magneto-optical trap for guide α (PMOT). The mirrors that compose the four walls of the pyramid reflect the laser light such that all needed beams to make a MOT are present. A schematic is shown in Fig. 2.3(a). Two trim coils, one on the vertical axis and one on the horizontal axis, allow the PMOT to be moved. Fig. 2.3(b) shows an image of the PMOT when it is moved away from the extraction hole at the apex of the pyramid. One spot is the actual MOT and one is a reflection image. In this non-extracted mode, the PMOT is large enough to be easily visible with the naked eye (to most

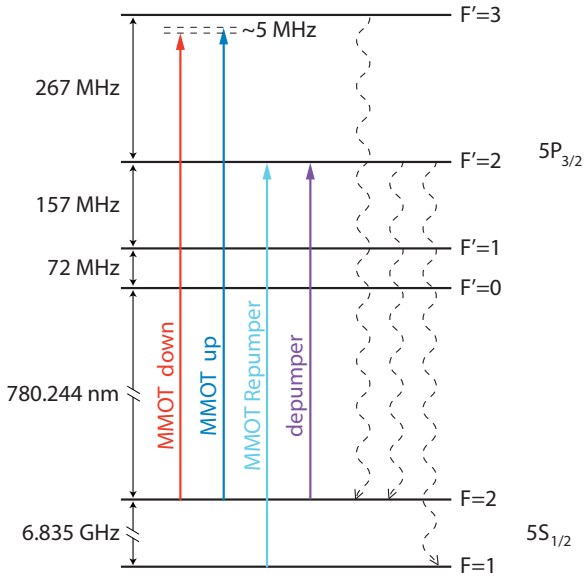

Figure 2.2: Level diagram for ^{87}Rb.

people).

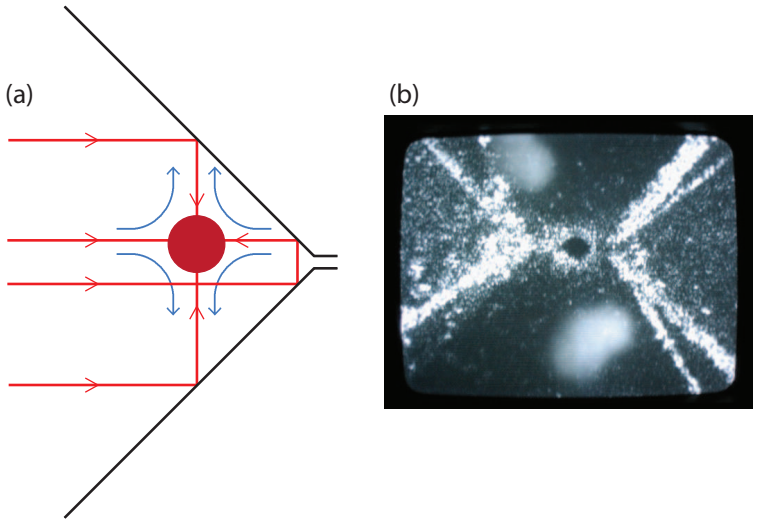

Figure 2.3: (a) Schematic and (b) an actual photograph of the PMOT.

Changing the current in the trim coils moves the PMOT over the extraction hole. The flux of atoms emitted from the PMOT was measured to be $\Phi_{\mathrm{PMOT}} \approx \times 10^9$ s^{-1} [49]. The atoms from the PMOT travel horizontally about 16 cm until they side-load the secondary MOT, which is a 2D+ moving MOT (MMOT). The transfer efficiency from the PMOT to the MMOT is about 16% [49].

The magnetic field for the MMOT comes from the guide wires themselves. At the location of the MMOT, the guide wires are separated by 3.7 cm, and the MMOT is located directly between them. This separation distance decreases throughout the length of the guide, to 1.5 mm surface-to-surface separation at the excitation point midway down the guide and 1.0 mm at the probing region at the end of the guide.

The MMOT is composed of four circularly polarized beams, each 45° from the vertical direction of the MMOT. By changing the detuning between the upgoing and downgoing beams, we create a moving frame of reference for the atoms cooling within the MOT. Standard MOT temperature is ∼150 μK. The downgoing beams have a slightly lower frequency than those of the upgoing beams; all are red detuned from the $5S_{1/2}\ F = 2 \rightarrow 5P_{3/2}F' = 3$ transition. The launch velocity (the velocity of the moving frame of reference) of the atoms, v_0, is controlled by changing the relative detuning of the beams,

$$v_0 = \frac{\epsilon\lambda}{\cos\theta} \tag{2.1}$$

where ϵ is half the frequency difference between the up and down beams, λ = 780.244 nm is the wavelength of the atomic transition and $\theta = 45°$ is the angle between the MMOT beams and vertical. We can operate the guide with launch speeds ranging from 2.2 m/s to 2.9 m/s.

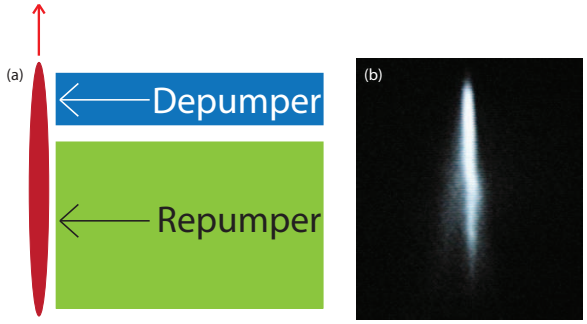

Figure 2.4: (a) Schematic and (b) an actual photograph of the MMOT.

Low-field-seeking atoms are trapped within the magnetic potential of the guide wires. As such, we use the $|F = 1, m_F = -1\rangle$ state for guiding our atoms. It is

one of three low-field-seeking states, as will be discussed in detail in Chapter IV, but it is the one that is dark to the stray light from the MOT. To place the atoms in $|F = 1, m_F = -1\rangle$, we use a depumper to pump the atoms into this state as they are leaving the MMOT (see Fig. 2.4(a) for a schematic). The top of the repumper and the bottom of the depumper are both cut off with a knife edge. At the location of the MMOT, there is about 1 mm vertically separating the two beams.

The atoms are launched upward for 20 cm before the guide wires bend at 90°, where the atoms then enter the horizontal section of the guide. We have to give the atoms enough velocity to traverse this bend; there is a critical velocity below which the atoms do not have enough energy to make it into the guide. Only about 1/3 of the atoms remain guided around this bend; a portion of the rest are recaptured by the MMOT. The vertical section was implemented to introduce some "gravitational slowing". Though gravity slows the atoms somewhat, the imparted velocity needed for the atoms to traverse the bend then must be counteracted if the atoms are to be slowed. Any velocity added from launching the atoms has to be removed as the atoms are cooled, but too many atoms are lost from the system by evaporatively cooling from such high velocities needed in this setup. This is addressed in Chapter V.

2.1.2 Optical Detection of the Guided Atom Flow

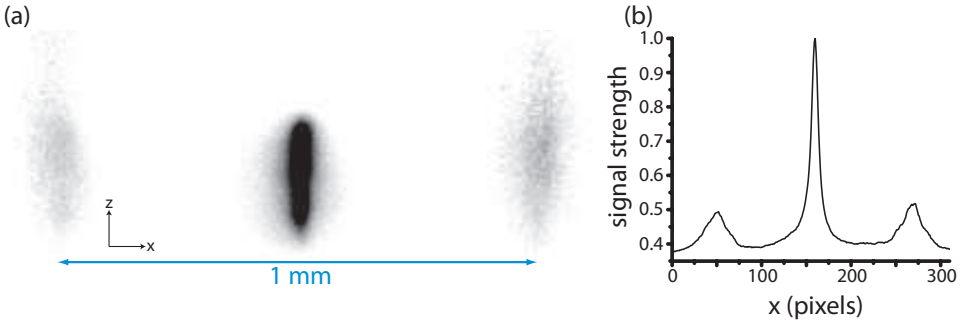

Figure 2.5: (a) Picture and (b) profiled trace from the end of the guide.

Once atoms are in the guide, we need a way to detect them. At the end of the

guide, we have an Andor iXon-DV887 camera. It is supposed to be capable of single-photon detection, though our signal is not quite that low. In this region, I use a probe ($F = 2 \rightarrow F' = 3$ transition) along with a probe repumper ($F = 1 \rightarrow F' = 2$ transition) to image the atoms. A sample image, along with the profiled trace of that image, is shown in Fig. 2.5. The side peaks are from light that is scattered from the atoms, illuminating the guide wires. The guide wires have a surface-to-surface separation of 1 mm at this location.

The detuning of the probe light and the magnetic fields that are present play off each other to affect the Zeeman splitting of the atoms. For example, if the end coil (shown in Fig. 2.1) is on, the probe needs a different detuning to be on resonance with atoms at the center of the guide. When the probe is not on resonance, we excite atoms in shells out from the center. Because of the way the atoms are imaged, this results in two bars of atoms in the picture.

2.1.2.1 Optimizing the Atoms in the Guide

We use the end-of-the-guide signal shown in Fig. 2.5 to optimize the flux of atoms within the guide. It is easier to optimize with the profile instead of the picture since it is more quantitative.

There are a large number of parameters that play into the guide performance, and the optimization procedure is quite iterative. Some of the optimization parameters include the lockpoints of the four lasers (see Fig. 2.6 and Table 2.1); the MMOT beam polarizations; the trim coils and the input mirror to the PMOT; the positions, polarizations and relative power of each of the MMOT beams; the launch velocity (Equation 2.1) of the MMOT; and the power in the MMOT repumper and depumper beams. Each of the four lasers is electronically locked to an atomic reference line. Drifts in the lockpoints cause instability in the atomic flow within the guide.

The Master laser is used for the red-detuned MMOT beams, the depumper, and

the probe (and the Exc, see Section 3.2). As seen in Fig. 2.6, changing the lockpoint of the Master laser affects the detuning of each of these. As such, it's one of the primary optimization parameters. If the lockpoint on the Master laser is adjusted, it affects the MMOT beam polarizations, which can then be adjusted with a half waveplate on each beam. Often the power in the MMOT beams, which is controlled in a Labview analog control program, also needs to be checked. Typically, we do not change the Master lockpoint enough to be greatly concerned about adjusting the probe frequency to compensate.

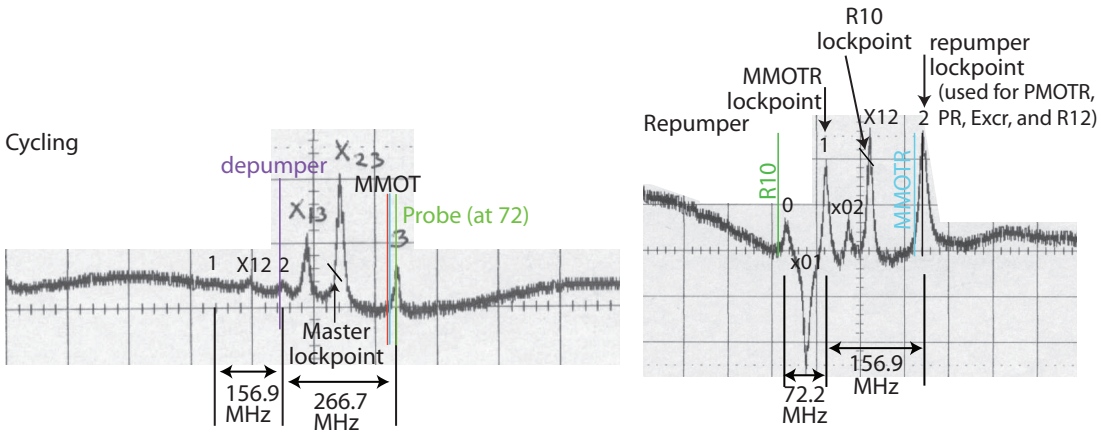

Figure 2.6: ^{87}Rb cycling and repumper spectra. The lockpoints for the Master, MMOT repumper (MMOTR), repumper, and R10 (explained in Chapter IV) lasers are marked, as well as the actual frequencies used in several parts of the experiment. X denotes crossover peaks, which occur halfway between actual peaks. For explanation of the different labels, see Table 2.1.

The MMOT is quite sensitive to differential radiation pressure from the four trapping laser beams. As such, I need to ensure that the power ratio of the up-going to down-going beams are approximately equal, and the splitting between each of those pairs is also equal. The circular polarization of the four beams is also important. To help stabilize these parameters, we added a quarter waveplate at the output of each of the two MMOT fibers. During the start of the day, I use both this quarter waveplate and the half waveplate to minimize the transmission through the beam cubes that

Label in Fig. 2.6	Explanation	Section introduced
depumper	The depumper laser.	2.1.1
MMOT	The two red-detuned MMOT lasers, which have a small difference in frequency on this scale.	2.1.1
Probe	The probe laser. (Also used as the Exc laser.)	2.1.2 (3.2)
R10	The R10 repumper laser.	4.1
MMOTR	The repumper for the MMOT.	2.1.1
PMOTR	The repumper for the PMOT.	2.1.1
PR	The probe repumper.	2.1.2
Excr	The excitation repumper.	3.2
R12	The R12 repumper laser.	4.1

Table 2.1: Explanation of labels in Fig. 2.6.

split the branches of the MMOT beams to set the quarter waveplates. Then I restore the half waveplates to approximately even splitting between the branches, finishing the half waveplate setting by watching the atoms at the end of the guide. This helps minimize the polarization drift of these two beams.

The DBR laser (used as the cycling transition for the PMOT) lockpoint, the position of the PMOT input mirror, and the magnetic field strength of the two PMOT trim coils all work together in affecting the position of the MMOT. Of these, the offset on the DBR lockpoint seems to have the largest effect on the guide performance and also drifts the fastest. While taking data, I have to monitor this lockpoint, often tweaking it a couple times an hour or more.

Beyond the connections that some of these parameters have (i.e. the Master lockpoint and the MMOT polarizations), some of the parameters seem to interact in unpredictable ways as well. To fully optimize the guide, it is useful to go through all the parameters multiple times, and in different patterns of the order of adjustment. Eventually the optimizations will have diminishing returns on increasing the guide performance.

2.2 Electric Field Control

As stated in the introduction and will be elaborated on in Chapter III, for some experiments we use Rydberg atoms within the guide. Rydberg atoms are extremely sensitive to electric fields, which polarize the atoms and cause electric dipole forces. The initially excited $59D_{5/2}$ levels exhibit the quadratic Stark effect, and dipole forces scale as $\alpha E \nabla E$, where α is the polarizability and E is the electric-field magnitude. Higher-angular-momentum states, which become populated through thermal transitions and collisions, have permanent dipole moments $\mathbf{p}$ and dipole forces $(\mathbf{p} \cdot \nabla)\mathbf{E}$. Since these forces may easily overcome the magnetic confinement force in the guide, we must minimize the electric field (and its inhomogeneity) during the free evolution of the atoms in the guide (i.e. before any ionization is applied). Estimates show that in the given electrode geometry and for levels in the vicinity of $n = 60$ the electric field must be kept below 1 V/cm for magnetic guiding to outweigh the electric dipole forces.

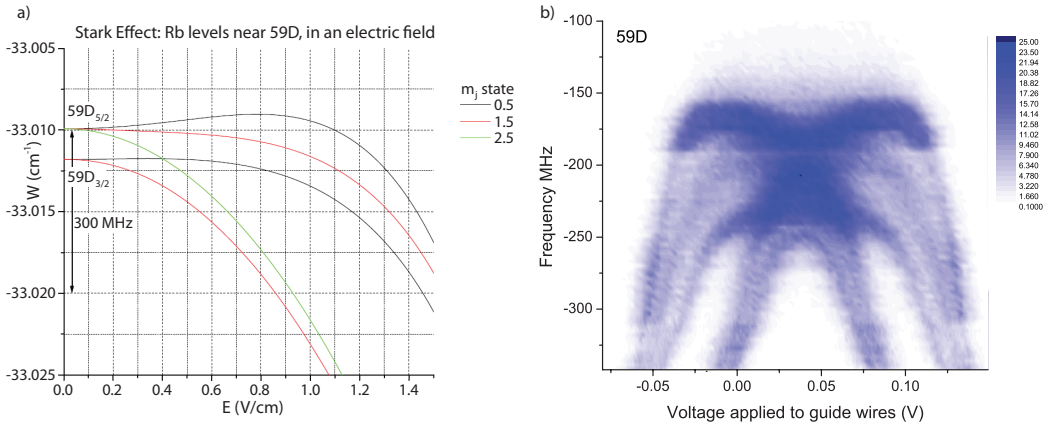

Figure 2.7: (a) Theoretical and (b) experimental Stark spectra for 59D.

The horizontal electric field, E_x, is homogeneous in lowest order and is tuned with a potential difference between the guide wires (surface-to-surface separation distance at the excitation point is 1.5 mm; see Fig. 2.9). To get an idea of the necessary applied fields needed to zero the electric fields, we can experimentally map out a

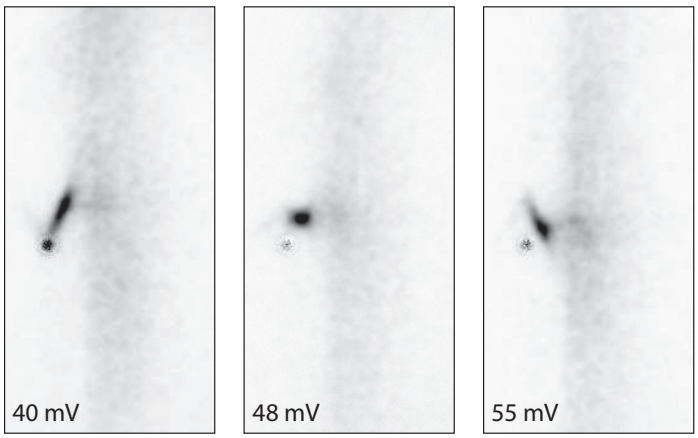

Figure 2.8: Ion images to determine the horizontal electric field zeroing. Here, I have shown three voltage steps that are easily discernable, though much finer steps were taken. The voltages listed were applied to both guide wires such that $V_{\text{left}} = -V_{\text{right}}$. This data was taken a few months after the Stark map shown in Fig. 2.7 and experimental conditions had changed slightly, therefore necessitating a higher applied wire voltage.

Stark spectrum. Figure 2.7 shows both a theoretical map and one from our guide. For this map, the vertical electric field was held fixed and the voltage applied to the guide wires was varied, such that $V_{\text{left}} = -V_{\text{right}}$, where $left$ and $right$ refer to the two guide wires. The theory plot and the experimental plot are in different units, but they are directly proportional so the maps have the same shape. To get from wavenumber in cm^{-1} to frequency, multiply by $c = 2.998 * 10^{10}$ cm/s. Electric field is directly proportional to the applied voltage, which is plotted on the horizontal axis of the Stark map. The line of symmetry in the experimental Stark map gives the needed condition to offset, and thereby zero, the electric field present in the system. In this plot, I would need to apply about 0.035 V to the left wire and -0.035 V to the right wire to zero the horizontal electric field.

The Stark map is a crude way to zero the electric field. With three electrodes on which to vary the potential, the process is very iterative. Figure 2.7(b) shows an example where the potential on two of the electrodes is varied. We can do much better than using this Stark mapping method. For $E_x \neq 0$, the ion image on the

micro channel plate (MCP) phosphor screen becomes strongly distorted, as shown in Fig. 2.8. By minimizing the angle of the ions imaged in the pictures, we zero E_x to within an uncertainty of 4 mV for the applied potential, since we can discern 2 mV steps in the images and we apply that voltage to each of the guide wires. This uncertainty is estimated based on the observed sensitivity of the image distortion to the potential difference between the guide wires. We do not address the z component of the electric field, since it is a reasonable assumption that it does not greatly change over the region of interest.

The vertical electric field, E_y, is harder to estimate and to control than E_x. Small changes of the potential applied to the vertical electrode produce significantly different potential shapes along the ion extraction trajectory; we will examine this more closely in Chapter III. We were able to experimentally find a condition that was most conducive to Rydberg-atom guiding, where the electric field and its inhomogeneity at the location of the atoms are small enough that electric-dipole forces do not inhibit Rydberg-atom guiding, and the signal ions originating within the atom guiding region are not blocked from passing through the vertical electrode. An electric-field calculation for this experimental condition shows an electric field of $E_x \approx 0$ and $E_y \approx 0.5$ V/cm at the location of the guiding channel. The electric field will be further discussed in the context of the Rydberg guiding data in Section 3.2.4.

2.2.1 Ion Imaging

The analysis of cold atomic beams in atom guides as well as the readout of atom-interferometric devices requires highly sensitive atom imaging and counting techniques. The fluorescence imaging methods used in the present experiment [49, 50] are well suited to characterize beams of guided ground-state atoms. However, all fluorescence imaging schemes are destructive to the atomic beam and not sufficiently sensitive to detect small numbers of atoms. (Fluorescence imaging can be sensitive to

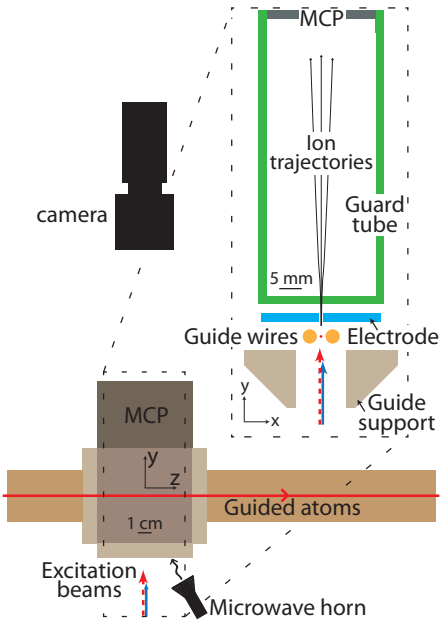

Figure 2.9: Schematic of the excitation and detection region in the two wire magnetic guide. The guided atoms (small red dot in the inset) travel between the guide wires, where they are excited into Rydberg levels with two lower (780 nm, dashed red arrow) and one upper (480 nm, solid blue arrow) transition beams. The Rydberg atoms are detected by microwave ionization (or field ionization). With the guide support grounded and the guard tube at −1.4 kV, ions are directed upward to a micro channel plate, where counts are recorded with both spatial and temporal resolution.

systems with few atoms, such as in a cavity.) While optical techniques are generally not useful to detect Rydberg atoms, state-selective electric-field ionization can be employed [52, 53]. With this technique, ions or electrons resulting from electric-field ionization are counted and/or imaged using charged-particle detectors. To that end, we have developed an ion imaging technique that works well in our linear atom guide. Using ion trajectory simulations as well as experiments, we study the passage of the ions through the detection system, the magnification of the detection system, and the time-of-flight characteristics.

Figure 2.9 shows the cross section of the excitation/extraction/detection region in the middle of the guide (for relative location, see Fig. 2.1). The wire diameter is 3.18 mm, with a surface to surface separation of 1.49 mm. The electrode is 1.59 mm

thick, with a slit width of 1.02 mm. The distance from the center of the guide wires to the top of the electrode is 4.76 mm, and the intermediate region between the electrode and the guard tube is 1.59 mm. The guard tube has a slit width of 1.59 mm. The distance from the top of the guard tube opening to the face of the MCP is 56.2 mm.

After the atoms are excited to Rydberg states, they must be ionized for detection. We can ionize with either a state-selective field ionization (FI) ramp, or with microwave ionization (MI). In some cases, which will be discussed in Chapter III, the atoms ionize without help from an applied ionization method. Potentials on the vertical electrode and ion extraction tube (see Fig. 2.9) direct the ions in the $+y$ direction and image them onto a micro-channel plate (MCP) detector, which has a detection efficiency of about 30% for impacting ions [54]. This efficiency mostly reflects the likelihood of the ions to hit the surface of the channels, and is significantly higher than other detection appliances such as photon multipliers. We control the delay time between excitation and ionization, t_d, to investigate the evolution of Rydberg atoms in the magnetic guide.

Each detected ion produces a countable pulse and a blip on a phosphor screen behind the MCP. We note that ion detection is necessary instead of electron detection (which would be done by reversing the imaging voltages) because the magnetic fields from the guide wires remain on throughout the entire experiment [55]. Over the relevant energy and magnetic-field range, the electron cyclotron radii are so small that in most spatial regions the electrons exhibit drift trajectories and largely follow the magnetic field lines of the guide-wire field. As a result, electrons generated by field ionization are channeled away from the electrode slit and the MCP detector even if the electrodes have potentials favorable to the detection of the electrons. Due to the heavy mass of Rb ions, the ion trajectories are only slightly deflected by the magnetic field.

After Rydberg atoms are ionized, the signal ions are extracted and imaged onto

the MCP detector. The ion counts on the MCP are recorded in two ways, allowing for both temporal and spatial analysis. A multichannel scaler (MS) distributes the counts into a number of time bins. At the same time, the MCP phosphor screen image is recorded with a GEViCAM GP3360_GEV camera. A few 10s of thousands of experimental cycles are averaged for both the MS traces and the images.

2.3 Ion Imaging Simulation

We found it useful to simulate the ion imaging setup introduced above. In the following, we characterize this atom detection method using ion imaging experimental data and ion trajectory calculations. In the simulation, the guide fields and ion-ion repulsion have been modeled in detail. The detection method is well suited for experiments on Rydberg atoms in magnetic guides, as will be seen in Chapter III.

The ion detection unit incorporates an extraction electrode (Electrode in Fig. 2.9) mounted 3 mm above the guiding channel of the magnetic guide formed by the two wires. In the following, we have simulated the ion imaging with the extraction electrode held at a variable, negative voltage (set to -1.4 kV for all data shown throughout the thesis). All ions created by photo-ionization are extracted quasi-instantaneously. A guard tube, held at a constant potential of -2 kV, shields the electric field created by the extraction electrode and defines an electric-field-free ion drift region near the MCP. Narrow slits (10 mm long by 1 mm wide) in both the electrode and guard tube allow the ions to pass through and be imaged on the MCP surface. In the following we define the z-axis to be parallel to the guide wires and the x- and y-axes to be as shown in Fig. 2.9.

2.3.1 Simulation Details

Varun Vaidya, an undergrad on this project, simulated the motion of the ions in our guiding geometry by first placing a collection of ions in between the guide wires,

then using a numerical integrator to calculate their trajectories in the presence of the magnetic fields of the guide, and finally mapping their final positions on the MCP detector [55]. In order to replicate realistic initial conditions, he placed 300 ions according to a cylindrically symmetric Gaussian spatial distribution with a standard deviation of 50 μm transverse to the guide axis, corresponding to the approximate diameter of the 480 nm photo-ionization beam. The initial momentum space distribution was assumed to follow a Maxwellian thermal distribution with a temperature of 400 μK along the transverse (x- and y-) axes and 1 mK along the guide (z-) axis.

The equations of motion for the ions were integrated using a fourth-order Runge-Kutta routine with a time step of 1 ns. The magnetic field of the guide wires, the electric field generated by the electrodes, and the electric field due to the ion-ion interactions were all taken into account when calculating the net force on each ion.

The Coulomb force on the jth ion due to the other ions was calculated using a pairwise sum over all particles,

$$F_j = \frac{q_j}{4\pi\epsilon_0} \sum_{i \neq j} \frac{q_i}{r_{ij}^2} \hat{\mathbf{r}}_{ij} \tag{2.2}$$

with ion positions $\mathbf{r}_i$ and $\mathbf{r}_{ij} = \mathbf{r}_j - \mathbf{r}_i$.

The magnetic field was calculated using the analytical expression for the field of two parallel current carrying wires, given by

$$B_x = \frac{\mu_0 I y}{2\pi} \left(\frac{1}{{r_r}^2} + \frac{1}{{r_l}^2} \right) \tag{2.3}$$

$$B_y = -\frac{\mu_0 I}{2\pi} \left(\frac{x - d/2}{{r_r}^2} + \frac{x + d/2}{{r_l}^2} \right) \tag{2.4}$$

where r_r and r_l are the distances between the ion and the right and left guide wires, respectively, and d is the center-to-center separation of the guide wires.

The electric potential in the region of the guide wires and the electrode was deter-

mined using an adaptive finite element algorithm implemented by Ansoft's "Maxwell" software. The electric field calculated from the potential was then exported onto a regular two-dimensional square mesh with a spatial resolution of 2.54 μm. The electric field due to the various electrodes at the position of each ion was interpolated from the mesh. Because this was a 2D mesh, the electric field is calculated only in the one plane, transverse to the guide wires. The simulation assumes that this electric field is the same for all z in the region of the slit. This is not entirely the case, since the $\pm z$ edges of the slit would contribute to a local electric field, but it is a reasonable assumption in the middle where the experiments take place. Due to the high resolution of the mesh, which was required to accurately model the ion dynamics near the edges of the electrodes, the overall extent of the mesh had to be cut off for practical reasons. This was possible because the electric field in the drift region (inside the guard tube) falls off sharply as a function of distance from the entrance slit. Once inside the drift region, the ions are not subject to a substantial force. We therefore cut off the electric-field grid inside the guard tube at a height of about 2 mm above its entrance slit. The electric field at locations above the grid cutoff remained below 10 V/cm, which was negligible for the present purpose. Therefore, once an ion reached the grid cutoff height, the final ion image location on the MCP was obtained in one step by linear extrapolation of the ion trajectory from the grid cut-off plane onto the MCP front plane.

2.3.2 Ion Imaging Behavior

Using the method described above, we have computed ensembles of ion trajectories for different (fixed) voltages applied to the extraction electrode. In the simulations, the MCP front plate and the guard tube are held at a fixed potential of -2 kV. To illustrate the focusing and magnification behavior of the ion imaging, the initial ion ensemble is spread out along the x-direction over a range of 100 μm, corresponding

to typical experimental conditions. A typical simulation result is shown in Fig. 2.10.

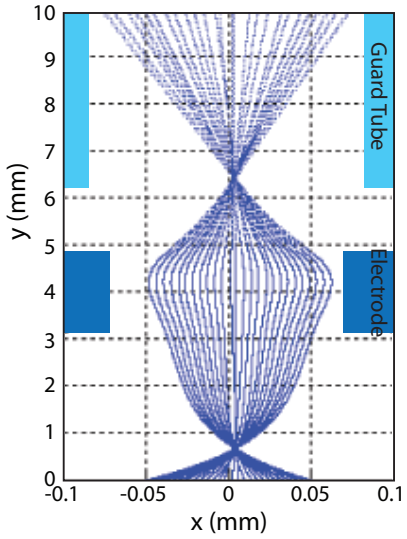

Figure 2.10: Ensemble of ion trajectories for an extraction electrode potential of -200 V and MCP potential of -2 kV. The slits in the electrode and the guard tube are indicated for orientation only and are not to scale (see Fig. 2.9 for an accurate depiction). Also, note the different ranges in the x- and y-directions. The plane of the guide wires is at $y = 0$ in this figure.

The slits in the guide rail, electrode and guard tube introduce a significant electric field component along the x-direction in the guiding and intermediate regions, as introduced in Section 2.2. The x-component of the field causes the width of the ion distribution along x to change as the distribution travels toward the MCP during extraction. Regions where the width of the ion distribution reaches a minimum correspond to the focal spots of the ion imaging system. The positions of the focal spots along the y-axis can be varied by changing the potentials of the electrode. Consequently, the setup behaves like a microscope with an adjustable magnification factor in x-direction. For the potentials used in Fig. 2.10, there are two intermediate focal spots, as can be clearly seen in the figure, and the x-magnification factor is about 15. Note that the MCP position is off the y-axis in Fig. 2.10; hence, the x-magnification is larger than it appears. Due to the (approximate) translational symmetry of the system in z-direction, the z-magnification factor is unity, regardless

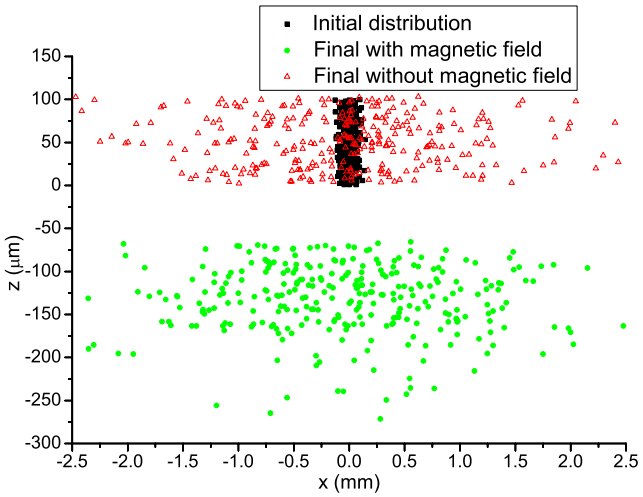

Figure 2.11: Sample of a simulated initial ion distribution in the xz-plane (black squares) and final ion distributions in the MCP detector plane with the guide magnetic field turned off (red triangles) and left on (green circles). The -150 μm average displacement and the spread of the detected ion positions in z-direction, observed in the field-on case, are due to the Lorentz force. Data such as these were used to determine x-magnification factors of the ion detection device. In this depicted simulation, the potentials for the extraction electrode and the MCP were -300 V and -2 kV, respectively.

of the detailed conditions.

As mentioned above, we image ions, not electrons. Since the ions have velocities that mostly point in the $+\hat{\mathbf{y}}$-direction due to the electric field produced by the electrodes, and since the guide magnetic field along the ion trajectories mostly points in the $+\hat{\mathbf{x}}$-direction, the Lorentz force results in an ion deflection in the $-\hat{\mathbf{z}}$-direction. Under typical conditions, the ion deflection only amounts to several 100 μm, as seen in Fig. 2.11, which shows top-down views of initial and imaged distributions under typical conditions. The ion imaging characteristics along the x-direction are not noticeably affected by the guide magnetic field.

The x-magnification factor of the ion distribution, M, is closely related to the position of the second focal spot along the y-axis and can be varied by altering the electrode potential. In Fig. 2.12, we show M vs the extraction electrode potential for a constant guard-tube potential of -2 kV. The figure shows that there are two

distinct regimes where the magnification behaves differently. For low absolute values of the extraction electrode potential, there are two focal spots, as seen in Fig. 2.10. The first focal spot, which is present under all conditions studied, occurs near the origin of the ion ensemble, at a height near $y = 1$ mm. The second focal spot forms within the range of the guard tube. As the absolute values of the extraction electrode voltage are increased, the second focal spot approaches the MCP, and consequently M decreases. At approximately -500 V, the second focal spot forms on the surface of the MCP, resulting in a very small magnification. For extraction electrode voltages more negative than -500 V, the second focal spot effectively forms above the MCP, and therefore acts as a virtual focal spot of the ion imaging device. The value of M begins to increase again and reaches approximately 15 at an extraction electrode potential of -1500 V. It is further noted that for voltages more negative than -500 V the image is inverted along the x-axis whereas for voltages between 0 V and -500 V it is not. In Fig. 2.12 we show experimentally obtained ion images in the various regimes, confirming the behavior of the x-magnification factor found in the simulations. Also, in the displayed experimental images a small field asymmetry leads to an offset of the average x-position of the detected ions. A comparison of the average x-positions in the regime of two focal spots (left picture) and the regime of one focal spot (right picture) with the case that the second focal spot lies in the MCP plane (middle picture) confirms the change in x-inversion behavior.

This transverse magnification factor is dependent on the y-height of the initial ion distribution relative to the plane of the guide wires. The effect of initial height, y_0, was investigated in simulations by choosing initial ion distributions of the type $P(x, y) = g(x)\delta(y - y_0)$, with a Gaussian $g(x)$ and varied values of the initial height y_0. Fig. 2.13 shows an approximately linear relation between y_0 and the magnification factor. The significance of the y_0-dependence of M in experiments is largely given by the vertical width of the initial ion distribution, which is of the order of the diameter

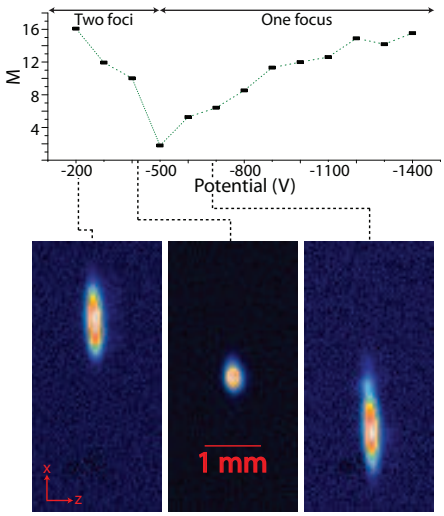

Figure 2.12: Top: the x-magnification M as a function of the extraction electrode potential. Bottom: experimentally obtained images of ion distributions for selected voltages. The experimental conditions were very similar to those of the simulation.

of the laser beams used for excitation. For a laser beam size of 25 μm, which is fairly straightforward to realize, Figure 2.13 indicates a variation of M over a range $13.4 \lesssim M \lesssim 13.8$ (*i.e.*, a 3% variation). This variation is small enough that it would not compromise most applications by having significantly different magnifications for atoms coming from different locations within the guide.

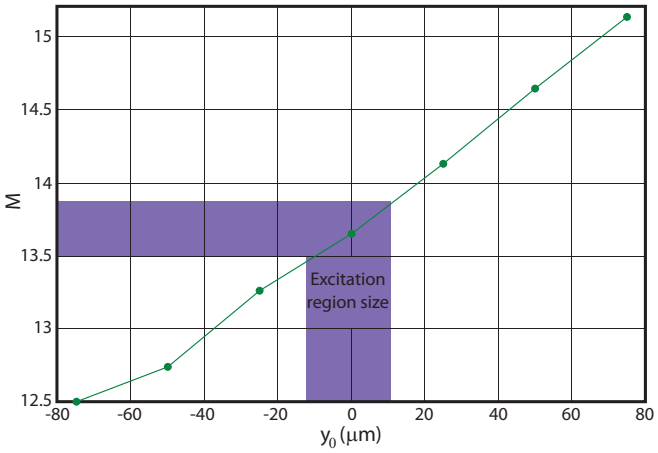

Figure 2.13: The x-magnification factor M as a function of the height of the excitation region.

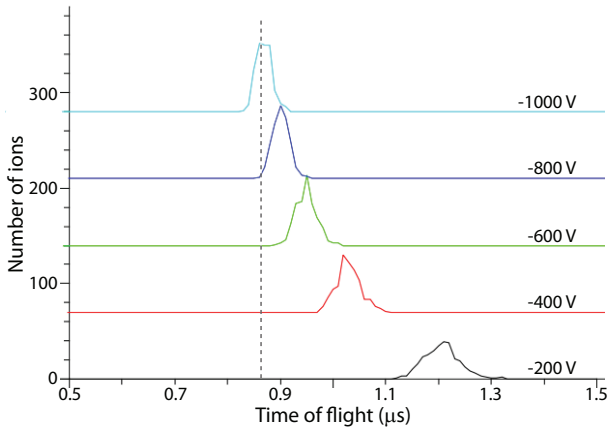

Figure 2.14: Simulated time-of-flight signals for the indicated potentials on the extraction electrode. The guard tube is held at -2 kV.

2.3.3 Ion Time-of-Flight Distributions

In applications of the ion imaging device, the average time-of-flight of ions (*i.e.*, the time elapsed between photo-ionization and arrival at the MCP image plane), will be useful to know. Due to the three-dimensional character of the ion distributions, we expect some dispersion of the times-of-flight; estimates of the time-of-flight dispersion will also be important. To study the time-of-flight characteristics, we use simulated initial ion distributions with Gaussian profiles in the x- and y-directions with a standard deviation of 100 μm and a uniform distribution along the z-axis. Several simulated time-of-flight distributions are shown in Fig. 2.14. Typical arrival times of the ions are on the order of 1 μs, with up to several 100 ns of dispersion. Ions closer to the electrode arrive earlier.

As one would expect, increasing the magnitude of the potential on the electrode reduces the time-of-flight of the ions to the MCP due to the increased initial acceleration of ions in the guiding region. For increasing magnitude of the extraction voltage, the average time-of-flight approaches an asymptotic value of 0.87 μs (for the given geometry). In the limit of very large, negative extraction voltage ($\lesssim -2$ kV), the extraction electrode generates a very deep potential well for the ions that pass

through it. The time-of-flight through the well has an asymptotic value of zero. Regardless of the detailed shape of that well, the ions slow back down to a kinetic energy of 2 kV while exiting the well and entering the guard tube (neglecting initial variations of potential energy). The time-of-flight is then mostly given by the 2 kV kinetic energy and the length of the tube, giving rise to the observed asymptotic behavior. For lower absolute values of the extraction voltage, the time the ions spend between the photo-ionization point and the guard tube, which adds to the asymptotic time-of-flight value, becomes significant and dominates the time-of-flight for extraction voltages between about -100 V and zero. Also, at low absolute values of the extraction voltage the dispersion becomes more significant, due to an increased effect of variations in initial conditions.

In the Rydberg guiding experiments presented in Chapter III, the extraction electrode is held at -1.4 kV. Therefore, extrapolating from Fig. 2.14, the average time-of-flight for the ions created in those experiments is less than a microsecond. This is low enough that it does not play a significant role in signal timing, but it is still useful to recognize that there is some spread in the time-of-flight distribution.

2.4 Conclusion to the Introduction

The information in this chapter prepares the way for the rest of the thesis. The photo-ionization and ion detection device can be easily adapted to detect Rydberg atoms in atom guides, and we use this method extensively in Chapter III. The experimental setup of guide α directly influences the Rydberg guiding data in the following chapter, and the optical pumping in the chapter after that. Guide β is strongly based on guide α, so this prepares the reader for Chapter V as well.

CHAPTER III

Rydberg Guiding

During the design and construction of guide β, we have used guide α to perform several new measurements on the guiding of Rydberg atoms. This has been a natural choice of experimentation due to the existing infrastructure present in the lab. In addition, in the past decade, several theory groups have published results on Rydberg atoms in strong transverse quadrupole fields. Our guide α presents an ideal platform in which to observe tightly-confined Rydberg atoms. As such, we studied the guiding of Rydberg atoms within the quasi-one-dimensional system of our linear atom guide, as well as the internal-state evolution of these Rydberg atoms.

3.1 Rydberg Guiding Introduction

Rydberg atoms have been capturing the interest of the scientific community since the 1920s. There has been a recent surge of interest in cold Rydberg atoms in a linear trapping geometry. Such systems present the possibility of creating one-dimensional spin chains by exciting atoms into high-lying Rydberg levels, which interact strongly due to their large dipole moments [56, 57, 58]. Rydberg crystals, which have been proposed in a frozen atomic gas using the Rydberg excitation blockade effect, may be an interesting application within a linear structure [59]. Entangled Rydberg atoms prepared in a linear guiding geometry could act as a shuttle for quantum informa-

tion [60, 61]. A one-dimensional trap or guide for Rydberg atoms could be used to further these types of research. Cold Rydberg atoms have been experimentally trapped using magnetic [62], electrostatic [63], and light fields [64]. Conservative trapping of Rydberg atoms conservatively trapped in magnetic atom guides has been theoretically investigated in [65, 66, 67]. Theoretical calculations also indicate the possibility of stationary Rydberg atoms confined in magnetic traps and magnetoelectric traps [68, 69, 70]. These systems would allow one to study Rydberg gases in a one-dimensional geometry. The Rydberg-Rydberg interaction properties in such a system have been theoretically studied in [71]. Trapped and guided Rydberg atoms are of interest in quantum information processing [72] and high-precision spectroscopy [73, 74, 75].

Waveguides built into chips are attractive setups for the linear guiding of atoms, and much experimental work ([76, 43, 77]) has advanced this type of research. With the capability of high magnetic gradients at low currents, such systems can be significantly smaller than macroscopic versions of magnetic guides. However, chip-based waveguides come at the price of having larger stray electric fields [78]. Though it takes much more physical space than an atom chip, we find that our large magnetic guide is a good environment in which to study the guiding of Rydberg atoms in a linear magnetic guide, which we have demonstrated [79].

In order to use a Rydberg guide for any sort of precise experiment, it is necessary to understand the dynamics of the Rydberg atoms within the guide. Rydberg atoms interact strongly with each other and with their environment. Within a magnetic guide, the Rydberg atoms experience conservative forces due to magnetic dipole moments interacting with the magnetic trapping potential. They also experience electric-dipole forces due to stray electric fields that may be present in the system. In Rydberg atom guiding and trapping at room temperature, thermally induced transitions from background radiation occur. In our high-gradient magnetic guide, demonstrated in [79],

this appears to be the dominant interaction, even though it occurs at rates that are not substantially faster than the initial state decay rate [80]. Energy exchange collisions, including the special case of Penning ionization, are also significant. Penning ionization has also been studied elsewhere, experimentally in [81, 82] and simulated in [83, 84]. Radiation induced and collision induced state redistribution effects can be studied using the methods of state selected field ionization, both using quasistatic electric fields [52] and microwave fields [85].

Using the linear magnetic guide discussed in the previous chapter, we set out to study the guiding of Rydberg atoms. We used the ion imaging techniques discussed to observe the Rydberg atoms over a period of 5 ms following excitation, where we could vary the delay time t_d between the excitation and the ionization. For this application, the potential on the extraction electrode is held near ground most of the time, so that the photo-excitation of Rydberg atoms and experiments on these atoms occurs under near-electric-field-free conditions. In the following sections, I will discuss the different ionization methods that begin the ion imaging process within the context of guiding Rydberg atoms.

3.2 Data Acquisition

The experimental timing is highlighted in Fig. 3.1. In particular, the $F = 1 \rightarrow F = 2$ excitation repumper (Excr) is pulsed on for 10 μs. Immediately following this, the excitation beam (Exc) is pulsed on for 5 μs. The tunable 480 nm blue laser is always on, exciting the atoms from the $5P_{3/2}$ $F = 3$ level to the Rydberg $59D_{5/2}$ level. The magnetic sublevels of the Rydberg state become approximately equally populated. The Rydberg-atom hyperfine structure is irrelevant. After a variable delay time between excitation and ionization, t_d, the Rydberg atoms are analyzed using either electric-field ionization or microwave ionization, with each ionization method highlighting different aspects of the Rydberg atom evolution.

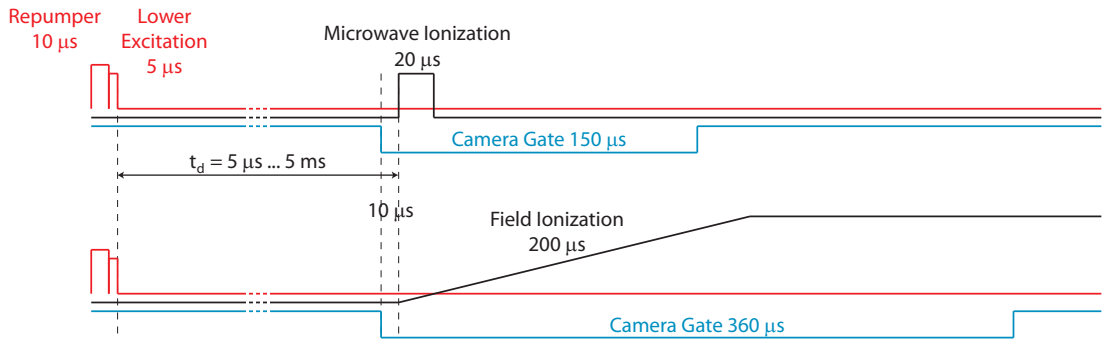

Figure 3.1: Experimental timing, including the gating of the MCP camera, for MI and FI.

After Rydberg atoms are ionized (whether by an applied ionization method or by one of the intrinsic phenomena that will be discussed later in this chapter), the signal ions are extracted and imaged onto the MCP detector as described in Chapter II. We estimate the MCP detection efficiency at 1.4 keV ion energy to be about 30% [54].

The ion counts on the MCP are recorded in two ways, allowing for both temporal and spatial analysis. A multichannel scaler (MS) distributes the counts into 2048 time bins. Most MS traces presented here consist of 50000 averages, except when $t_d \leq 500$ μs where we accumulate fewer experimental cycles to avoid saturation of the MS bins. At the same time, the MCP phosphor screen image is recorded with the Gevicam camera. 30000 images are averaged, then a background of the same number of images with the guide turned off is subtracted. A sample of each type of data is shown in Fig. 3.2.

As you can see in Fig. 3.2, there are a large number of phenomena occurring: Penning ionization (PI), thermal ionization (TI), initial remote field ionization (IRFI), remote field ionization (RFI), FI, and MI. The interplay between the different phenomena makes analysis particularly difficult. Gating the camera helps significantly; Fig. 3.3 shows how gating the camera over the applied ionization time (with timing as discussed in Fig. 3.1) greatly increases the clarity of the applied ionization signal (the MI and FI ions).

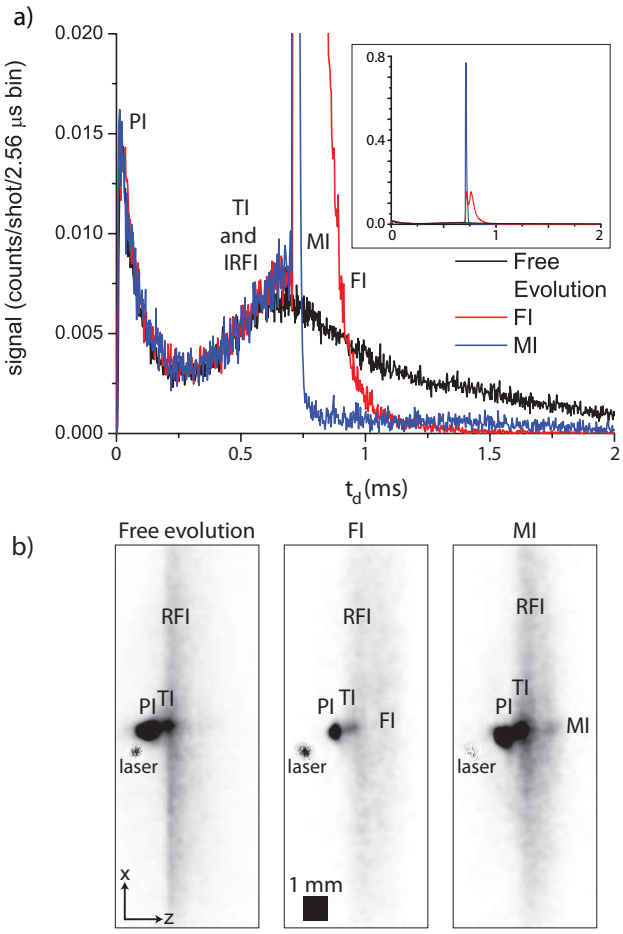

Figure 3.2: (a) MS traces for free evolution, FI, and MI. The inset is the same plot on a different scale to show the relative shapes of the MI and FI signals. (b) Corresponding MCP images, taken without having the camera gated over the ionization time. The abbreviations found in the figure are explained in the text.

The signal ions can be grouped into two classes. One class is due to interactions that are intrinsic to the Rydberg atom evolution as the atoms propagate along the guide, and occur even in the case of free evolution when no ionization field is applied. The intrinsic processes are PI, TI due to background blackbody radiation, and RFI (which we further distinguish into IRFI and delayed RFI; the difference between these will be addressed in Section 3.2.1, in the discussion of Fig. 3.4). RFI occurs when Rydberg atoms transition into magnetically unguided states at some point during their evolution. A fraction of these atoms moves into regions of large electric field,

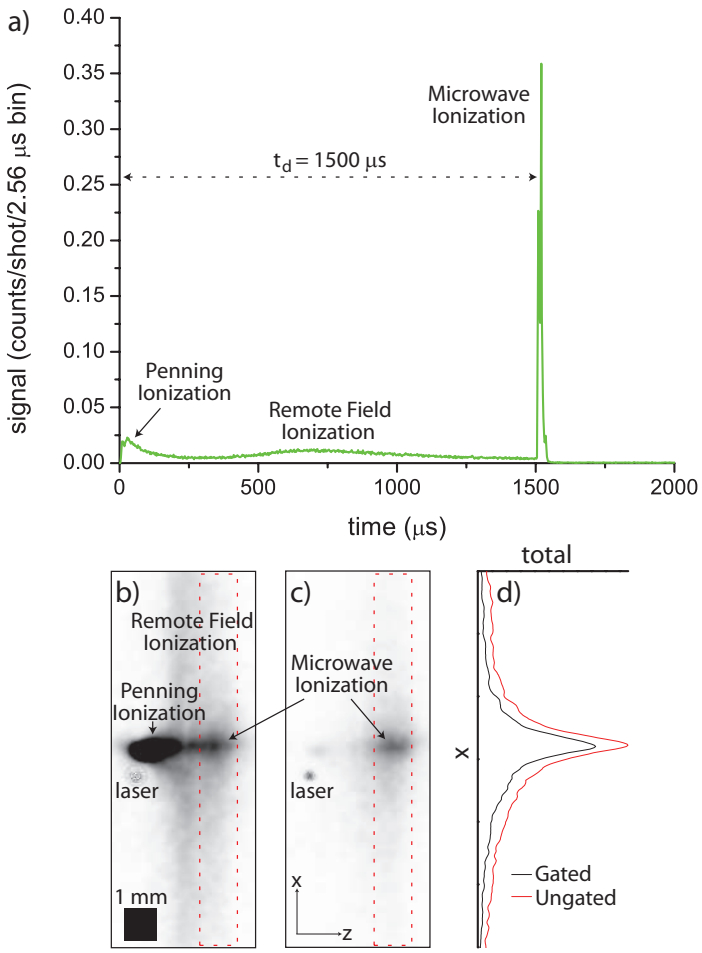

Figure 3.3: (a) MS trace of MI, at $t_d = 1.5$ ms. MCP image with a delay time of $t_d = 1.5$ ms, with (b) camera on throughout the experimental cycle and (c) camera gated over the microwave ionization signal. The black square indicates 1 mm^2 in the image plane. The images exhibit a remnant of laser light penetrating through the MCP and phosphor screen. (d) Profiles of each, from the regions indicated by the dashed boxes.

thereby ionizing and producing a widely-dispersed ion signal. The second class of signal ions is due to the applied processes of FI and MI, which lead to information about the internal-state Rydberg atom distribution at the delay time t_d. This t_d is shown visually in Fig. 3.1. The FI (red) and MI (blue) traces in Fig. 3.2(a), respectively, show that the intrinsic processes occur until the delay time t_d when either field or microwave ionization is applied. The applied ionization methods terminate the free evolution and deliver a picture of the Rydberg-atom state distribution and

the number of Rydberg atoms present in the guide at the instant when the ionization is applied. The data from varying t_d gives us insight into the evolution of the Rydberg atoms' internal states while traveling within the guide.

3.2.1 Free Evolution

Temporal data is collected in the form of MS traces, allowing us to study the distribution of counts as a function of time. The spatial and temporal signal of the different intrinsic processes (PI, TI, IRFI, and RFI) that occur within the guiding system allow us to study the free evolution of the Rydberg atoms without any applied ionization. This case is represented by the black trace in Fig. 3.2. The strong signal component that peaks shortly after excitation and lasts for $\sim$50 μs is due to PI. A minimum in counts occurs around 250 μs, then the IRFI signal begin to increase, peaking around 700 μs. When I integrate the FI signal and the free evolution signal, the signal yield due to FI is about three times as much as the signal yield from the free evolution. The other atoms are not detected unless ionization is applied. Thermal ionization begins immediately and trails off, but it is such a relatively small signal it is not discernable in the MS traces.

In ungated images (such as those shown in Fig. 3.2), the spontaneous processes of PI, TI, and RFI, as well as the imperfectly subtracted excitation laser spot, are visible in the images for free evolution, field ionization, and microwave ionization. To better focus on the applied ionization signals instead of the spontaneous signals, we gate the MCP camera over the time of the applied ionization as shown in Fig. 3.1. In the gate timing, it is important to factor in the ion times of flight and the fluorescence decay of the phosphor screen. Our ion times of flight range from 3 to 25 μs, peaking at 10 μs. These long ion times of flight reflect the small electric fields present in the atom guiding region during the free evolution time interval. The fluorescence lifetime of the phosphor screen is $\approx$ 50 μs, according to manufacturer specifications.

We set the gate to range from just before the beginning of the microwave pulse or field ionization ramp to 150 μs beyond their respective ends. Both gated and ungated images were taken at all experimentally used t_d for comparison.

In Fig. 3.3 we compare (b) an ungated and (c) a gated image, both taken at a microwave ionization delay time of $t_d = 1.5$ ms. The dominant feature on the far left in the ungated picture is due to Penning ionization, which is a likely outcome of the collision of two Rydberg atoms where one Rydberg atom ionizes and the other's n value is decreased. Penning ionization can be expressed by

$$\mathrm{Ry}(n_0) + \mathrm{Ry}(n_0) \rightarrow \mathrm{Ry}(n) + \mathrm{ion} + e^-, \tag{3.1}$$

with n_0 and n denoting the initial and final principal quantum numbers, respectively. We estimate that about $\sim$10% of detected ions are in this Penning ionization signal. This number varies with fluctuations in Rydberg atom density. Since each Penning collision involves a detectable ion as well as a second atom that transitions to a lower n state, about $\sim$20% of all Rydberg atoms created are involved in Penning ionization.

The presence of Penning ionization in our low-density Rydberg atom system might appear surprising. The Penning ionization rate is dependent on density (2×10^{14} m^{-3}), thermal velocity (on the order of 0.4 m/s), and collision cross sections (on the order of 2×10^{-12} m^2 for $n = 59$) [86, 81, 87, 88, 89]. Using these values and noting the time during which the sample is relatively dense (on the order of 100 μs), we estimate Penning ionization probabilities that are indeed in line with our experimental observations. With our time resolution it is impossible to distinguish between rapid sub-μs ionization (autoionization) and PI events picking up after a few microseconds of motion when collisions start to happen (such a distinction was made in an experiment in Ref. [90]). Further, due to energy conservation, the principal quantum number of the product atoms has to be less than $n_0/\sqrt{2}$, where n_0 is the initial principal

quantum number. Since n is decreased by $\sqrt{2}$, the electric field needed for ionization is increased by a factor of 4. Therefore the product atoms are out of range of our state selective field ionization ramps, rendering them undetectable in our system. The presence of Penning ionization suggests a level of density that indicates other non-ionizing, n-changing and ℓ-changing collisions are also present in the system.

In addition to PI, many counts from RFI are also visible in the ungated images. The profiles in Fig. 3.3(d), taken by integrating Figs. 3.3(b) and (c) over the regions indicated by the dashed boxes, show that the gating removes about 17% of the signal near the microwave ionization peak and more than 50% in the wings. Therefore, in the ungated image the signal in the peak is mostly due to microwave ionization, whereas a large fraction of the signal in the wings is from the remote field ionization signal. The benefit of the camera gating procedure primarily is to remove the majority of the remote field ionization signal, except for where the RFI signal overlaps in time with the camera gate (see Fig. 3.1). The Penning ionization signal is also removed from the gated images, though this signal does not spatially overlap with the microwave ionization signal.

The above analysis of the entire signal in Fig. 3.2 and the further discussion in Fig. 3.3 is still incredibly complicated. Since the signals from a number of different processes are superimposed in the ion images and in the MS traces, the analysis of the Rydberg-atom evolution in the guide is non-trivial. It is necessary to use both the temporal (MS trace) and spatial (ion image) information to understand the processes involved. To assist in understanding which phenomena are represented by the various signals found in the MS traces and MCP images, in Fig. 3.4 I have individually sketched the MS traces and ion images of all of the signals that occur.

The top image in Fig. 3.4 is a flow chart of the various phenomena. It also serves to highlight the close correlation between internal-state dynamics and center-of-mass propagation of Rydberg atoms in the magnetic guide. Solid lines indicate bound

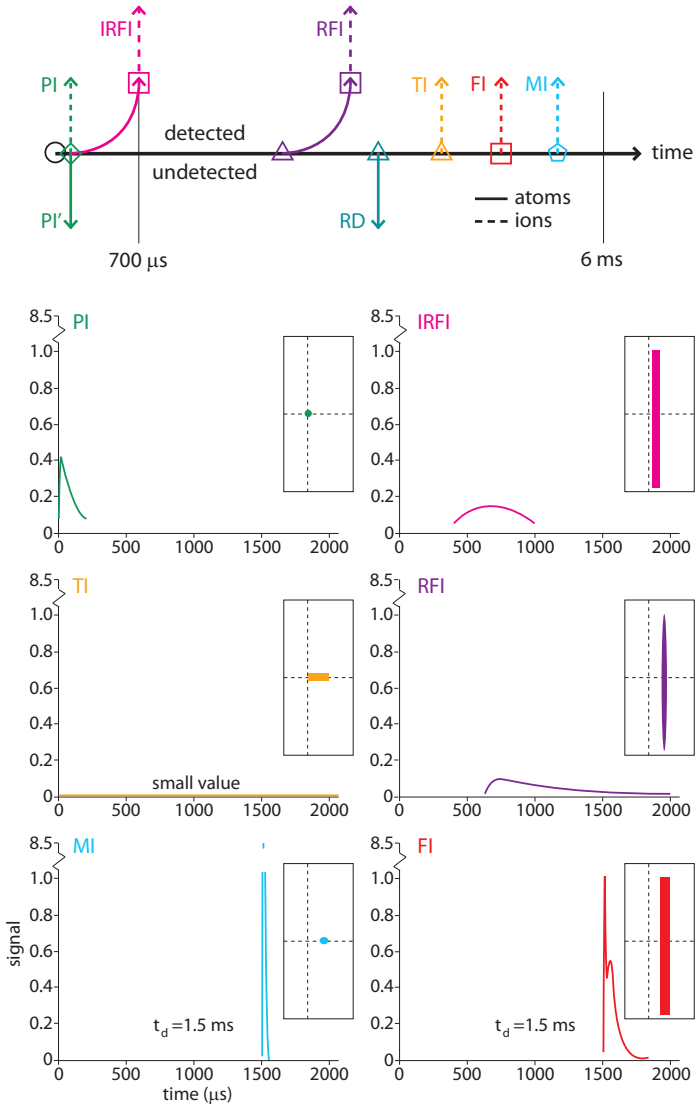

Figure 3.4: The top diagram is a flow chart of processes affecting Rydberg atoms prepared within a magnetic atom guide, rendered in the (t, y)-plane with y as in Fig. 3.5 below. Atoms are excited at time $t = 0$, indicated by the ◯. Solid lines indicate bound Rydberg atoms and dashed lines indicate signal ions. Lines below the axis are atoms and ions that are undetectable in our system. Below that, I have sketched the MS traces and MCP images associated with the different processes, taking care to keep the sketches to scale.

Rydberg atoms, while dashed lines represent signal ions. Signals below the time axis are not detectable with our system. The time of excitation is indicated by ◯. Symbols on the trajectory arrows indicate the type of event by which the signal arises: the ♢ is Rydberg-Rydberg atom collisions, the △s are thermal transitions, the □s

are electric field ionizations, and the ⬠ is microwave ionization.

At the excitation time (◯ in Fig. 3.4), samples of ∼100 Rydberg atoms are prepared in the guide. About half of them are in high-magnetic-field-seeking states, and are expelled immediately from the guide. A fraction of those move up along the y-direction, approach the strong electric field present in the slit in the vertical electrode, become field ionized and produce a signal that we refer to as the IRFI signal. The IRFI signal is widely dispersed in x-direction, because the points of origin of the corresponding ions are spread out across the x-width of the slit in the vertical electrode. The arrival time of the IRFI signal at the MCP is governed by the time it takes for high-field-seeking Rydberg atoms to move close to the vertical electrode, where they ionize; the additional time of flight of the ions to the MCP is negligible. The IRFI signal peaks at about 700 μs after excitation.

The initial Rydberg atom density is sufficiently high that PI also occurs. PI' indicates the atoms that are shifted to lower n values (with $n \leq n_0/\sqrt{2}$), thereby becoming undetectable in our system. We know that for every ion detected in the PI signal, another atom was involved in the corresponding undetectable PI' signal, since each Penning collision involves a pair of atoms. In the MS traces, the PI signal is limited in time to less than ∼200 μs after excitation; after that time the sample density becomes so low that PI ceases. This is sketched in green in the bottom section of Fig. 3.4. Since the production of PI ions is highest immediately after excitation and because the ion time of flight from the atom guide location (symmetry axis between the guide wires) to the MCP is only on the order of a few tens of microseconds, the PI signal peaks very early. Further, the ions originating from the atom guide plane (i.e., the plane formed by the guide-wire axes) are imaged into a tight, concentrated spot in the ion images. This is also sketched in the figure.

Due to the long evolution time in our system, the most prominent interaction of the Rydberg atoms is the relatively strong interaction with background blackbody

radiation [91, 92, 93], making thermal radiation the most important phenomena affecting the internal states of the guided Rydberg atoms. Thermal transitions within the bound-state space of the Rydberg atoms cause a diffusion-like behavior in all quantum numbers, as well as thermal ionization. Since our guide operates at room temperature, these internal state dynamics and thermal ionization are the dominant features at long interaction times. The resulting effects are, in decreasing order of importance, bound-bound transitions into nearby Rydberg states, TI, and thermally enhanced radiative decay (RD) into low-lying atomic states. The Rydberg atoms that radiatively decay into low-lying atomic states are not detected (RD in the top of Fig. 3.4, not shown in the sketched MS traces since not detected). These TI and RD events occur throughout the evolution time, but for clarity of the flowchart are only sketched at one location.

Rydberg atoms present in the guide produce a weak ionization current due to TI in the 300 K background radiation of the guide (yellow in Fig. 3.4). This signal is so weak that it cannot be discerned in the MS traces, though it is actually present. However, since all TI ions are generated near the atom guiding channel, the corresponding signal in the ion images is quite concentrated (similar to the PI signal). Hence, TI produces a faint stripe in the ion images with little extent in the x and some extent in the z-direction. The overall TI probability is so small that TI results in the weakest signal. Though it is weak, the TI signal has the longest duration, beginning at ionization and continuing throughout the experimental time scale.

Guided Rydberg atoms continue to interact with thermal radiation, and transitions of guided Rydberg atoms into magnetically unguided states occur at a certain rate until there are no Rydberg atoms remaining in the guide. Atoms that are guided for some time and then transition into a high-magnetic-field-seeking state follow a similar path to those causing the IRFI signal. The resultant RFI signal is delayed by the amount of time the atoms were actually guided. This delayed RFI signal starts

to appear around ∼700 μs and slowly tails off throughout the rest of the observed time.

3.2.2 Microwave Ionization and Field Ionization

Things get more interesting when we start to apply microwave or field ionization. As seen in the MS trace in Fig. 3.2, MI and FI each completely overwhelm the free evolution signals (thereby terminating the free evolution processes).

The Rydberg atoms are probed by microwave ionization with a microwave pulse of 20 μs duration and 18.5 GHz frequency. The microwave pulse is generated with an Agilent MXG Analog Signal Generator and amplified with a 6-18 GHz microwave amplifier. Since our frequency is just outside this range, the amplifier likely does not work quite as well as specified, but it is sufficient for the needs of this experiment. The amplifier is connected to a microwave horn, which is located at a slight angle to the excitation beams, at the viewport beneath the MCP (for location, see Fig. 2.9). The microwave pulse is applied at a variable delay time t_d and ionizes >90% of the Rydberg atoms. A typical MI trace is shown in the blue curve in Fig. 3.2, for t_d = 0.7 ms. After ionization the free charges are decoupled from the microwaves; *i.e.* the ions are no longer affected by the microwave field due to their vanishing ponderomotive energy and quiver amplitudes in the microwave field.

Alternatively to MI, we can use static field ionization and apply an ionization ramp starting at t_d. The potential on the electrode, identified in Fig. 3.5, is linearly decreased to −220 V over a duration of 200 μs beginning at t_d. This corresponds to an electric field ramp that peaks at 110 V/cm at the location of the atomic beam. At the end of the ramp the electric field is held at the maximum value for 500 μs. We set the voltage on this electrode with a programmable function generator that feeds into a home-built high-voltage amplifier that I assembled. A typical FI trace is shown by the red curve in Fig. 3.2, where t_d = 0.7 ms. Since the rise time of the applied

field ionization ramp is fairly long the distribution of counts along the time axis in the MS traces allows us to extract the distribution of ionization electric fields of the Rydberg atoms present in the guide. The latter can be mapped to internal state distribution using the known dependence ($1/16n^4$) of the ionization electric field on the principal quantum number. This is addressed further in Section 3.5, particularly with the discussion of Fig. 3.12.

The relative peak heights of the various MS traces is sketched in Fig. 3.4. I normalized the signal heights in the sketched MS traces to the highest FI peak. The MI signal peaks at $\sim$8.5. Both the MI and FI traces (for a given t_d) integrate to about the same value indicating the same number of Rydberg atoms detected, but the MI signal is significantly more compact temporally than the FI signal. Comparatively, the intrinsic signals are all fairly low in signal strength, all peaking somewhere in the $\lessapprox 0.4$ range.

Both MI and FI ionize nearly 100% of the Rydberg atoms that are in the guide. Due to the electric fields present, all of these ions are directed upward to the MCP for detection. Thus, the Rydberg atom detection efficiency for either of these methods is that of the known MCP detection efficiency, 30%. Atoms that transition to high-field-seeking states are expelled from the guide in all directions. Statistically, half will have a $-y$ component in their expulsion trajectory, thereby being lost from the system. The half with the $+y$ component become the (I)RFI signals. Therefore, we expect a detection efficiency of $\sim$15% for (I)RFI. Detection for PI and TI will not be quite as good as for MI and FI, but it is reasonable that it should be much better than that of (I)RFI.

3.2.3 Image Magnification

In the following I provide additional information that was important in arriving at the above interpretation of the data. In analyzing the various signal components

in the images, it is important to understand the ion imaging properties of the system. For all cases, the longitudinal magnification of the ion images is $M_z = 1$. Because the atoms are moving in the guide, there is a direct correlation between space in the z-direction and time. The ramped electric field of the FI case deflects the ions horizontally on their way to the MCP for detection. This deflection is not present with MI, or any of the other free ion signals. For this reason, we have an x-axis resolution on the CCD camera of 24 ± 3 μm/pixel for free ions (PI, TI and MI) and 6.0 ± 0.3 μm/pixel for FI. These refer to distances in the object plane. The resolutions are determined by moving the excitation beam by a known amount and measuring the resultant displacement in the image. This corresponds to transverse magnifications of $M_{PI} = M_{TI} = M_{MI} = -1.6\times$ and $M_{FI} = 6.6\times$. Because the exact route by which ions due to RFI (and IRFI) arrive at the MCP is unknown, the magnification of the RFI signal cannot be easily determined, but $M_{RFI} = M_{IRFI} > M_{PI}$ and is probably close to M_{FI}. We also note that due to the finite size of the MCP the wings of the RFI and FI signals are slightly cropped. The negative magnification in the case of free ions comes from an intermediate focus in the ion imaging, as simulated in [55]. The difference in magnification is clearly seen in Fig. 3.9(b) below in Section 3.4, which shows gated images for FI and MI at various t_d.

The TI and RFI are distinct in the ion images due to their significantly different magnifications, though they temporally overlap and are thus indistinguishable in the MS traces. This manifests in the images as the TI and RFI signals having the same z coordinate but quite different extents in x. The TI signal appears as a much narrower streak within the transversely-spread RFI counts.

3.2.4 Electric Field's Effect on Data

As introduced in Section 2.2, the electric field present in the system greatly affects the data. Here, I will go into more detail about the electric field in the context of the

Rydberg guiding data.

Figure 3.5 highlights the excitation/detection region discussed previously in section 2.2.1. Part (a) of the figure shows the relative orientation of the electric and magnetic fields within the guiding region, as well as a sketch of the ion trajectories through the slits in the vertical electrode and the MCP's extraction tube. Figure 3.5(b) shows that small changes of the potential applied to the vertical electrode produce significantly different potential shapes along the ion extraction trajectory, with some values of applied electrode voltage giving a potential barrier that the ions would have to overcome to travel from the guiding region (represented by the black dot) to the MCP.

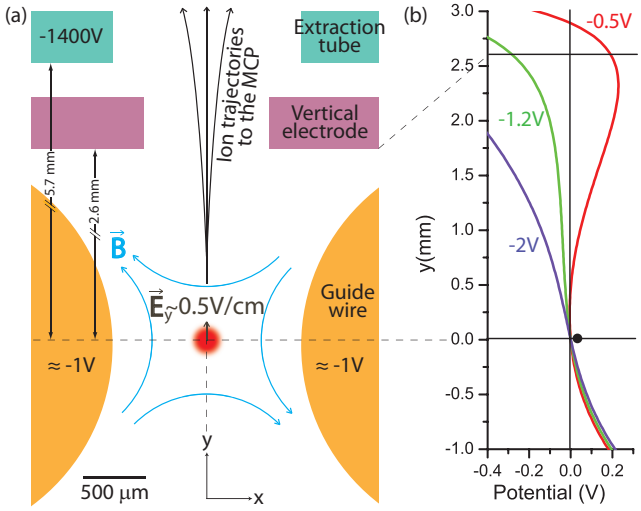

Figure 3.5: (a) The guiding channel and surrounding region. The magnetic field is fixed; a sketch of the lowest order term is displayed. The strength of the electric field is tuned with the vertical electrode. Heights of the vertical electrode and the guard tube are not to scale; the distances from the center of the guiding channel to the bottom of the vertical electrode and the guard tube are 2.6 mm and 5.7 mm, respectively. (b) The electric potential for three indicated potentials on the vertical electrode. The signaled ions are generated at a location with slightly higher potential than the barrier they have to overcome to reach the MCP.

For vertical-electrode voltages more positive than ~ -1 V a potential barrier increasingly prevents ions from reaching the MCP, as evidenced by an absence of the free

ion signals. For electrode voltages more significantly negative than ~ -2 V electric-dipole forces increasingly inhibit Rydberg-atom guiding, as evidenced by diminishing ionization signals after about 2 ms.

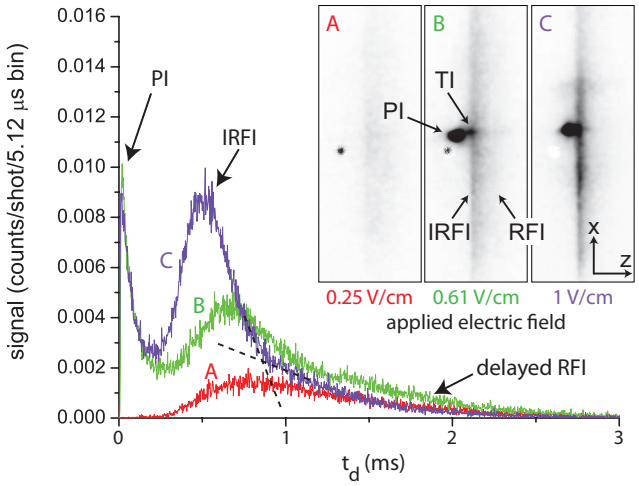

Figure 3.6: Changes in the free evolution signal as a function of applied vertical electric field, matching the three voltage cases shown in Fig. 3.5(b). The inset shows corresponding MCP images of the free evolution (no induced ionization).

The response of the detected free evolution signal to changes of the vertical-electrode potential is shown in Fig. 3.6. The PI and TI signals are due to ions that originate from locations close to the center of the guide, as indicated by the black dot in Fig. 2.9(b). Consequently, PI and TI signals are only observed in the cases with -1.2 V (0.61 V/cm) and -2 V (1 V/cm) in Figs. 3.5(b) and 3.6, where the potential on the vertical electrode is sufficiently negative that ions generated near the atom guiding channel are able to overcome the potential barrier and pass through the electrode region into the MCP for detection.

In the case with -2 V (1 V/cm) applied, where the vertical-electrode potential is the most negative among the cases studied, the IRFI signal is largest and peaks the earliest, as expected from the potentials shown in Fig. 3.5(b). In this case C in Fig. 3.6 with the -2 V applied, we see the largest distinction between the IRFI and the delayed RFI signals. These are labeled in the figure, and I added dashed

lines indicating the distinction between the two. The IRFI signal has a much steeper and narrower distribution of counts in time than the RFI signal. When the two are superimposed as in the data, this leads to a "kink" in the MS trace.

In all cases we observe a widely dispersed signal component at times after 1 ms, which is attributed to delayed RFI. There, atoms that become unguided due to thermal transitions move into regions away from the guide center and ionize remotely. Many of the RFI ions are produced above the barrier or sufficiently below the guiding channel that they have a high likelihood of passing over the barrier. In any case, the RFI signal is not nearly as sensitive to the vertical-electrode potential as the PI and TI signals are. We interpret the RFI signal observed at times $t_d \gtrsim 2$ ms to be from atoms that are guided for some time and then become unguided at some later point in time, leading to a widely dispersed, late-time RFI signal. This late RFI signal is largest in case -1.2 V (0.61 V/cm), indicating that this case combines reasonably efficient Rydberg-atom guiding with an ability to detect PI and TI. Conditions of -1.2 V (0.61 V/cm) are used throughout the Rydberg guiding data, since it is the best compromise between detecting PI and TI signals without critically inhibiting Rydberg atom guiding.

To confirm our interpretation of the data from varying the applied electric field, we have numerically calculated the electric potential in the guide region. See Fig. 3.7, which shows the trap of the center-of-mass coordinate of the Rydberg atoms. This is calculated for atoms with the maximal magnetic moment possible, $\mu = 3\mu_B$, which are the best-bound atoms within the guide. The trap depth, colored in blue in the figure, is about 60 MHz deep and about 0.3 mm wide. The thermal energy is about 18 MHz, so these atoms should be nicely trapped. We have found that the electric field E_y in the guiding channel has a magnitude of $\sim$0.5 V/cm for the conditions used in the experiments, allowing the produced ions to just clear the potential barrier that arises from the set conditions. These findings accord with the above interpretation

of the experimental observations.

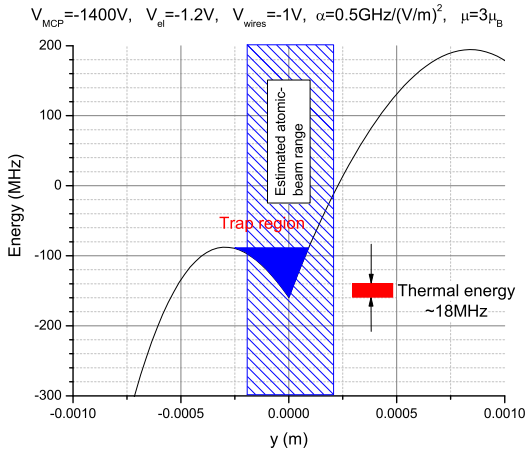

Figure 3.7: The potential along the y axis is simulated, then the electric field is obtained from the derivative of this potential. The energy, plotted on the vertical axis, is $-\frac{1}{2}\alpha E^2$, where $\alpha = 0.5$ GHz/(V/m)^2 is the static polarizability.

3.3 Simulation

In addition to taking experimental data, we have developed a simulation to model the internal-state dynamics. We simulate the experiment by treating the atoms' center-of-mass (COM) dynamics classically and using a quantum Monte Carlo method for their internal-state evolution. The Rydberg atoms are in well-defined $|n, l, j, m_j\rangle$ states at each time step of the simulation. The quantization axis for each atom is given individually by the direction of the magnetic field at that atom's location. Given that the center-of-mass oscillation frequency within the guide is in the kHz range and the Zeeman splittings are in the MHz range, we assume that the internal states of the atoms adiabatically follow changes in magnetic-field direction, leading to well-defined m_j-values and atomic g-factors at all times.

At each time step, the probabilities of thermally induced transitions into other bound target states with $5 \leq n' \leq 100$ or free target states with energy $\epsilon' \leq 0.25$ eV

are calculated for a radiation temperature of 300K. This time step is sufficiently short to accurately model the COM motion because it is orders of magnitude less than the COM oscillation period of the atoms in the guide. It is also sufficiently short to model the radiative transitions between the internal atomic states, because the shortest transition times for the states of interest are longer than $\sim$100 μs. All possible radiative electric-dipole transitions are taken into account. Random numbers determine if the atoms remain in their current states or undergo a quantum jump. The simulated quantum jumps are photo-ionization ($|n, l, j, m_j\rangle \rightarrow |\epsilon', l', j', m'_j\rangle$ with free-electron energy ϵ') and transitions into a different Rydberg states ($|n, l, j, m_j\rangle \rightarrow |n', l', j', m'_j\rangle$). Since the detailed electron properties after photo-ionization are irrelevant, photo-ionization is simulated as one quantum-jump channel, which is a sum over all unbound target states. For the bound-bound quantum jumps there are hundreds of channels due to the large number of possible target states. With the known probabilities for the various jumps, a random number determines which jump occurs. After each quantum jump, the affected atom emerges in a well-defined new state (or it is flagged as photo-ionized). The time step size is dynamically adjusted so that the total quantum-jump probability does not exceed a few percent. The mechanical bounce time within the system is on the order of 1 ms, so time steps cannot exceed a few percent of this. Most time steps are 5-20 μs.

The model accounts for: lifetime increases by thermally driven transitions into states with higher n, ℓ and m_j; atom loss due to thermal photo-ionization; decay toward the ground state; and radiatively-driven transitions from positive m_j (atoms guided) to negative m_j (atoms magnetically expelled from the guide). The simulation is initialized with all atoms having well-defined (n, l, j)-quantum numbers and randomly selected m_j values, which corresponds to the expected experimental situation. The magnetic force, given by the internal-state m_j values and g-factors, acts on COM coordinates of the atoms. The internal-state dynamics lead to time-dependent $m_j(t)$,

which are different for each realization of an internal-state quantum trajectory. The functions $m_j(t)$ determine the atoms' COM trajectories, which are computed classically. The atoms evolve independently as radiative transitions occur between states, with the magnetic force acting on the center-of-mass coordinates. Collisions are not included in the simulation.

Although the Rydberg atom samples we prepare in the experiment are not very dense (see Appendix A for a calculation), we do observe an initial period ($\lesssim$50 μs) of Penning ionization which suggests some degree of ℓ- and m-mixing of the non-Penning-ionized atoms during this initial period. After the Penning ionization ceases, we expect collision-free evolution. The simulations are therefore run for two types of initial conditions. In case (a), the atoms are initially prepared in the $59D_{5/2}$ level with randomly selected m_j values. Here, we model a collision-free situation in which the atoms evolve independently, solely due to radiative transitions between internal states and the magnetic force acting on the center-of-mass coordinates. In case (b), the atoms are initially prepared with an effective quantum number $n^* \approx 58$ and (ℓ, j, m_j)-quantum numbers randomly selected with proper statistical weighting (for an explanation of statistical weighting, see Appendix B). Here, we simulate the effects of an initial phase of complete ℓ- and m-mixing due to Rydberg-atom collisions which randomize all angular quantum numbers of the Rydberg atoms to result in a shell averaged sample.

Simulated plots of the internal-state dynamics for case (a) as a function of time are shown in Fig. 3.8. Figure 3.8(b) shows that the ℓ distribution increases with time. The distribution starts with an initial l-value of 2, corresponding to the initial 59D state. By $t_d = 6$ ms, it ends with $\ell_{\text{avg}} \approx 7$. This increase in average ℓ, along with the simultaneous increase in n, explains most of the long lifetimes that are seen experimentally. More on this topic will be covered in Section 3.5, in the context of Fig. 3.10, where the lifetime given by case (b) is significantly longer than we find

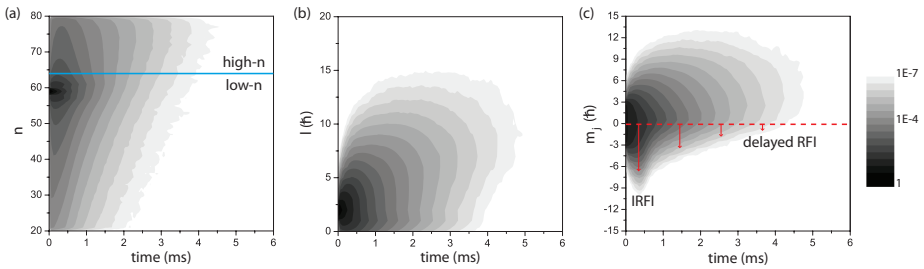

Figure 3.8: Simulated internal state dynamics as a function of time for case (a) of the initialization parameters. (a) n distribution, with the blue line marking the cutoff between high-n and low-n. (b) ℓ distribution. (c) m_j distribution. The length of the red arrows show the rate at which the atoms depart from the guide.

experimentally.

The m_j values, which are initialized in the simulation to random values, spread both positively and negatively at early times as seen in Fig. 3.8(c). Atoms with $m_j < 0$ are high-field seeking and are magnetically expelled from the guide; a fraction of these atoms become directed into regions of high electric field strength, where they ionize and give rise to the RFI signal. Thus, after $t_d \approx 500$ μs, the values for m_j appear to shift higher. Atoms with positive m_j tend to maintain this state for some time since the diffusive radiative transport in m-space is quite slow. The probability flow from the magnetically guided ($m_j > 0$) into the magnetically expelled ($m_j < 0$) domain diminishes with increasing time, as indicated by the red arrows in Fig. 3.8(c). This gives rise to the delayed RFI signal. Most remaining m_j values are positive by the end of the simulated time.

There is no $g_j m_j = 0$ case possible within our system, though having neutral atoms with no magnetic moment certainly sounds reasonable. g_j has a value between 1 and 2, and cannot therefore be zero. $m_j = (0.5 \pm \text{integers})$ and therefore also cannot be zero. For this reason, there are no atoms that simply fall out of the guide under the influence of gravity, since all atoms experience a magnetic force that either contains them within or expels them from the guide. All of the atoms, even those with the smallest magnetic moments, experience a force of a few hundred times that of gravity.

3.4 Experimental Data on Rydberg Atom Guiding

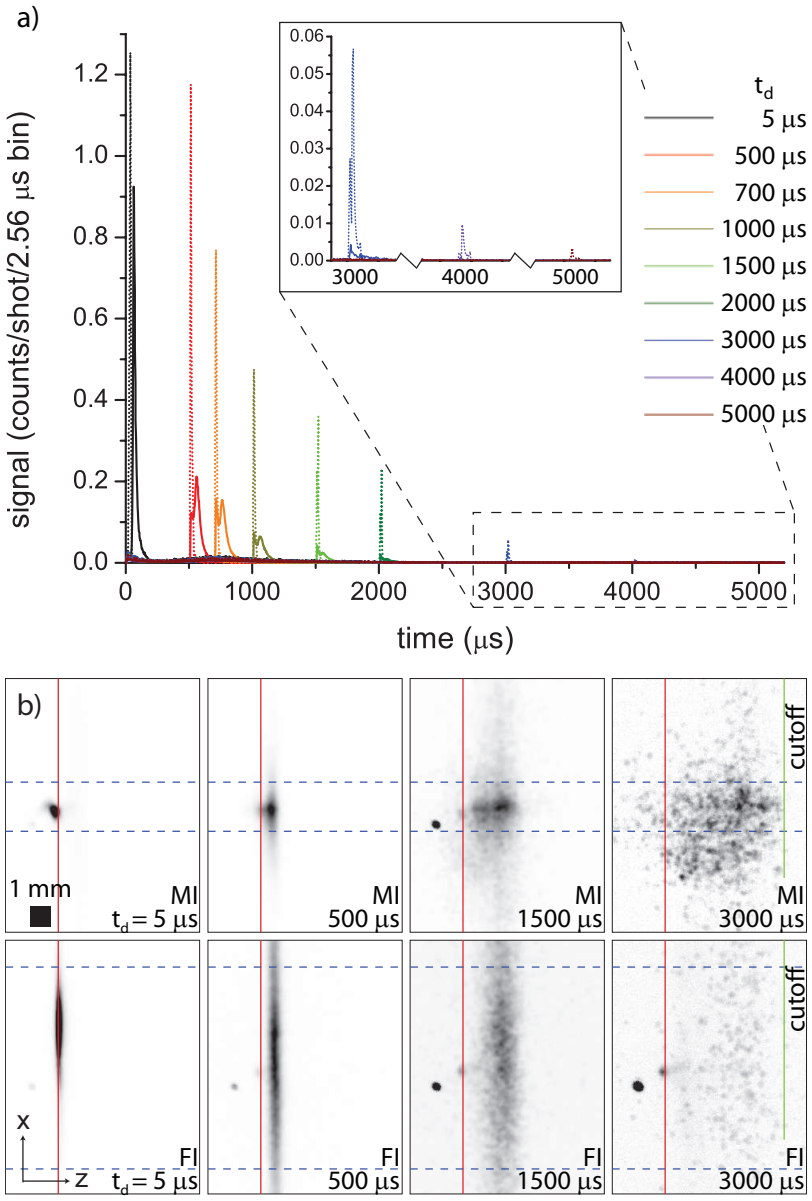

Figure 3.9: (a) MS traces as a function of delay time t_d. MI data is dashed; FI data is solid. (b) Gated MCP images as a function of t_d for FI and MI. The brightness scale for each delay time is adjusted separately for clarity. The dashed lines represent the image location of the guide wires, based on the measured magnifications.

We study the guiding and evolution of the Rydberg atoms in the guide by varying the delay time t_d. Figure 3.9(a) shows MS traces for different values of t_d ranging from

5 μs to 5 ms, for both MI and FI. Figure 3.9(b) shows a selection of gated images. Before the microwave pulse or the FI ramp is applied, we observe Penning ionization and remote field ionization. Both of these signals are intrinsic to our setup and do not play a large role in the analysis of the Rydberg guiding, though are relevant to the overall evolution of the Rydberg atom sample, as I have discussed with Fig. 3.4. The integrated microwave ionization signal in the MS traces in Fig. 3.9(a) corresponds to the signal seen in the images and gives a quantitative measure for the number of Rydberg atoms present in the guide at time t_d.

Based on the field gradient in the guide, we estimate that it takes a high-magnetic-field-seeking Rydberg atom about 1 ms to become expelled from the guide. This estimate is confirmed in the simulations. Therefore, Rydberg atom signals observed after $\sim$1 ms are primarily attributed to guided Rydberg atoms. As shown in the inset in Fig. 3.9(a) there is still microwave ionization signal at $t_d = 5$ ms, indicating that there is guiding of Rydberg atoms out to at least that time. For $t_d \geq 3$ ms the images are partially clipped by the edge of a slit in the electrode noted in Fig. 3.5, leading to a sharp cutoff in the ion images on the $+z$ side (see $t_d = 3$ ms in Fig. 3.9(b)). The signal is only slightly cut off at $t_d = 3$ ms, but we miss detection of significant signal at $t_d = 4$ ms and most of it at $t_d = 5$ ms.

The red lines in Fig. 3.9(b) mark the z-location of immediate detection ($t_d = 5$ μs, which is as close to 0 as we can go in this system) as a reference. By $t_d = 0.5$ ms, the FI signal has spread out such that it is not entirely contained on the MCP and therefore not all of the ions are detected, but the MI signal is much more concentrated. The blue dashed lines indicate the image locations of the inner edges of the guide wires, based on the respective magnifications of MI and FI. The guide wires are a physical boundary on which Rydberg atoms become destroyed on impact. Therefore, any signal outside of these bounds likely comes from atoms that are in the region above the guiding channel. A likely scenario that would explain the signal outside the

horizontal bounding lines is that some atoms are guided for a significant amount of time before transitioning into high-field-seeking states, at which time they would be expelled from the guide. The ionization is applied before these atoms have moved too far from the guiding region to be detected.

The delayed guided Rydberg atom signals in Fig. 3.9(b) show that the atoms travel at an average speed of 1.2 m/s, indicating that the average forward speed of those atoms does not change upon excitation to Rydberg states. The velocity spread, given by the longitudinal extension of the ion signal divided by t_d, remains constant, which implies that Rydberg-atom collisions do not increase the longitudinal temperature of the atomic sample beyond its initial value of $\sim$1 mK.

3.5 Comparison of Rydberg Atom Guiding: Data and Simulation

In the following section, I will compare the experimental data to that of the simulation, addressing both the spatial and temporal aspects of each.

3.5.1 MI and Simulation

In Fig. 3.10 we compare the experimentally observed fraction of remaining guided Rydberg atoms (using MI) as a function of t_d with the simulation (case (a)–circles, case (b)–triangles). With MI (excluding the data points at $t_d = 4$ and 5 ms, where much of the signal is blocked by the edge of the slit), we see a near-instantaneous initial increase in lifetime due to collisions, then a relatively constant decay time of $\tau_{\mathrm{MI}} = 700 \pm 150$ μs. This is significantly longer than the natural decay time of the $59\mathrm{D}_{5/2}$ state, $\tau_{59\mathrm{D}5/2} = 150$ μs. For the FI data, the lifetime varies from $\tau_{\mathrm{FI,min}} = 450$ μs to $\tau_{\mathrm{FI,max}} = 1300$ μs, depending the method used to calculate the lifetime (from the same data). $\tau_{\mathrm{FI,min}}$ was derived using the integral of only the second peak

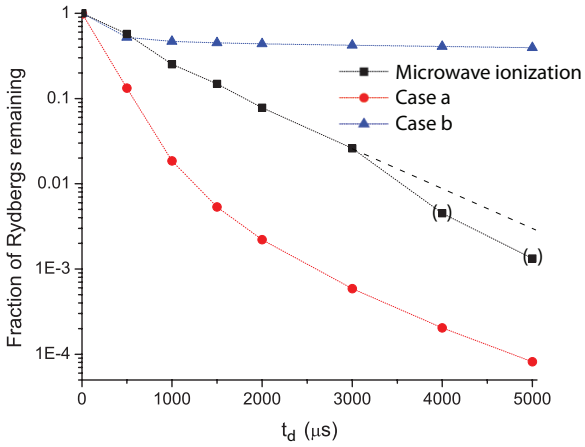

Figure 3.10: Fraction of Rydberg atoms remaining in the guide vs delay time, t_d, from MI experiment (squares) and simulation Case (b) with complete ℓ- and m- mixing (triangles) and simulation Case (a) with complete m-mixing but no ℓ-mixing (circles). The parentheses indicate points where a significant portion of the experimental signal is blocked from detection. The dashed line shows an extrapolation of the experimental curve based on the assumption that the Rydberg signal decay time does not change after 4 ms, where the signal is partially blocked.

in the MS traces, whereas $\tau_{\mathrm{FI,max}}$ uses the fraction of remaining Rydberg atoms (the entire FI signal, so both peaks) with the lifetime calculated as −fraction/derivative. The same two methods gave nearly identical values in the case of MI. In simulation case (a), over the first 2 ms the signal decay time gradually increases from about 200 μs to 1 ms, due to thermal transitions. The decay behavior of the experimental data and simulation case (a) match fairly well at $t_d \gtrsim 2$ ms; however, the experimental guided-atom fractions consistently exceed the simulated ones by a factor of ∼50 in the time domain. We attribute this difference in lifetime-extending behavior to the aforementioned Penning ionizing collisions, which apparently cause a rapid, near-instantaneous state mixing and an associated five-fold increase of the signal decay time. The signal decay time in the simulation case (b), $\tau_{\mathrm{b}} = 33 \pm 5$ ms, is about 30 times longer than the experimental value, indicating that the collision-induced ℓ-mixing in the experiment falls very far short of producing a shell-averaged sample. We conclude that the experimental results lie between simulation cases (a)–no initial

collision-induced mixing and (b)–complete initial collision-induced ℓ- and m-mixing, but significantly closer to the behavior in case (a). In particular, initial collisions do not populate any extremely long-lived high-ℓ states.

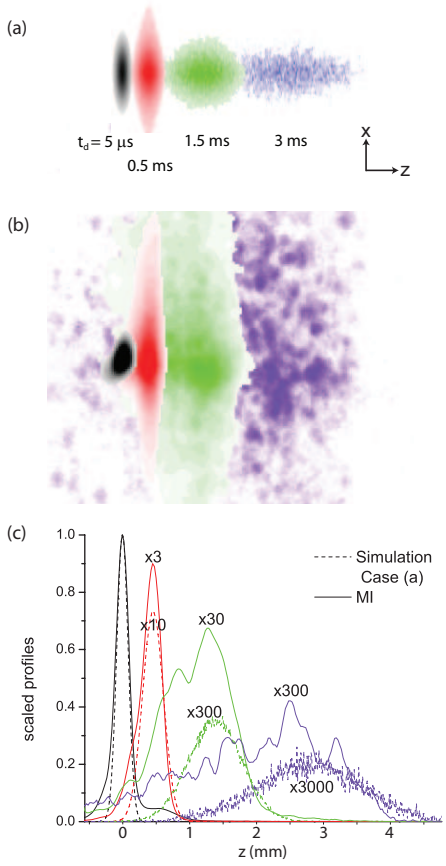

Figure 3.11: (a) Simulated and (b) MI atom distributions at representative times. (c) Integrals along x for the experimental and simulated data. The colors indicate the t_d represented, which are explicitly labeled in (a).

Figure 3.11 compares MI ion image data to that of the simulation, showing atomic distributions for representative simulated t_d are shown in Fig. 3.11(a) and for the experimental MI in (b). Darker areas indicate larger density at each time. Profiles of the MI images in Fig. 3.9(b) in the z-direction (shown in Fig. 3.11(c)) show that the Rydberg-atom distribution transverse to the guiding channel maintains an approximately constant shape up to $t_d = 1.5$ ms. These are each normalized to the initial atom count. The peaks are multiplied by the scaling factors listed for visibility. Dis-

tances are given in the image plane. The experimental values show more atoms as t_d increases than the simulation predicts because the ℓ-mixing, which is not included in the simulation, extends the lifetimes of the atoms [79]. Also, because collisions are not included in the simulation, we expect there to be more atoms remaining for longer times in the experiment.

At later delay times, the fraction of the signal outside the dashed lines in Fig. 3.9(b) increases. As mentioned in the discussion at that figure location, these dashed lines are the boundary for the guide wires in the image plane, so signal occurring outside the dashed lines arises from atoms that originated above the guiding channel. This may indicate that at these later times an increasing fraction of untrapped atoms contributes to the microwave ionization signal, since atoms that thermally transitioned to high-field-seeking states are expelled from the guiding channel, but take some time to completely remove themselves from the experimental region. If some of these untrapped atoms happened to be present at the time of the microwave ionization, they would be ionized in the same way as the atoms within the guide, which could lead to the signal outside of the dashed lines. However, at all delay times we observe a dense core in the images that is due to Rydberg atoms that are in low magnetic field seeking states within the confines of the magnetic guide.

The qualitative agreement of the experimental and simulated data shown in Fig. 3.11(c) validates the simulation. In particular, the longitudinal distributions match very well. Though the experimental data have a significantly larger x extent than the simulated data, the relatively dense and compact core of the MI signals do resemble the shape predicted by the simulation. We believe that this x-extent discrepancy comes from the part of the RFI signal that is present in the experiment at the same time as the applied microwaves. This fraction of the total RFI signal that occurs within the camera's gate time, as discussed with Fig. 3.1, would appear in the ion image along with the MI signal that we are interested in.

3.5.2 FI and Simulation

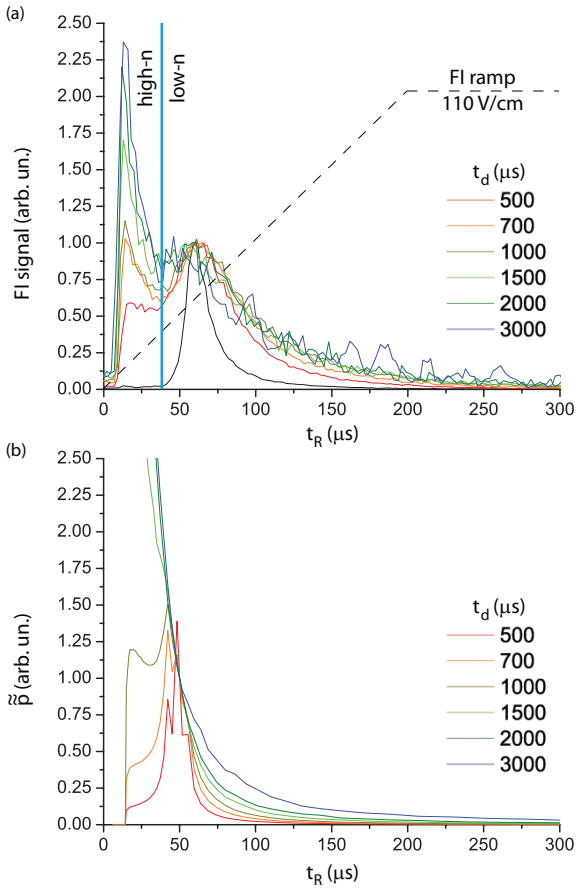

Figure 3.12: (a) FI data, shifted by t_d to align the peak of the signal. Each MS trace is normalized to the value of the second peak. The field ionization ramp (dashed line) is superimposed with the MS traces. The blue line marks the valley between the two peaks. (b) Corresponding FI curves, $\tilde{\tilde{p}}(t_R)$, from the simulated n-distributions at different t_d. In both (a) and (b), the curves for $t_d = 3000$ μs have been smoothed by adjacent averaging. In this figure, t_R is the time elapsed since the start of the FI ramp.

With the MI data above, we are able to compare some of the more general properties of the guided Rydberg atoms to those found with the simulation. Using FI, we can delve a little deeper into the details of the internal-state dynamics of this system.

As seen in Fig. 3.2, the MS trace for FI shows two peaks. Figure 3.12(a) focuses on this FI region of the MS trace, showing the FI traces for several t_d. In this figure, each trace is normalized to the second peak so that the shapes of the traces can easily

be compared. The second peak corresponds to the field ionization signature that arises from the initial state (59D). The field ionization signature of the initial state population diminishes into a shoulder in the state selective field ionization traces around $t_d = 2$ ms. At later times, the second peak becomes too small for clear detection.

The location of the second peak does not change in time, though it does broaden, which is likely due to the state mixing that starts immediately after excitation and is due to collisions (for $t \lesssim 100$ μs) and thermal transitions (at all times). Figure 3.8 shows that the overall m distribution has increasingly higher average m values as time elapses. This would lead us to expect FI spectra to exhibit diabatic peaks [53]. The peak remains at a fixed time (about 60 μs after the start of the FI ramp, as seen in Fig. 3.12(a)), so there is no evidence of diabatic peaks within our experimental data. This is a reasonable, if unexpected, observation. The field ionization ramp is very slow, which leads to the atoms experiencing the FI process adiabatically. Possibly a stronger reason for the lack of diabatic peaks is the strength of the transverse magnetic field present in the system. This turns crossings into anticrossings in Stark maps, which pushes toward adiabatic FI [53]. As seen in Fig. 3.5(a), once the atom is slightly above the center of the guiding channel it enters a region of transverse magnetic field, which is on the order of 10s of gauss and couples states with m-quantum numbers different by 1; coupling strengths scale as 1.4 MHz/G. The presence of the magnetic field makes the atoms undulate through the Stark map, without significantly changing in energy. The simulation shows that even at late times, we mostly have $m \leq 6$, so the majority of the atoms would be coupled together in this way since most atoms would have some coupling partner from the m-quantum numbers differing by 1 criteria.

Since the rise time of the applied field ionization ramp is fairly long (200 μs) the distribution of counts along the time axis in the MS traces allows us to extract the distribution of ionization electric fields of the Rydberg atoms present in the guide.

To compare simulated with experimental data, the raw simulated distributions $p(n)$ after evolution time t_d are mapped into distributions

$$\tilde{p}(E) = p(n)|\frac{dn}{dE}| = p(n(E)) \cdot 4n^5 \tag{3.2}$$

where E is the ionization field, $E = \frac{1}{16n^4}$. Further, for the given linear electric field ramp the simulated distribution vs time is $\tilde{\tilde{p}}(t_R) = (dE/dt_R)\tilde{p}(E(t_R))$.

Figure 3.12(b) shows corresponding simulated FI traces, $\tilde{\tilde{p}}(t_R)$, taken from the simulated n values at the given t_d. The n values are mapped to electric field values, then from there mapped to time values. Specifically, we can calculate the electric field that corresponds to the minimum between the two peaks in Fig. 3.12(a). This minimum (marked with a vertical blue line in that figure) represents a convenient experimental dividing point between the high-n and low-n states. The curves in Fig. 3.12(b) are normalized at $t_R = 50$ μs, in approximate correspondence with the normalization applied to the experimental data. There is a slight discrepancy in the location of the peaks, which we attribute to the fact that the simulation does not take into consideration the ion times-of-flight. By comparing the two plots in Fig. 3.12, we examine the n-state distribution of the atoms. The figure shows that as the value of t_d increases, the low-n peak broadens due to Rydberg atoms transitioning into higher and lower principal quantum states, driven by thermal radiation. This broadening is complete by $t_d \geq 1$ ms, after which time the low-n side become form invariant indicating that the $n < n_0$-state distribution has become fixed. By about $t_d = 700$ μs in the data and $t_d = 1$ ms in the simulation, a prominent first peak arises, which is due to an accumulation of Rydberg atoms in states with high principal quantum number; these states have longer lifetimes than the initially populated 59D. The simulation shows that the high-n side does not stabilize. This is not the case in the data, due to the electric field present in the system, as discussed in Section 3.2.4.

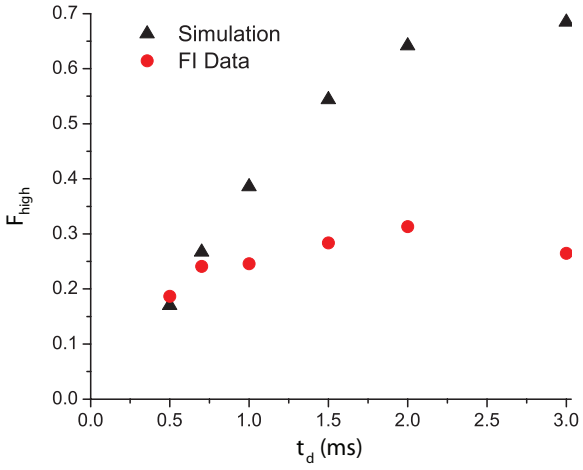

Figure 3.13: Fraction of high-n state atoms, F_{high}, as a function of t_d. Both experiment and simulation show that thermal transitions cause an accumulation of population in higher-n states. In the experiment, the trend saturates at a lower value, presumably due to electric forces that increase in n.

The increase in average n (Fig. 3.8(a)) matches the decrease in needed applied ionization electric field that we see with field ionization. The dividing point between high-n and low-n in Fig. 3.12(a) corresponds to a value of $n = 64$ from the above calculation. For the values of t_d used in Fig. 3.12, the fraction of Rydberg atoms in states with $n \gtrsim 64$, $F_{high}(t_d)$, is obtained by integrating the MS traces from $t_R = 0$ to $t_R = 36$ μs in the experiment and dividing by the integral over the entire t_R range. In the simulation, we obtain $\sum_{n\geq 64} p(n) / \sum_{n\geq 20} p(n)$. Measured and simulated values of $F_{high}(t_d)$ are compared in Fig. 3.13. The statistical uncertainty of the FI data is smaller than the plotted dots in the figure, since it arises from shot noise. These data are an average of 50000 experimental cycles, so the shot noise is $\pm\frac{1}{\sqrt{50000}} = \pm 0.004$, which is too small to be seen on the scale of this plot. Figure 3.13 demonstrates that $F_{high}(t_d)$ increases both in experiment and simulation; the simulated value is consistently higher than the experimental one. In the experiment F_{high} levels off at about 30% at long times, whereas in the simulation it reaches 70%. The discrepancy is likely due to the E_y-electric field, which leads to a saturation of the experimentally observed high-n fraction.

3.6 Rydberg Guide Conclusions

We have observed guiding of Rydberg atoms in a high-gradient linear magnetic guide for up to 5 ms, as well as investigated the internal-state dynamics of Rydberg atoms in our linear guide as a function of time. Field ionization, microwave ionization, and simulations are our primary tools. We find that atoms move toward higher n, higher ℓ, and higher m_j over time, due to Penning ionization, thermal ionization, and other state-changing collisions present in the system. This leads to a guided Rydberg atom signal decay time nearly five times longer than the lifetime of the initial $59D_{5/2}$ state.

A linear magnetic guide provides an excellent apparatus in which to study the internal-state dynamics of Rydberg atoms in a quasi-one-dimensional guide system. In the future, one may realize much longer Rydberg atom guiding times (and therefore guiding distances) by exciting long-lived circular-state Rydberg atoms in the guide using adiabatic state preparation techniques [94]. Alternatively, a crossed-field method [95], which is compatible with various types of atom guides (magnetic, electric, optical), could be used. Circular Rydberg atoms have low susceptibility to stray electric fields and long lifetimes (10s to 100s of milliseconds in a 4K environment), making them ideal for cavity-QED experiments with superconducting microwave resonators [96, 97]. A guided, cold beam of such atoms may enable new studies in this area, in quantum information transport and processing with Rydberg atoms (see, e.g., [61]), and possibly in high-precision spectroscopy [98, 99]. However, the physical setup of our experimental apparatus limits the detection region such that we are only able to detect guiding of the Rydberg atoms over about a centimeter, so these techniques to extend the lifetime of the sample may not necessarily be useful in our system, since we would not be able to extend the detection region to match.

CHAPTER IV

Optical Pumping

After finishing the Rydberg guiding experiments, we began to use guide α for a variety of experiments related to optical pumping. With the setup we already had, very little needed to be changed to begin this vein of experimentation. The main changes involved taking down the microwave horn, adding another repumper laser, and adding a few new coils to the setup. In the follow section, I will explain the background and general goal of this effort, and later discuss experimental results.

4.1 Transfer of States

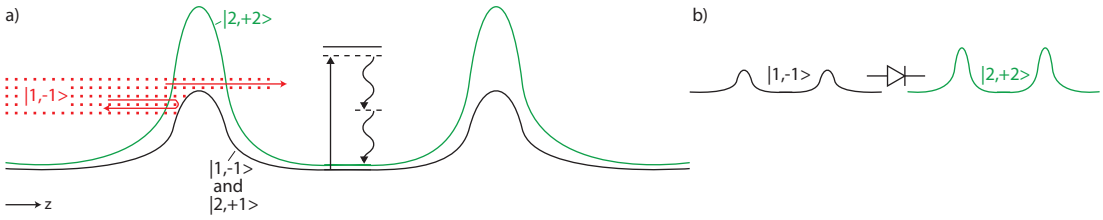

Figure 4.1: (a) Shorthand sketch of the transfer that a pair of photons is capable of. (b) Atom diode analogy, where atoms are irreversibly transferred into the steeper potential.

One of the first, and most important, attempts in the optical pumping experiments was to transfer the atoms from the $|F = 1, m_F = -1\rangle$ state to the $|F = 2, m_F = +2\rangle$ state. Both of these are low-field seeking, and are therefore trapped within the guide's

magnetic potential. A transfer of this type is analogous to an "atomic diode", as illustrated in Fig. 4.1. In this figure, some of the atoms that are initially in $|1,-1\rangle$ are able to travel past the first potential hill. Using the transfer process indicated by the arrows in the middle of the diagram, the atoms are transferred to the $|2,2\rangle$ state, where they then become trapped by the twice-as-deep potential. Once in the deeper potential, the atoms have no way to transfer back to the shallower potential. A similar scheme, though implemented in reverse, is used to transfer atoms from a $|2,2\rangle$ BEC into a $|1,-1\rangle$ BEC in a different group's quest for a continuous atom laser [47, 1].

There are three possible low-field-seeking states in ^{87}Rb: $|F=1,m_F=-1\rangle$, $|F=2,m_F=+1\rangle$, and $|F=2,m_F=+2\rangle$. These are highlighted with red ovals in Fig. 4.2. All other states are either untrapped or high-field-seeking. As covered in Chapter III, high-field-seeking atoms are rapidly expelled from the guide. The guiding potential is $\mu_B g_F m_F |B|$, where $\mu_B = 9.27\times10^{-24}$ J/T is the Bohr magneton, g_F is the Landé g factor of the hyperfine structure, m_F is the hyperfine sublevel, and B is the magnetic field. Given this, atoms in the $|F=2,m_F=+2\rangle$ state will see a magnetic potential that is twice what atoms in the initially guided state see. This allows for greater guiding efficiency, and also would allow for more efficient adiabatic evaporative cooling, if one were able to apply such a method in our system. However, to make this change of guided state from $|F=1,m_F=-1\rangle$ to $|F=2,m_F=+2\rangle$, there is a net change in total angular momentum of $|\Delta m_F| = 3$, which is not allowed in a single optically pumping transfer under quantum selection rules.

Therefore, we need at least a two step process to transfer the atoms' states. To do this, we employ two different repumpers in the middle of the guide, tuned to the transitions indicated in Fig. 4.2. One is tuned to the $F=1\rightarrow F'=0$ transition, and the other is tuned to the $F=1\rightarrow F'=2$ transition, hence the labels R10 and R12 respectively. (R12 is the same repumper labeled Excr in Fig. 2.1.) The arrows in the

figure represent one possible successful channel of transfer from $|F = 1, m_F = -1\rangle$ to $|F = 2, m_F = +2\rangle$, where success means changing the magnetic moment of the atom in question. This particular path involves two excitations, using the R10 and R12 lasers, and two spontaneous decays.

This is a rather complex optical pumping situation for calculating the transition probabilities and rates, as there are 8 ground states and 16 excited states to consider. The excited states do not become significantly populated but are still important in the calculation of transitions rates. When calculating transition probabilities, there is a global conservation such that any atom that exits one state must transition into another state. In our system, the photon scattering rate (see Appendix C) is large enough that coherence effects do not need to be considered. However, there are many parameters that do affect the transitions rates. The laser lockpoint and the Zeeman shifts (which are position dependent within the guide) affect the detuning that the atoms see. The local magnetic field direction is not fixed, so an accurate model of the system has to decompose the incident laser beams into their σ^+, π, and σ^- components. The magnetic field also defines the quantization axis for the atom, and when a transition occurs there is often a change in m-state which can change the atom from a state that is trapped in the guide to a state that is expelled from the guide. In many ways, calculating the transitions rates in this experiment are similar to those used in the Rydberg guiding simulation detailed in Sec. 3.3. For more information on Clebsch-Gordan coefficients and transition rate equations, see [100].

R10 and R12 are nearly coincident with each other. One enters the chamber after a reflection from a half-mirror, and the other follows a very similar beam path after just missing the edge of that half-mirror. These enter the chamber from the bottom side, traveling in $+y$ direction. The R10 beam has a FWHM diameter of 380 μm and the R12 is 370 μm. Both have top-hat profiles, made by imaging an iris onto the atoms' location. We roughly optimize the longitudinal overlap between the two by

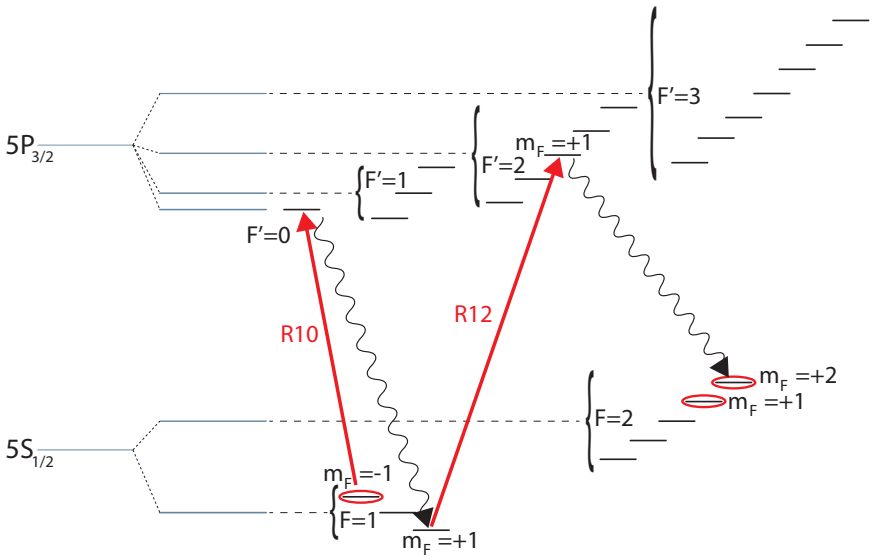

Figure 4.2: Optical pumping levels. The arrows indicate one possible successful channel for transferring the atoms from $|F = 1, m_F = -1\rangle$ to $|F = 2, m_F = +2\rangle$.

moving them onto the underside of one of the guide wires and viewing them with a CCD camera. The fine optimization is done with the total number of atoms that we see at the end of the guide, using a trace like that shown in Fig. 2.5(b).

When the two beams are properly aligned, have the proper polarizations (which depend somewhat on what experiment we are doing), and have the proper powers, we see a strong nonlinear effect on the atoms detected at the end of the guide. This is shown in Fig. 4.3. For these traces, the probe repumper at the end of the guide is blocked. Therefore, atoms that are detected are not still in the $|F = 1, m_F = -1\rangle$ state, since the probe should only see atoms in the $F = 2$ state. This means that the R10 and R12 combination in the middle transferred the part of the population that is detected into the $F = 2$ state. The red trace, with just the probe and no R10 or R12, acts as the background since no atoms are detected. The green and blue curves have the probe and the R10 or the R12 light, respectively. The gray line shows the mathematical addition of the green and blue lines, subtracting off the red background line. The black curve, with both R10 and R12 active at the same time,

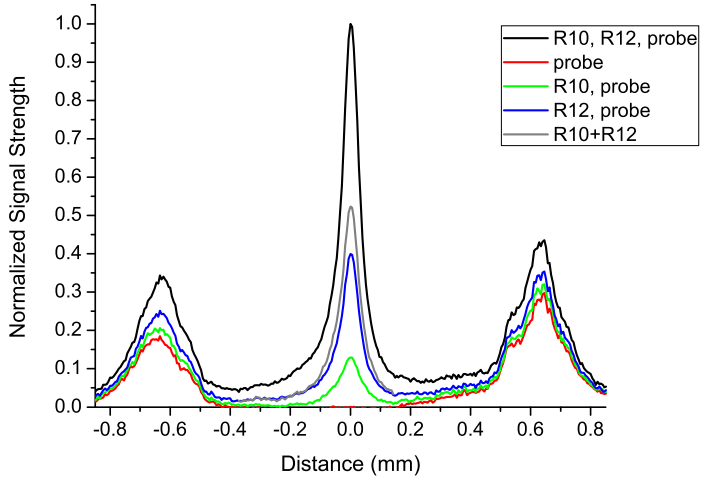

Figure 4.3: Nonlinear effect, detected at the end of the guide as in Fig. 2.5(b).

shows significant enhancement of the atomic signal detected over this addition. As seen in Fig. 4.4, this enhanced signal can saturate and then eventually deplete the detected atoms as the intensity is increased. With the intensity too high, off-resonant scattering can lead to overwhelming loss of atoms within the guide. For more on photon scattering rates, see Appendix C.

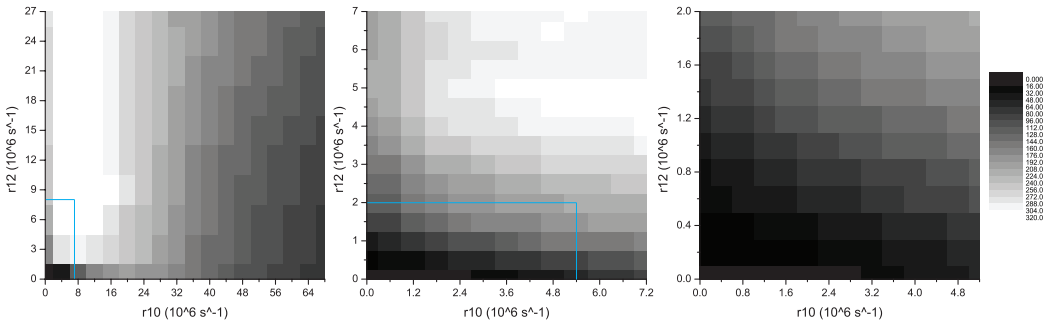

Figure 4.4: Stepping R10 and R12 in power to show the nonlinear effect in a gridded format. The grid axes are labeled in a unit that is proportional to the Rabi frequency, with the x axis for R10 and the y axis for R12. Each plot is taken with successively smaller steps in intensity; the blue lines indicate the zoomed-in region for the next smaller plot.

This nonlinear effect has a strong dependence on the intensity of each of the repumper beams. To characterize the nature of this intensity enhancement, we stepped

each repumper's power iteratively, creating a grid. The left panel in Fig. 4.4 is the full grid, in rather large step sizes. We successively zoomed in on the region of interest, marked with the blue lines in the figure. The nonlinear enhancement in signal is evident by the fact that most grid points have a higher intensity value than the sum of the outermost corresponding row and column.

In addition to varying the intensities of both beams, we also investigated this cooperative state transfer effect by varying the polarizations of each beam, to map out the entire parameter space. Figure 4.4 shows the case with the strongest effect. For this case, R10 is π-polarized and R12 is σ-polarized with respect to the guiding axis, in the laboratory frame of reference. As the atoms traverse the guide, the large magnetic fields of the guiding potential will alter the atoms' frame of reference. The different polarization combinations gave different shapes of the optimal intensity combinations. In this best case shown, the non-linear enhancement is optimal with intensities of $I_{R10} = 0.04$ mW/cm^2 and $I_{R12} = 0.007$ mW/cm^2. In the time it takes for the atomic beam to cross through these two laser beams, this translates into 93 and 16 scattering events for each repumper, respectively, for an atomic beam with a mean forward velocity of 0.88 m/s, assuming that both repumpers are on resonance with their respective transitions.

4.2 Pulsed Atom Guiding

In past experiments (including Rydberg guiding), we had always operated guide α continuously. We realized that it may be advantageous to do some of these experiments with pulsed batches of atoms though. Pulsing the atoms was integral to the study of the atoms reflecting off the magnetic potentials, which I will cover in Section 4.3. For information on how we pulsed the atoms, see Appendix D.

We explore a pulse of atoms flying through the end-of-guide detection region in Fig. 4.5, varying the launch duration from 300 to 1000 ms. In this figure, time=0 is

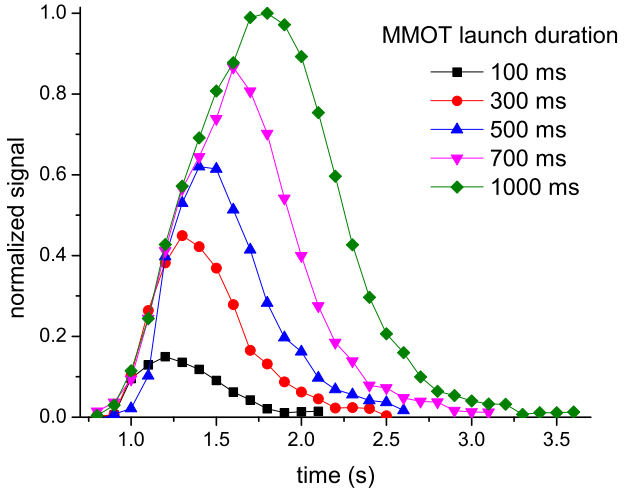

Figure 4.5: Spread in signal at the end of the guide as a function of MMOT launch duration.

when the MMOT first switches from unlaunched to launched. Atom pulses shorter than 1 s show a decrease in peak signal due to the temporal spread of the atoms as the atomic pulse passes through the detection region, as well as due to the time needed to efficiently eject atoms from the MMOT into the guide. The atom packets of the shorter launch durations spread much more significantly relative to the launch duration than their longer counterparts.

In addition to using the computer's analog output to control the MMOT launch timing (see Appendix D), I also use it to send a TTL trigger to a BNC 575 pulse/delay generator. I can program this device to perform the rest of the timing for the experiment. The timing is illustrated in Fig. 4.6. The solid black line indicates the start of the timing sequence; that is the time that the delay box is triggered. The MMOT stays unlaunched for 2 s, then launches for a determined amount of time, usually 1.2 s. The big coil at the end of the guide (see Fig. 2.1 for reference) is always on. An intermediate coil, either coil 1 or coil 2, is turned on 4.8 s after the trigger (2.8 s after the start of the MMOT launch). This is the time at which the atom packet is at maximum $+z$ along the guide; even considering the spread of velocities, this is after

all the atoms have passed the intermediate coil and before any have returned. The Andor camera and the probe light are both triggered at the same time, indicated by the dashed and dotted lines, which we vary from 3.6 s to about 10 s. By beginning the delay time as early as 3.6 s, we image the very first atoms to enter the detection region. Because the detection is destructive to the atoms in the guide, we only take a single shot of an atom packet in a given experimental cycle. On the next cycle, we can vary the delay time between the trigger and the detection, as indicated with the gray scale pulses on the Andor camera and probe lines in the figure, thereby imaging the atoms as they traverse the detection region on subsequent passes after being magnetically reflected. Often, we use a camera exposure time of 0.2 s. Having the probe on for a bit longer than the camera exposure time, as long as it is turned off before the next experimental cycle begins, does not affect the experiment in any way.

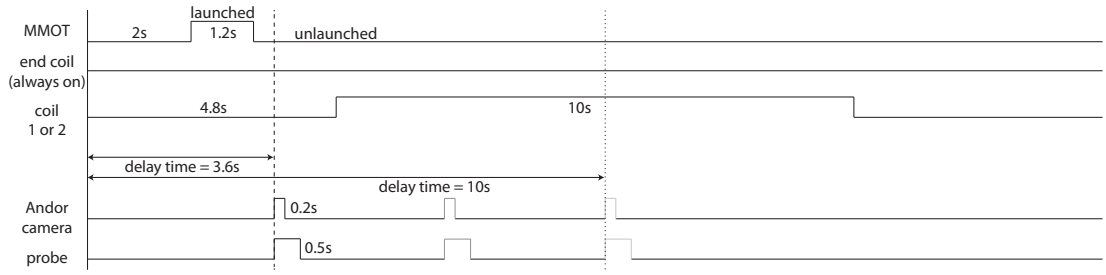

Figure 4.6: Timing of the optical pumping experiments. The delay time, the time from the experimental trigger (solid line) to the detection (dashed, dotted lines), is varied between 3.6 s and 10 s. The pulses on the Andor camera and the probe, shown in different shades of gray, indicate three different delay times that are applied during different experimental cycles.

We used the pulsed MMOT scheme to measure the mean longitudinal velocity of the atoms in the guide. These velocities are shown in Table 4.1. We can vary the vertical launch velocity of the MMOT by changing the frequency difference between the two beams (see Equation 2.1). The values that we found for having the MMOT pulsed did not quite agree with the values we had measured with the Rydberg guiding experiments, so we also used the current setup to measure the velocity of the

atoms while the guide was in continuous. To do this, we applied a killing pulse to the middle of the guide for a certain duration of time. This required having an R12 repumper as well as the cycling transition (Exc+Excr in the Rydberg guiding notation, see Fig. 2.1) to completely knock all guided state atoms out. This appeared in the detection at the end of the guide as a gap in the atomic flow. From these gap images, we found the velocities to be more comparable with those measured with the Rydberg guiding, so the main difference arises from having the MMOT continuously operating or in a pulsed configuration. I attribute the differences that remain between the two continuous measurements to be from the distances involved; with the Rydberg data the velocity was measured in micrometers per microsecond in the MCP images, whereas the probe is located $\sim$75 cm from the kill pulse. Because of the longer distances involved, I believe the latter to be the more accurate measurement. Nearly all of the optical pumping experiments were done with a launch velocity of 2.4 m/s, which corresponds to a horizontal velocity of 1.01 m/s (pulsed) or 0.88 m/s (continuous).

The fourth column in Table 4.1 lists calculated values, based on energy conservation from when the atoms are launched from the MMOT to when they reach the bend into the horizontal section of the guide. These values are quite a bit higher than the measured values. This discrepancy could arise from having the MMOT beams not perfectly at 45°, since that would affect the vertical velocity that we believe we are applying. Additionally, the measured values assume that the atoms maintain a constant velocity throughout the entire horizontal part of the guide, which may not necessarily be the case.

4.3 Magnetic Reflection

One of the overarching goals of this project is to contain atoms within the guide. A longer trap time, especially if combined with a deeper trapping potential from a

vertical velocity (m/s)	pulsed MMOT: horizontal velocity (m/s)	continuous MMOT: horizontal velocity (m/s)	calculated velocity (m/s)
2.2	0.73	0.63	0.96
2.3	0.86	0.74	1.17
2.4	1.01	0.88	1.36
2.5	1.14	1.00	1.53
2.6	1.35	1.17	1.69
2.7	1.45	1.35	1.84
2.8	1.51	1.45	1.98
2.9	1.65	1.62	2.12

Table 4.1: Velocities in the horizontal section of the guide, as a function of the vertical (launch) velocity of the MMOT.

transfer of the atomic state, could lead to increased collisions that may possibly lead to further cooling of the atoms within the guide. After exploring some of the optical pumping possible in our setup, we turned to a study of magnetic reflection within the guide as a way to trap the atoms for a longer time.

For this magnetic reflection study, we reflected the atomic flow off of magnetic potentials provided by various coils, particularly coil 1, coil 2, and the end coil. For relative positioning of each coil, see Fig. 2.1.

We began our magnetic reflection study by using only the end coil, which has 711 ± 2 turns. The center of the end coil is located $\sim$18 cm from the probe. Running at 4 A, it produces a magnetic field of $\sim$7 gauss at the probe location. The magnetic field produced by this coil is profiled in Fig. 4.7. To operate this end coil continuously at this current, we have a small fan pointed directly at the coil. The coil mount, which I designed and machined, has a large surface area (shown in Fig. 4.8), which helps significantly with heat dissipation. However, should the need arise to run at an even higher current, we would need to develop a way to water cool the coil. For a sense of scale of the end coil, the circulation holes are 3/8" diameter, and the inner diameter of the mount is just over 2.75" so that the mount can slide over the vacuum flanges at

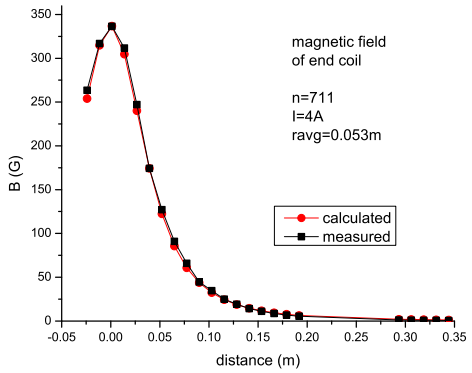

Figure 4.7: Magnetic field of end coil running at 4A. Values are measured with a gaussmeter and compared to those calculated using the formula $B_z = \frac{\mu_0 n I r^2}{2(z^2+r^2)^{3/2}}$, where $n = 711$ is the number of turns comprising the end coil, $I = 4$ A, and r is the fitted "effective" radius of the coil.

the end of the guide. The coil is wrapped in the 2.8 cm gap between the two plates.

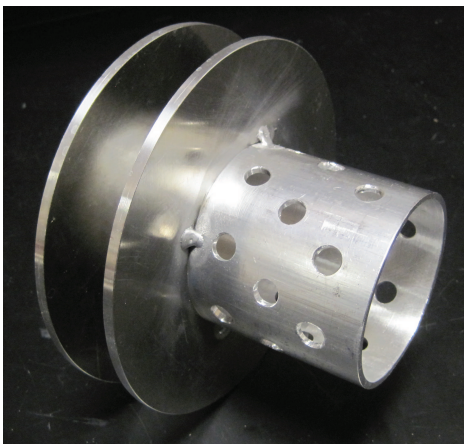

Figure 4.8: Mount for the end coil.

This giant coil is integral to the magnetic reflection experiments at the end of the guide. Using the end coil, we can easily see reflected atoms in the images. Figure 4.9 shows this quite clearly. The atoms are traveling in the $+z$ direction within the guide, so the bottom blob is the incoming atomic beam. We change the detuning of the probe beam to make it resonant with the atoms at the center of the guide, based on the magnetic field applied. The top blob in the figure shows atoms that are reflected by the end coil's magnetic field and are traveling in the $-z$ direction.

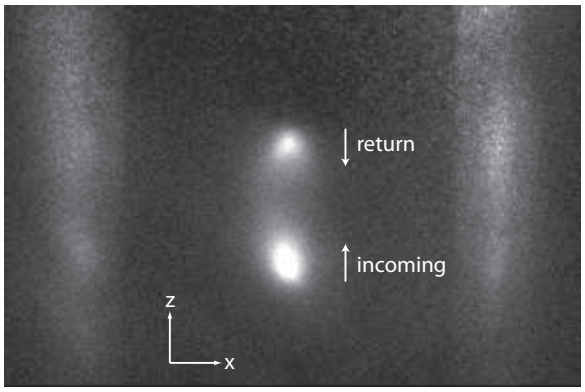

Figure 4.9: Reflection of the atomic beam off the end coil.

The relative amount of atoms detected in the reflection compared to the incoming signal strongly depends on the velocity at which the atoms are traveling, as well as the current running in the end coil and the delay time at which the image is taken.

4.3.1 Double Magnetic Bouncing

If we can easily reflect the atoms once using a magnetic field, it should be entirely possible to reflect them multiple times. Here is a first look at that attempt. To load the guide in batches of atoms, I periodically launched and unlaunched the MMOT by changing the detuning of the upgoing and downgoing MMOT beams. The MMOT launch duration was for 1.0 s for this data. To see the multiple reflections, I had the end coil running continuously at 2.5 A. I pulsed coil 2 (see Fig. 2.1) on at 6 A, varying the delay time of the coil turn-on relative to when I pulsed the MMOT. The centers of the end coil and coil 2 are 18.4 cm and 21 cm from the probe, respectively. This is as close as it is physically possible to place each coil.

In Fig. 4.10, I have profiled a series of images like those in Fig. 4.9. The legend gives the delay time from the trigger to the detection, where the MMOT was launched from 2.0 s to 3.0 s. At a launch speed of 2.4 m/s, the speed in the horizontal portion of the guide is about 1.01 m/s. Therefore, it makes good sense that at 4.0 s all of the detected atoms are in the incoming signal since this is only about 1 s after the

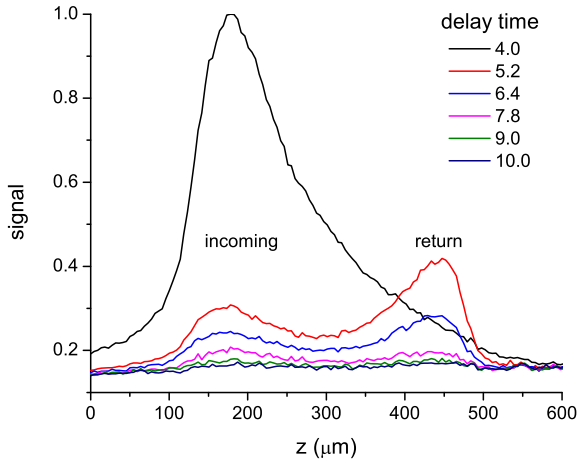

Figure 4.10: A first look at the double-bounce behavior of the atoms within the guide.

end of the MMOT being launched. At 7.8 s (nearly 5 s after the end of the MMOT launching) we still see a good amount of signal, indicating that we have quite nice trapping of the atoms between the two magnetic coils.

For the graph in Fig. 4.10, data was taken every 0.2 s, but plotting them all makes the figure too crowded. In looking at a finer time step, there is a slight amount of sloshing visible in the atomic signal as atoms bounce between the two coils. After some time, the atoms between the coils mostly merge into a flow where there are approximately as many atoms moving in $+z$ as there are in $-z$ at any given point in time.

In similar data to that shown in Fig. 4.10, we perform a more rigorous analysis. Instead of simply taking the profiles of the picture along the z-direction (as was done for the previous plot), the incoming and return signals were separately integrated. An appropriately-sized region of interest box was drawn around each of the incoming and return signals. The counts inside each box were integrated, then a background (the integrated signal from the same-sized region of interest halfway between the counts and the guide wires) was subtracted from each. Four experimental data sets were averaged together to obtain the plot shown in Fig. 4.11. For this data, the end coil

ran a current of 4 A and coil 2 ran 6 A. Coil 2, which is able to slide in the z direction, was centered 38.4 cm away from the probe, which increased the round-trip distance that the atoms travel between the two coils by 40 cm over the case of Fig. 4.10.

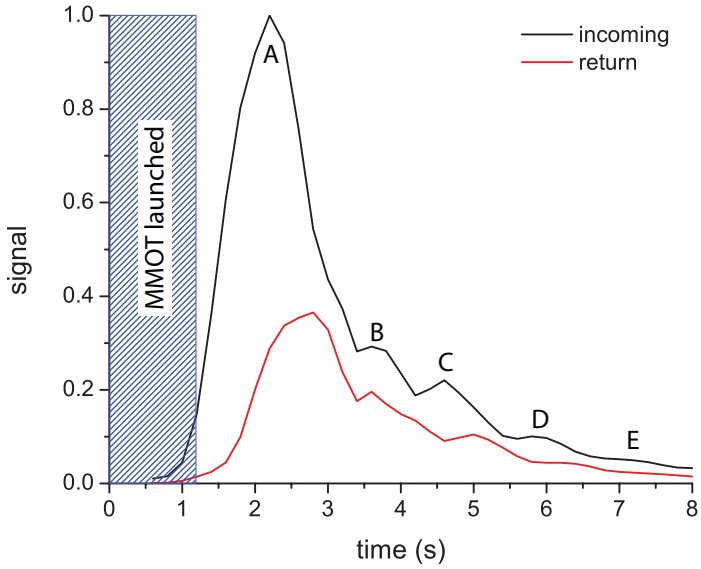

Figure 4.11: Sloshing motion of the atoms as they reflect multiple times between the magnetic boundaries within the guide.

In Fig. 4.11, the MMOT is launched for 1.2 s, as shown with the blue dashed area. The bulk of the atomic packet passes through the "incoming" region for the first time at 2.2 s. This is labeled A in the figure. The following letters label other maxima passing through this region on subsequent round trips through the system. Between each of the maxima in the incoming signal, there is a maximum in the return signal. This indicates that the atomic packet sloshes back and forth between the two coils. In this data, the atoms make at least four discernable round trips.

Exponentially fitting the curves in Fig. 4.11, we find the lifetime to be $\sim$2 s. This indicates that there is considerable loss of atoms, more than we had expected. Various loss mechanisms contribute to a decrease in the atomic signal as a function of time. The most significant loss arises from atoms that have enough energy to overcome the magnetic barrier that the end coil creates. These atoms are energetic enough to pass over the end coil's potential and are lost from the system.

A lesser number of atoms transfer enough energy from the longitudinal to the transverse directions to become untrapped. Of these, the more significant loss comes from atoms that adhere to the guide wires. The atoms are better bound in the plane of the wires than in the transverse plan, but the wires are close enough together (surface-to-surface separation of 1 mm by the end of the guide) that it is more likely that the atoms escape in the x-direction. That said, the magnetic potential in the y-direction does soften enough that a small percentage of atoms could be lost in that direction as well.

The $1/e$ decay time should be the same for $|F = 2, m_F = +2\rangle$ atoms as it is for the $|F = 1, m_F = -1\rangle$ atoms. We will test for this by switching to the intermediate coil before the excitation region (using coil 1 instead of coil 2) and applying R10 and R12 to transfer the atoms to the $|F = 2, m_F = 2\rangle$ state.

4.3.2 Magnetic Reflection Conclusions

The large amount of atom loss seen in Fig. 4.11, as well as the shorter-than-expected trap lifetimes, point to improvements that could be made to the system to increase the number and duration of atoms contained within the guide. By adding external water cooling to the end coil, or possibly redesigning the end coil to use hollow wires with water flowing on the inside (like that of the guide wires), we could increase the magnetic potential present at the end of the guide. Since this appears to be a major loss mechanism, increasing the height of the potential at the end could provide a significant improvement to the number of atoms remaining in the guide after the first reflection.

We briefly studied the effect of the vacuum pressure on the lifetimes of the atoms trapped within the guide. Guide α currently has a vacuum pressure of 5.3×10^{-11} torr. The trapping time decreases with worse vacuum pressure, so it is likely that the converse is also true. It would be possible to add a TSP (titanium sublimation pump)

to the end of the guide, which would improve the vacuum pressure and therefore extend the trapping time.

To address the loss of atoms in the transverse directions of the guide, we would need to decrease the velocity of the atoms entering the magnetic reflection region. As seen in Table 4.1, the velocity in the horizontal section of the guide is about 1 m/s, if a launch velocity of 2.4 m/s is used. There is a critical launch velocity below which the atoms do not have enough energy to gain entry into the guide; this launch velocity of 2.4 m/s is already approaching this critical velocity, based on the number of atoms detected at the end of the guide as a function of the launch velocity. In the present geometry, we cannot decrease the velocity by much more before we would have too few atoms to make the experiment practical. It has been proposed that rotating the entire experimental apparatus by 90° could be an effective way to lower the input velocity. If that were to be done, the atoms would no longer have a 20 cm rise to contend with and could therefore have significantly lower velocities within the main section of the guide. At a minimum, rotating the entire experiment would take a graduate student an entire summer to complete. All of the optics would have to be removed, then restored after the rotation. A different scaffolding would need to be designed and built. The welding cables that bring the current into the guide wires would need replaced, and a new integration scheme would need to be developed for the interface of the welding cables and the water with the guide wires. Once I have completed my degree, there are no graduate students working on any of the three iterations of this project (guide α, guide β, or the spiral guide). In light of these hurdles, I do not think it will be worthwhile to rotate guide α, but would rather see future efforts placed on guide β and the spiral guide. Ultimately, the decision is likely going to be left up to the funding agencies; future students will only have the opportunity to work on projects where there is funding.

4.4 Leaving Guide α

A few questions still remain about the optical pumping experiments already in progress. We hope to finish the majority of those up in the next month. For now, this concludes the discussion of experiments within guide α. The remainder of the thesis will focus on guide β.

CHAPTER V

Guide β

In the quest to experimentally implement an atom laser, I have designed and built a new linear magnetic atom guide for ground-state atoms, guide β. There are many improvements over the existing atom guide (guide α), and we are quite hopeful about the prospects of achieving a continuous, coherent atomic beam with this new apparatus.

5.1 Background

In the intervening years since the experimental achievement of BEC, there have been many pulsed atom laser experiments [21, 28, 31] as well as experiments in 2D [101], steady-state [102], and optically pumped continuous [103] BECs. There have also been several quasicontinuous versions of atom lasers [23, 46, 24, 104, 47], with varying degrees of success in attempting to make the atom laser actually continuous. An atom laser detector that can operate continuously is discussed in [32]. Theory has also been abundant on the topic of atom lasers [105, 106, 107, 108, 109].

After making a BEC continuous, there has to be a way to outcouple the BEC to actually make the atom laser. For this application, the BEC must have stable number statistics, meaning that it needs to be both phase- and amplitude-stable. Our system should be able to achieve this. With the correct output coupler, our system will

provide continuous matter waves. There have been several studies into this topic: a continuous output coupler [110], a pulsed outcoupler [22], strong outcoupling of various Zeeman sublevels [111], and a comparison of available outcoupler choices [30].

There are several limitations expected in the experimental achievement of an atom laser. In particular, proposals have been made regarding the limit of a multistate (all m_F sublevels used in the output) atom laser [112], and the limit of flux achievable in a continuous atom laser [113]. A way to perform counting statistics of the atoms within an atomic laster is put forth here [27].

5.2 Introduction

Realization of a continuous atom laser will be an extraordinary step in the field of atom interferometry, as well as many other areas. Our proposed method for an operational atom laser utilizes a linear magnetic atom guide. Thus, the steps for achieving BEC occur in space, rather than time as is usually the case.

In order to make a BEC in a guide, there are three important topics we must consider. First, we must mode match the atoms injected from a MOT with the atoms in the guide. To do this, we will need to match the kinetic and potential energy closely enough to not disturb the atoms in the guide. The second consideration is that of adiabatic reflection. In most injection schemes into a guide, including ours, there is a section of magnetic compression. As a consequence of the quantum adiabatic theorem, as the atoms enter a region of tightening magnetic potential the atoms will be pushed into a higher level quantum level, which will cause some of the atoms to be reflected. Calculations show that our injection scheme, detailed in Section 5.6.3, should meet the requirements of both of these considerations, mode matching the atomic flow with that of the atoms in the guide, and eliminating the possibility of reflection in the magnetic compression region. The third topic is that of atomic density. To have enough density within the guide, the mean free path of the atoms

at the end of the guide should be on the order of the guide diameter, ∼0.5 mm. Calculating this, mfp = 1/nσ = 0.5 mm, gives a density of n =∼6×10^{12} cm^{-3}. We can compare this to the mean free path of the atoms entering the guide by using the expected flux of 10^9 atoms/s, velocity of 10 cm/s, and cross section of (0.5 mm)^2. This gives a density that is a factor of 100 smaller than needed at the end of the guide, but it is important to note that this is before any evaporative cooling has taken place. This calculated injection density gives a mean free path that is much smaller than the length of the guide, so with these parameters sufficient density should be achieved by the end of the guide.

The design of guide β is largely based on that of guide α [49, 50]. The knowledge of the shortcomings of guide α gave us a good starting place for designing guide β. Based on this, we made three significant changes: 1. The primary pyramidal magneto optical trap was replaced with a Zeeman slower, which has an output flux a hundred times greater than that of the pyramidal MOT. More initial flux should logically translate into more atoms in the guide. 2. Guide α launches the atoms vertically upward 20 cm from the secondary moving MOT into the guide by creating a moving frame of reference for the atoms with the detuning of the MMOT beams. This gives the atoms a significant velocity boost such that by the time they settle into the horizontal portion of the guide they are traveling at an average speed of 1.2 m/s (depending on the speed at which they are launched). There is a small range of tunability to this velocity (∼1.0 to ∼1.9 m/s) but it is still quite fast and this velocity must be counteracted by cooling the atoms significantly to reach ground state. The lower limit on this velocity range is discussed in Section 4.3.2; the width of the velocity distribution increases at slower velocities. Guide β is entirely in one horizontal plane and uses a magnetic plunger to adiabatically inject the atoms from the secondary MOT for guide β (2MOT) into the guide. These atoms will travel at an estimated speed of ∼10 cm/s in the guide. 3. Stray on-resonant light adversely affects the atoms

in guide α. In the new design, we have incorporated a mechanical shutter between the 2MOT and the main portion of the guide.

5.3 Chamber Overview

Figure 5.1 is an Autocad rendering of guide β. The experiment starts with a rubidium oven (1), which emits a steady stream of atoms traveling at a few hundred m/s. These atoms are slowed to a few tens of m/s with the Zeeman slower (2). The Zeeman slowed atoms are captured in a primary MOT for guide β (1MOT) (3). This is a standard 6-beam MOT. We have, so far, measured a substantial increase in the number of atoms in this 1MOT when the Zeeman slower is operating. The atoms are pushed from the 1MOT to the 2MOT with a pusher beam. Because the Zeeman slower and the 1MOT are shared with the spiral guide experiment [45], there is a gate valve with a built-in window (4) on either side of the 1MOT chamber (only one is shown in this rendering). If we are running the guide β, we can close the gate valve to the spiral guide chamber and still allow the pusher beam to pass through the window. The same applies to the spiral guide, in that we can close the valve on the guide β side and open the valve on the spiral side, allowing the pusher beam to push the atoms in the opposite direction. These gate valves are not strictly necessary, but are useful when one part of the vacuum chamber needs to be opened to air and worked on.

The 2MOT chamber (5) has a large number of internal components that will each be discussed in detail in the following sections. One of those components is the mechanical shutter (6), which will physically block all cycling transition and repumper light from the atoms in the guide. At the far end of the 2MOT chamber, there is a built-in cooling block (7). Here cold water is pumped through a circuitous track in the chamber wall to cool all of the injection and MOT coils within the vacuum chamber. Throughout the length of the guide (8), the atoms will experience surface

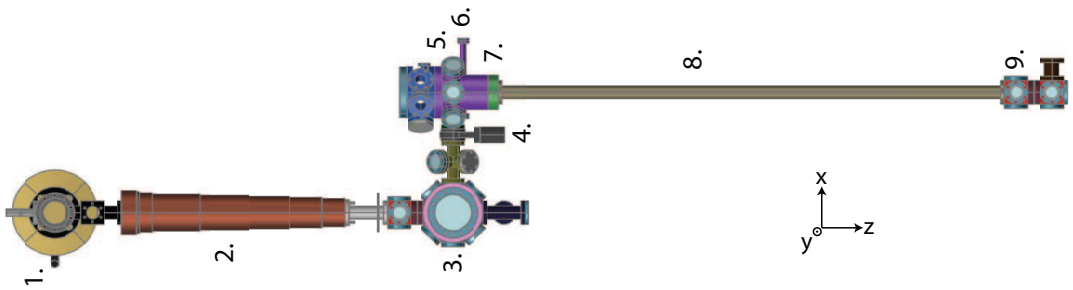

Figure 5.1: An Autocad drawing of the entire vacuum chamber for guide β. 1. Rb oven. 2. Zeeman slower. 3. 1MOT. 4. Gate valve with window. 5. 2MOT. 6. Mechanical shutter. 7. Cooling portion of chamber wall. 8. Surface adsorption region. 9. Detection region. The guide is oriented such that gravity is in the $-y$ direction (into the page).

adsorption evaporative cooling. At the end of the guide, we have a detection region (9). Here, there is a small coil inside the chamber to create a magnetic 'dimple' to catch the atoms. Alternatively, we could use a sheet of green light to make a light shield barrier and outcouple the atoms by changing the intensity of the barrier. These outcoupling methods will be discussed further in Section 6.5.

5.4 Zeeman Slower

We already had a fully functional Zeeman slower in the lab (see Chapter 5 of [114]) so I had to design guide β such that it interfaced onto the preexisting structure. The relative position of the Zeeman slower is shown in (2) of the Autocad drawing in Fig. 5.1.

To show that the Zeeman slower was operating as expected after a lull in use, we examined the absorption spectrum of the atomic beam produced by the Zeeman slower. The plot is shown in Fig. 5.2. The saturation spectroscopy trace shows the $F = 3$ peak and the $2 - 3$ crossover peak (X23), which are separated by 133.5 MHz. This gives a reference scale for the rest of the graph. Comparing the peak locations on the saturation spectroscopy trace to that of the absorption spectrum gives the frequency difference, which, along with the angle that the probe beam makes to the

atomic beam, can be used to calculate the velocity of the slowed atoms. We found this to be 10.9 m/s, which is a quite reasonable speed to be captured by the 1MOT, though maybe a bit on the slow side for what would be expected as the output of the Zeeman slower.

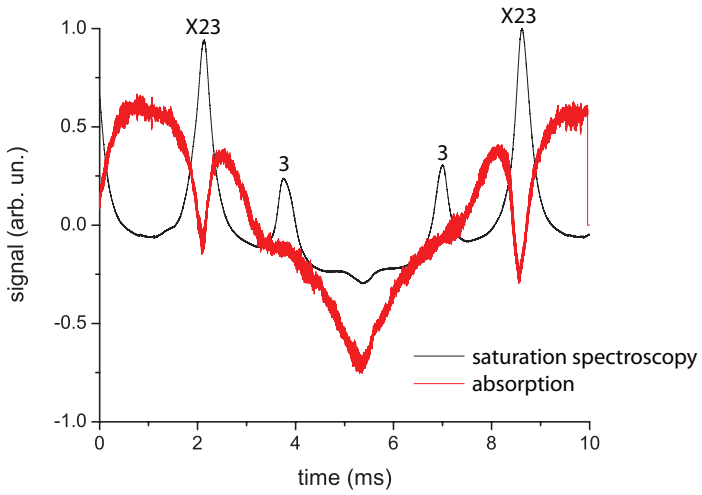

Figure 5.2: Zeeman absorption.

The output of the Zeeman slower is captured in the 1MOT. This is fully functional, and we have seen the enhancement of the number of atoms in the 1MOT when it is fed with the Zeeman slower. This is shown in Fig. 5.3, where (a) is without the Zeeman slower and (b) is with the Zeeman slower. Integrating these two images, we see a factor of 6.6 enhancement in the number of atoms in the 1MOT when the Zeeman slower is operating. Ideally, this number would be closer to 10. As the magnetic field within the Zeeman slower is increased, the Zeeman slower will cool a larger fraction of atoms present in the modified Maxwell velocity distribution of the atoms emerging from the atomic beam oven at the beginning of the Zeeman slower. As we increase this Zeeman magnetic field, the current in the extraction coil at the end of the Zeeman slower as well as the frequency of the slower laser beam must be adjusted. The optimization of these parameters, based on the number of atoms within the 1MOT, is ongoing. Transverse cooling, which will be discussed in Section 6.2, should yield further significant improvements to the atom number captured in the

1MOT.

In these preliminary tests, we see loading times of the 1MOT of ∼250 ms, which is quite low. Such a low loading time could indicate high background pressure, incorrect polarization of one or more beams, or a radiation pressure imbalance. We are continuing to investigate this. We did see that the loading time with the Zeeman slower was a bit shorter than the loading time without it, which is as expected. With a higher loading rate, the MOT will reach a regime where the radiation pressure limits the filling more quickly.

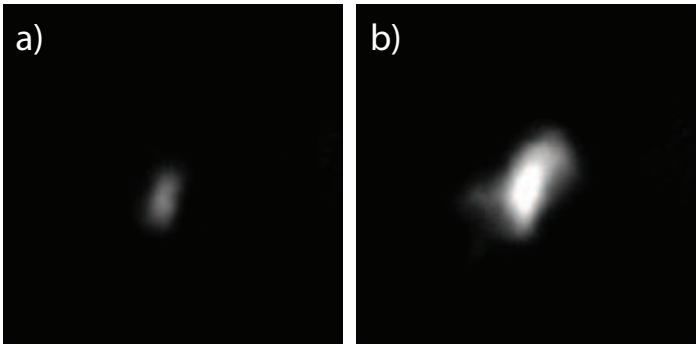

Figure 5.3: The 1MOT (a) without and (b) with the Zeeman slower.

5.5 Guide portion

The main portion of the guide β is the most similar to that of guide α. A metal rail (aluminum in guide β, stainless steel in guide α) supports the guide. This rail, depicted in green in Fig. 5.4 and (8) in Fig. 5.1, needs to be completely flat over the entire length of 65.3". We had the rail for guide β made by Advanced Industries in Chelsea, MI. They were able to guarantee a flatness of 0.005" over this length.

The guide wires are held to the rail with a series of spacers. There are 21 spacers over the length of the guide. Each spacer is 1.5" long. These are depicted in brown in Fig. 5.4 and in yellow in Fig. 5.7. Advanced Industries also manufactured these. The guide wires are held with a center-to-center separation of 0.1644" throughout the

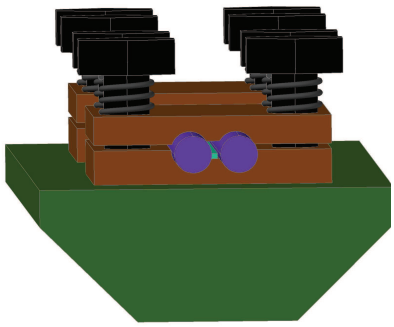

Figure 5.4: A cross section of guide β's rail (green), the spacers that hold the guide wires (purple here, brown elsewhere) in place (brown here, yellow elsewhere), and the silicon strips (light blue) for surface adsorption evaporative cooling. The atoms travel between the guide wires, directly above (in this orientation) the silicon strips. The rail is actually turned 90°, such that the guide wires are vertically stacked.

length of the guide. Both the top and bottom spacers have through holes, and the rail is tapped. The spacers are held together with 8-32 screws, which have springs wrapped around them. The springs are shown in gray in Fig. 5.4. The springs place a small but even amount of pressure on the four corners of the spacers, allowing for a slight thermal expansion of the guide wires. With the guide wire geometry, thermal expansion is significantly more likely in the longitudinal direction, where there should be enough slack in the guide wires before they exit the chamber to adequately adjust to this expansion.

While the atoms are traveling in the guide, we will perform surface adsorption evaporative cooling [115, 116] by slowly decreasing the separation between the atomic beam and strips of silicon held in place with the spacers. The hottest atoms will adsorb (stick to) the silicon surface, leaving the remaining atoms to rethermalize at a lower temperature. A schematic of the surface adsorption plan is outlined in Fig. 5.5. For more on the plan to implement this, see Section 6.4.

Figure 5.5: Schematic of surface adsorption evaporative cooling. The blue dashed line represents the silicon strips that are spaced evenly down the 1.5 m length of the guide. As the atomic beam travels, it is brought closer to the silicon surfaces. The hottest atoms adsorb onto the silicon, leaving the remaining atoms colder.

These silicon pieces need to be at a uniform height relative to the guide wire supports. To ensure this, I developed a very meticulous gluing process. Erik Power (a postdoc in the lab) etched a wafer of silicon into 0.033" strips for me in the clean room. For each strip, I scored the proper length with a sharp knife then broke the wafer along the score line. I discarded any pieces that were not perfectly broken. To get the most even gluing with a UHV compatible epoxy, I used H77S from Epoxy Technology, Inc since it has a small particulate size. Before beginning the gluing process, I cleaned each spacer with acetone and then methanol in the sonicator.

To start the gluing process, I removed the prepared epoxy from the refrigerator so it could warm up. I cleaned all my tools with acetone, paying particular attention to the surface of the special pressure plate that I had made very similar to the top spacer clamps, but with the center portion extended to press against the silicon. I placed a silicon strip on a clean surface, sprayed it with acetone then methanol, then wiped it dry in rapid succession. Using the very tip of a cleaned thumb tack, I scratched a tiny amount of epoxy on each of the plateaus in the clamp. Very gently, I placed the silicon strip on top, using clean plastic tweezers. I placed a small length of wire (1/8" outer diameter copper tubing), covered in kapton, in each of the wire slots to simulate the actual guide wires. I then put rubber spacers, cut to the proper dimensions, on either side of the clamp to give a very small amount of cushioning. Then I added

the pressure plate gently on top. 8-32 screws wrapped in springs were used to hold it together. Using a "homemade height gauge", I made sure to tighten each of the four screws to the same height above the top of the pressure plate, thus applying equal and consistent pressure to each silicon strip. I placed the entire package in a vacuum sealed ($\sim 10^{-3}$ torr) oven. I baked the epoxy at 150°C for 75 minutes, then shut the oven off, leaving the oven chamber under vacuum. After the oven cooled to room temperature (which took at least 3 hours) I could turn off the vacuum and remove my piece. I then dismantled the clamps, discarded the rubber spacers, cleaned the pressure plate, and started the process over. I made a handful of mistakes along the gluing process, and most of those parts just had to be discarded. It took about 2 1/2 weeks to get 21 good spacer clamps with silicon strips appropriately positioned.

The distance from the guiding channel to the surface of the silicon strips will be controlled with magnetic fields that are external to the guide's vacuum chamber. We will need to slowly lower the magnetic field gradient that the atoms see, which will gradually bring the atomic flow closer to the silicon surfaces. For further discussion on this, see Section 6.4.

Once the guide was assembled but before we installed the long nipple that provides the walls for the vacuum chamber in the guide section, we checked the guiding channel for obstructions by sending a HeNe laser through as shown in Fig. 5.6. Thankfully, everything looked fine. This test was repeated after the vacuum chamber was installed around the guide rail with the same results. Hopefully this indicates that the atoms, once injected into the guide, will have no difficulty traveling the entire length.

5.6 Vacuum Chamber

Most of the action of guide β happens in between the 1MOT and the actual guide itself: the 2MOT; tapering of the guide wires; the mechanical shutter; the adiabatic magnetic injection. This was by far the most difficult portion to design. Figure 5.7

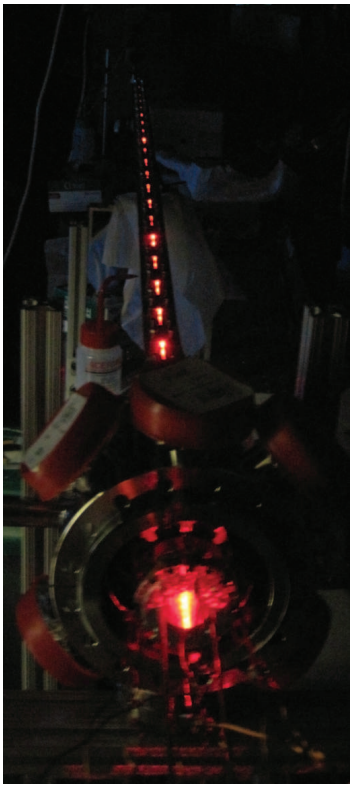

Figure 5.6: Testing the guiding channel for obstructions by sending a HeNe laser through.

shows a cross section view of the vacuum chamber and all of the components for the 2MOT region.

The vacuum chamber (purple and green in Fig. 5.7, (5) in Fig. 5.1) was custom made by MDC. Most of the rest of the components shown (orange, pink, light blue, yellow, dark blue) were made by Jim Tice in the Scientific Instrument Shop housed in the physics department. Each of these components will be covered in detail below.

5.6.1 Guide Wires

The guide wires are made from high-quality, oxygen free copper, but they had been in storage in the lab since guide α was assembled a number of years ago. Therefore, before I could begin the installation process I had to clean the copper. I obtained a long, shallow tray that the entire length of the guide wires could lay in and used this

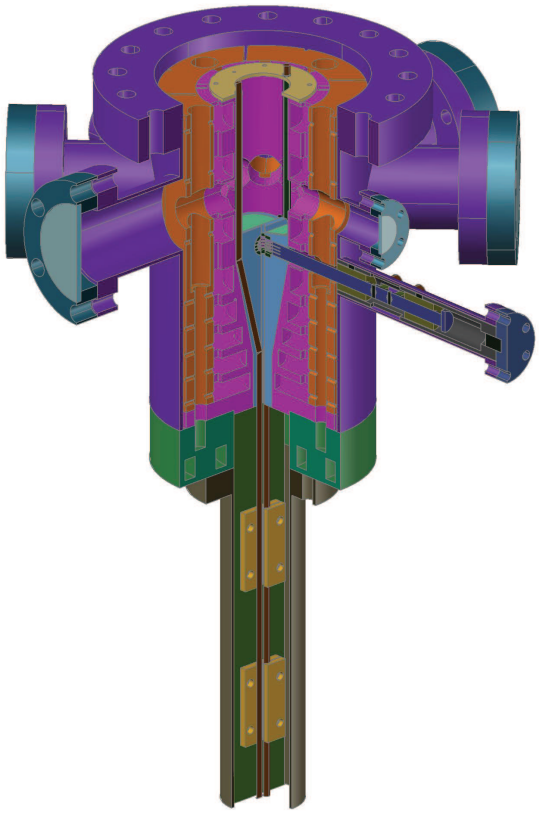

Figure 5.7: Cross section of the 2MOT chamber and the entry to the guide.

to bathe the copper in a low concentration of hydrochloric acid (1 part 1N HCl to 1 part deionized water) to remove any oxidation from the surface of the copper.

Once the guide wires were clean, we had to be quite careful to keep them clean. Each guide wire had to be bent to very specific angles for the compression section of the guide (more on this in section 5.6.4). I created a custom wire-bending apparatus to assist in this bending process and used this to bend the wires by hand.

Installing the guide wires was a delicate process. First we covered the wire sections within the steel casing (see section 5.6.4) with Kapton, then clamped the steel pieces around the guide wires. The steel piece was inserted into the combination of the injection coil holder (see section 5.6.3) and the 2MOT coil casing (see section 5.6.2). The rail (see section 5.5) was attached to the injection coil holder, which then nicely

supported the guide wires. After placing these parts within the external portion of the vacuum chamber, I bent the guide wires to ∼90° at each end to exit the chamber, then slid the remaining chamber pieces over the respective bends.

The guide wires are attached to the vacuum chamber with swagelok connectors. One issue that we discovered with this is we did not have the proper size of swageloks on the custom-built flanges that we had ordered. Therefore, we had to use a two-step process, utilizing some steel tubing that we had left over from another application. The flanges that connect to the chamber are swageloked to the steel tubing, and then the steel tubing is swageloked (with a different size of swagelok on either side of the piece) to the guide wires. The connections of the swageloks work extremely well; we hold vacuum on the level of 10^{-11} torr within the guiding section of the vacuum chamber. A ceramic vacuum break, with a ceramic portion between two vacuum flanges, electrically isolates the guide wires from the rest of the vacuum chamber in each of the locations where the guide wires exit the chamber.

In guide α, we run the guide wires at about 200 A. We knew that we would want to operate similarly in guide β. Running this much current dissipates a large amount of heat within the vacuum, on the order of a few kilowatts. To remove the heat, we run pressurized, chilled water in the center of the hollow guide wire tubes. The copper guide wires have an outer diameter of 1/8". We flow ∼16°C water at 120 psi in the guide wires.

To inject the water into the guide wires, along with the current running on the guide wires, I had to design special mounts to limit the force that the water and current supplies placed on the swagelok connections. The Autocad design for these is shown in Fig. 5.8(a). I milled four of these pieces in the machine shop, two for the input and two for the output. The bulk of each piece, shown in green, is milled from nylon, which is quite difficult to work with since it is so gummy. The three different sections of the support are milled to different but very specific depths, which also

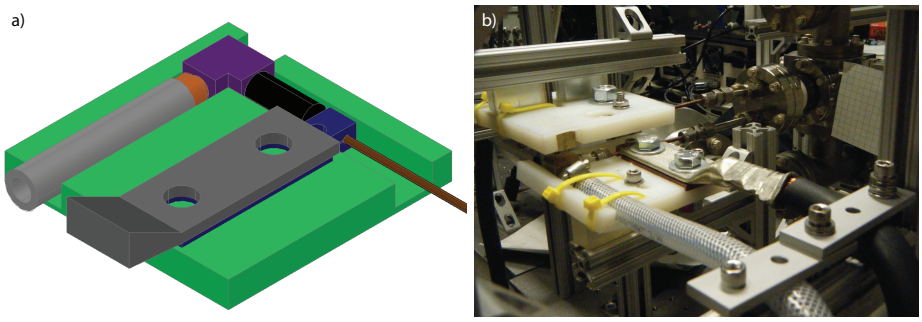

Figure 5.8: Water and current inputs to the guide wires. (a) is the Autocad schematic, showing the water hose (light gray) which feeds into the guide wire via a Swagelok connector (black) and the lug (dark gray) from the welding cable that connects the current via the copper connector (blue). (b) is a picture of the actual setup at the end of the guide.

increased the difficulty of the machining process. The water from the chiller arrives at the guide wires in 3/8" inner diameter hoses, represented in the figure by the light gray cylinder. A hose barb (shown in orange) connects this to a brass elbow (purple). From the elbow, a swagelok feeds the water into the guide wire.

Erik Power designed and machined the copper clamps (shown in blue in Fig. 5.8) to connect the current to the guide wires, since he needed nearly-identical ones for the same application on the spiral guide. From there, we had to connect these clamps to the power supplies, which we did with size 4/0 welding cables. We cut the cables to length, but then had to attach lugs to the end. For this, we needed a special clamp. Erik asked the University electricians to borrow one, which apparently is not allowed, but one of the electricians came to the lab to clamp the lugs for both guides for us for free.

As shown in Fig. 5.8(b), the entire assembly of the water and the welding cables is mounted on sturdy 80-20 supports. The cables and hoses are strain-relieved a few inches away from the mounts. The mounts are electrically isolated from the 80-20 with plastic spacers.

All three guides (guide α, guide β, and the spiral guide) share the high-current Agilent 6690A power supplies for the guide wire currents. To switch between the

three experiments, we installed two "Frankenstein" switches. These robust double-pole-double-throw switches with multiple inputs allow us switch the current between guide α and the south end of the lab, and then from there to switch between guide β and the spiral guide. In a similar manner, I designed switches in the plumbing to route the chilled water for the guide wires between the three experiments.

5.6.2 2MOT Coils

A standard anti-Helmholtz-type configuration for our 2MOT coils would have been prohibitively large for as far away from the MOT as the physical constraints of the chamber mandated. Instead, we have four racetrack-shaped coils on the inside of the vacuum chamber. These produce the same quadrupole magnetic field, with the same field gradients, that one would expect in a typical MOT setup.

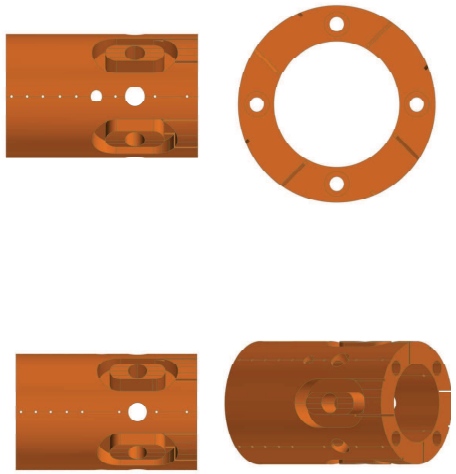

Figure 5.9: An Autocad overview of the 2MOT casing, viewed from four different angles.

These racetrack coils are housed in an aluminum casing within the 2MOT chamber. The Autocad design for this casing is shown in Fig. 5.9, and it is the orange piece in Fig. 5.7.

I built a coil former out of aluminum to wrap the coils on. There were bounding plates on either side to ensure the proper thickness of the coil. All metal surfaces were cleaned and covered with kapton before the wrapping process. This coil former was mounted on a lathe, set to manual turning. We used Epoxy Technology H74 epoxy to form columns of glue in four places spaced around the racetrack to ensure that there would not be air bubbles trapped, which would hinder the vacuum pump-down process. Because these coils were for use in UHV, we had to be extremely cautious while wrapping the coils. Once wrapped, the epoxy was cured in our vacuum oven. After the epoxy was set, I could carefully remove the coil from the former. I was able to remove most all of the kapton as well. The coils were then carefully placed in the 2MOT casing and epoxied in place. The 2MOT coils are shown in the right image of Fig. 5.13.

Through holes in the aluminum casing allow the casing to be screwed to the chamber wall, which is water cooled. Chilled water (at $\sim$16°C) at a pressure of about 15 psi is pumped into the built-in cooling region (green in Fig. 5.7, featured in Fig. 5.10). There is good thermal contact between this cooling portion of the chamber, the casing that houses the 2MOT coils, and the injection coils as well. Thus, all heat generated within the chamber from the 2MOT coils and the injection coils is counteracted by the chilled water in the chamber wall.

5.6.3 Magnetic Plunger

Inside the casing, we have the injection coils for the magnetic plunger. The Autocad design for the aluminum support for this is shown in Fig. 5.12 and is the pink piece in Fig. 5.7. This was a very difficult piece to design, and it was also quite difficult to manufacture. This piece is actually two separate pieces then joined together. Jim Tice did an excellent job machining this piece, and the photographs (Fig. 5.11 is one of the pictures) that Jens Zorn took of it and the other pieces are highlighted on

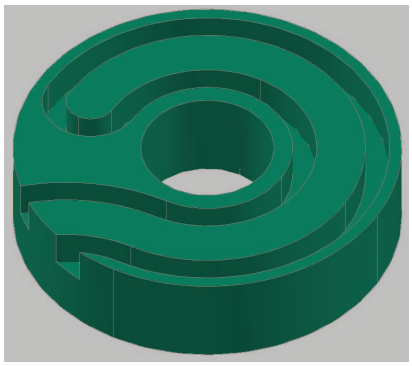

Figure 5.10: The internal cooling track within the chamber wall. MDC made this water track then welded a "lid" in place. The cooling piece was welded to the rest of the vacuum chamber. This water track is entirely outside of the UHV.

the Instrument Shop's website.

Figure 5.11: Jens Zorn took a few high-quality photographs of the pieces the Physics Instrument Shop machined for guide β. This shows the casing for the 2MOT, injection coil support, steel wire support, and mechanical shutter.

There are 8 coils that form the magnetic plunger used to inject the atoms from the 2MOT into the guide. Each of these coils has a different diameter and thickness, as can be seen in either of the left images in Fig. 5.12 of the aluminum support. This support was placed directly on the lathe to wrap these coils. Because the leads for the coils would get in the way, we had to work from the input side (coil -2) down to the exit side (coil $+6$). As with the 2MOT coils, we used H74 epoxy to form columns of glue to prevent against air bubbles. Fig. 5.13 shows a picture of the injection coils

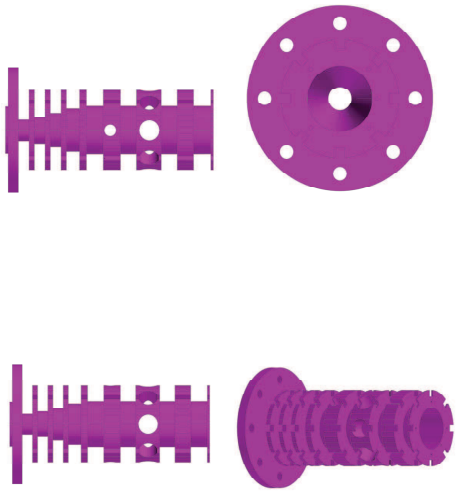

Figure 5.12: An Autocad overview of the injection coil package mount, viewed from four different angles.

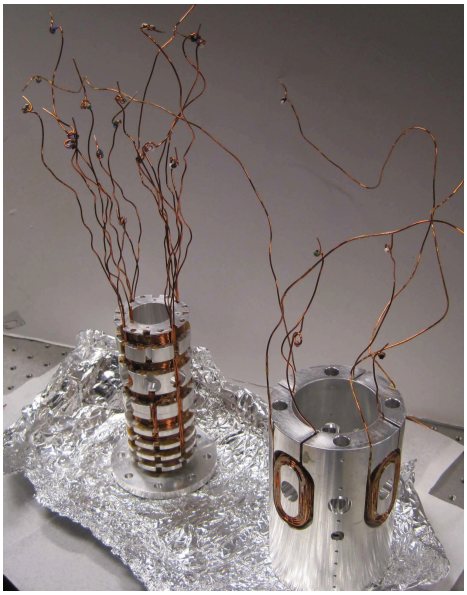

Figure 5.13: The injection coils and the 2MOT coils, just prior to installation. UHV compatible colored ceramic beads were used to mark the different coil leads.

and the 2MOT coils.

To keep track of the wires from each coil, I used color-coded vacuum compatible ceramic beads, purchased from Accu-Glass. Since there were 6 colors of beads, I

connector	1		2
a	west upper 2MOT coil		east upper 2MOT coil
b	Coil +5 return		Coil +6 return
c	Coil +5		Coil +6
d	Coil +3 return		Coil −2 return
e	Coil +3		Coil −2
f	west upper 2MOT coil return		east upper 2MOT coil return
connector	3		4
a	east lower 2MOT coil		west lower 2MOT coil
b	Coil +4 return		Coil +1 return
c	Coil +4		Coil +1
d	Coil +2 return		Coil −1 return
e	Coil +2		Coil −1
f	east lower 2MOT coil return		west lower 2MOT coil return

Table 5.1: Injection and 2MOT coil connections. "Return" refers to the winding direction of the coils; by labeling which lead is "input" (labeled by not labeling) and which is "return" we were able to keep track of which direction the current should be run in each coil. The locations of the coil connectors is shown in Fig. 5.14.

threaded either two or three beads on each wire lead. Figure 5.13 shows how this looked like a tangled forest, but it was extremely useful when I made the electrical connections after assembling all of the pieces. Inside the vacuum chamber, I connected each wire internal cable assembly of the 6-pin electrical feedthrough with a ceramic wire nut. Table 5.1, along with Fig. 5.14, lists the coil connections for all 8 injection coils and the 4 2MOT coils. In the process of installing the injection coil package, the beads only fell off of one of the coils (coil −1). Therefore, there is a 50% chance that the coil leads are reversed on that coil. There is also a chance that coil −2 is shorted to the aluminum case, though tests thus far have been inconclusive.

The circuit to control all of the different coils has had a complicated history. Steven Moses began the design of the circuit, Karl Lundquist did the vast majority of the assembly and testing, a grad student spent a long time chasing noise that

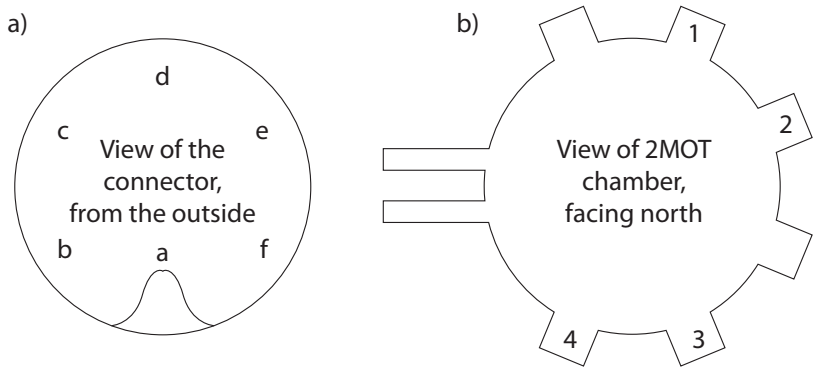

Figure 5.14: (a) 6-pin feedthrough connectors, as viewed from the outside of the vacuum chamber. (b) An outline of the 2MOT vacuum chamber as viewed when facing North, with the four flanges that contain the 6-pin feedthroughs numbered.

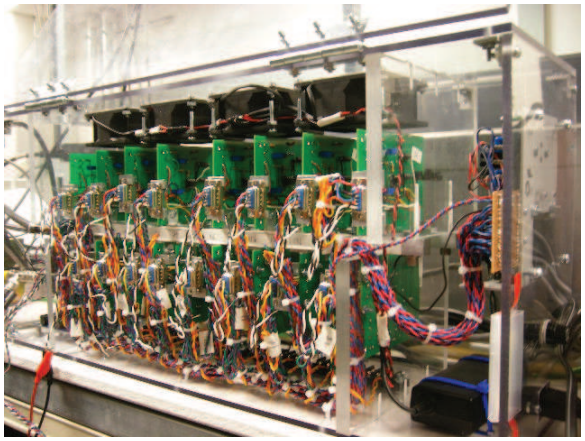

Figure 5.15: Each circuit board controls one coil.

no one else could see, Erik Power wrote the initial software to control it, and Matt Boguslawski made the software actually work. A picture of our circuit box is shown in Fig. 5.15.

A video simulation of the magnetic plunger in action can be viewed at `http://www.youtube.com/watch?v=DHXyEQuirxw`. In this video, the black indicates the guide wires. Blue is low magnetic field, where the atoms are trapped. The atoms start in the 2MOT at $z = 0$. By changing the currents in the 8 injection coils as indicated in Fig. 5.16, the low field region is shifted to the right. The guide wire separation decreases, magnetically compressing the atoms at the same time as they are injected.

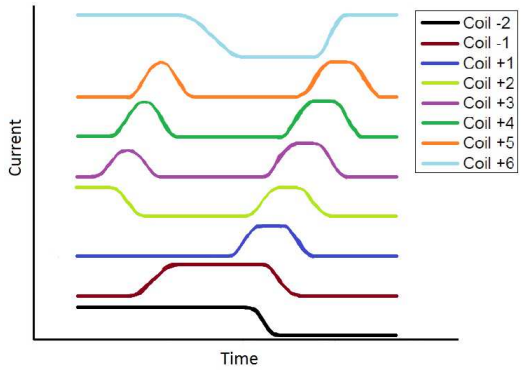

Figure 5.16: The relative current for each injection coil as a function of time.

Eventually, the barrier between the low-field pocket containing the atoms is lowered and the atoms are pushed the rest of the way into the guide to merge with the atoms that are already in the guide. Though this process is pulsed (we anticipate running this injection at a rate of ∼1 Hz) the atoms will be in the guide for long enough (∼10 s) that they will merge into a continuous atomic flow before reaching the end of the guide. Other groups have used similar schemes of pulsed injection into an atomic guide [36, 117].

5.6.4 Steel Wire Support

Inside the injection coil package, we have a housing for the guide wires themselves. This piece, shown in Fig. 5.17 and in light blue in Fig. 5.7, is made of stainless steel. The taper of the outside of this piece, shown well in Fig. 5.17, exactly matches the taper on the interior of the injection coil piece, which is visible in Fig. 5.7. It was because of this taper on the inside of the injector package that the injection piece had to be split into two pieces; it was impossible to machine the internal taper that deep into the piece.

Figure 5.17 also shows some of the other smaller pieces around the steel wire support, which itself is two pieces held together with two screws (this split is visible in Fig. 5.22, and the two screws are shown in dark gray in Fig. 5.20). The dark green

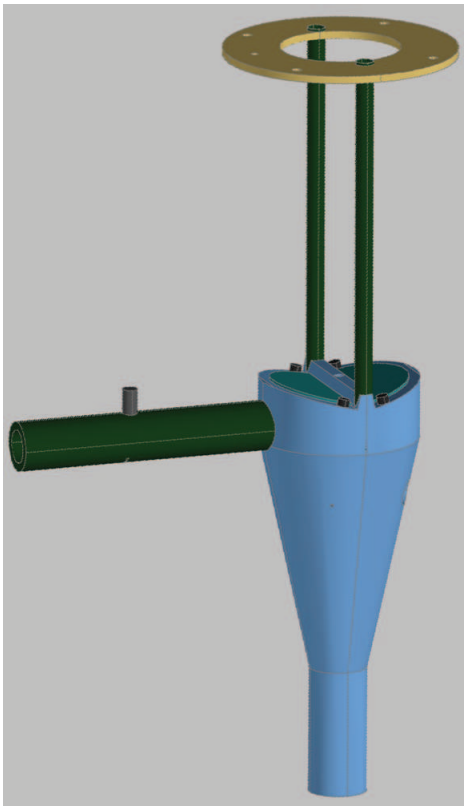

Figure 5.17: An Autocad depiction of the stainless steel wire holder and the stationary portion of the shutter.

shapes are stainless steel tubes, which support the copper guide wires (brown) as they enter the steel piece. These stainless steel tubes fit down into the bulk of the stainless steel piece, and the pale yellow aluminum disk at the top secures that end. This pale yellow disk actually screws onto the top of the injection coil structure. Also visible is the stationary portion of the mechanical shutter (dark green), which will be discussed more later.

In Fig. 5.17, you can see that the top of the stainless steel wire support is beveled at 12.5°. On these angled surfaces, we have two half-circle waveplate-mirrors (dark teal) mounted to retro-reflect the 2MOT beams. We ordered these waveplate-mirrors from Casix after a large amount of communication to ensure that they understood what I wanted them to make. Since we can make a 2MOT, it is likely that the waveplate-mirrors are manufactured close enough to specifications. The waveplate-

mirrors are a 1" diameter low-order $\lambda/4$ waveplate that is cut in half. The top surface has antireflection coating for 780 nm. On the bottom surface, there is a layer of aluminum ($>$ 100 nm). This is the actual mirror. Below that, there is a layer ($>$ 1 μm) of SiO_2 to act as a buffer between the aluminum mirror and the stainless steel piece it is mounted on. It is further protected by a thin sheet of kapton sandwiched between the waveplate-mirror and the steel piece. This waveplate-mirror is held in place with a few different clamps, shown in Fig. 5.19, which I machined. The copper clamp pieces sit beside the waveplate-mirrors and act to define the position of the waveplate-mirror. I made them by drilling a hole in a thin sheet of copper, then using the machine shop's shearer to cut them roughly to shape. The rest of the shaping was done by hand with a file. The teflon pieces actually hold the waveplate-mirror on to the steel wire holder. The teflon is mounted above the copper piece, and is large enough to reach slightly over the waveplate-mirror. I drilled a hole in the teflon piece then cut these to shape by hand with a blade. Two copper pieces and two teflon pieces are used for each waveplate-mirror. The waveplate-mirror clamps are not shown in Fig. 5.17, but they are held in place with the four 0-80 screws that are visible beside the two pieces of the waveplate-mirror.

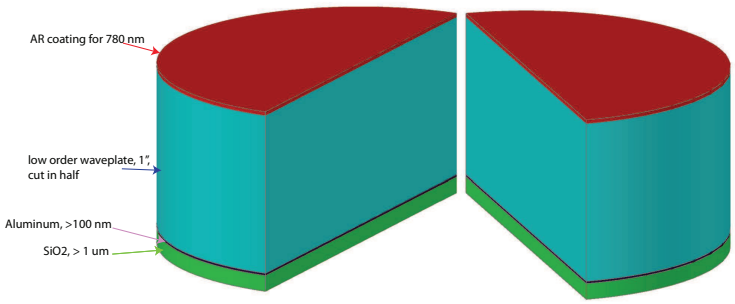

Figure 5.18: The waveplate-mirror.

One of the main functions of the stainless steel wire holder, and the reason we

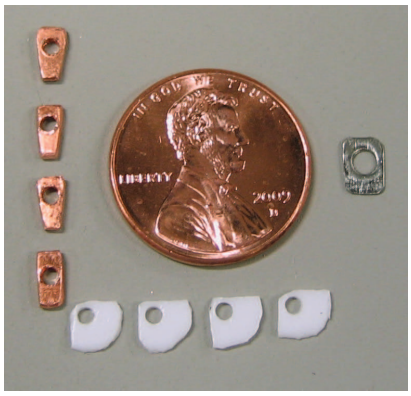

Figure 5.19: Clamps to hold the waveplate-mirrors in place inside the chamber.

chose the sturdier-but-harder-to-machine stainless over aluminum, is to decrease the separation of the guide wires. We decided that aluminum would not be up to the task of keeping the wires from relaxing their bends. This decrease can be seen in Fig. 5.20. I made a somewhat primitive wire bender to bend the guide wires to the proper shape by hand. The guide wires, which are 1/8" hollow copper tubes, are covered with kapton tubing anywhere they are in contact with another surface. This means that they are covered in kapton for the entire distance of the steel wire holder.

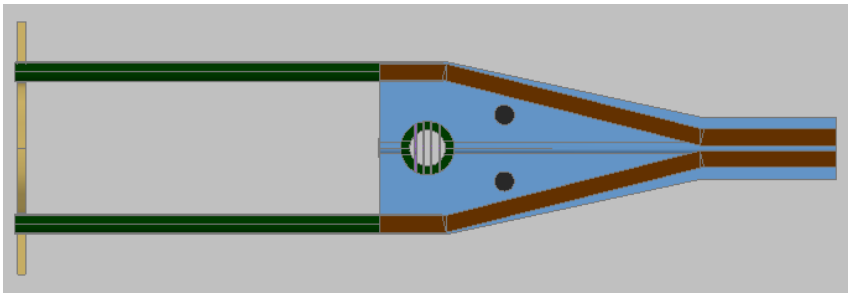

Figure 5.20: The surface-to-surface separation of the guide wires decreases from ∼1" to ∼1 mm over a distance of a couple inches.

5.6.5 2MOT

The timing for the pusher beam, together with turning the 1MOT beams off while the atoms are being transferred, is already in place. The 2MOT already looks quite nice (see Fig. 5.21), but it needs some improvements still. One of the main things we

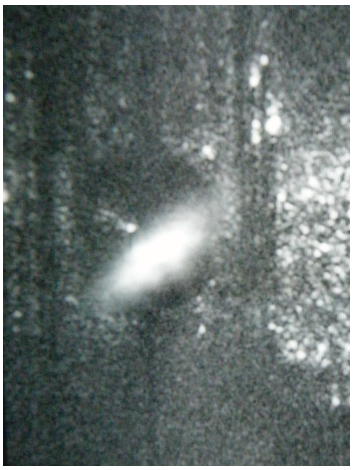

Figure 5.21: An image of the 2MOT. Here, both horizontal beams are going into the 2MOT, but the guide wires are not yet on.

need to optimize is the laser power splitting between the 1MOT beams, the 2MOT beams, the pusher beam, and the Zeeman slower beam.

We began looking for the 2MOT with only two of the racetrack coils, since that still produces the proper magnetic field geometry but is a simpler system. In trying the 2MOT without the guide wires running current, we discovered that the magnetic fields were not quite as expected and therefore the 2MOT was not centered over the hole to get into the guide. We were able to counter this effect by temporarily using a strong permanent magnet a little away from the side of the vacuum chamber. Using all four racetrack coils fixed this positioning issue.

By tuning the currents in the four 2MOT coils, we are able to run the 2MOT with guide wire currents up to $\sim$200 A, which is likely the condition under which we will want to eventually run this experiment.

5.6.6 Mechanical Shutter

A prominent feature in Fig. 5.17 is a stainless steel tube (shown in dark green) that houses the stationary portion of the mechanical shutter. This stationary shutter is highlighted in Fig. 5.22. The stationary shutter fins are made of 0.01" thick stainless steel. They are rectangular pieces 0.4"x$\lesssim$0.402". The second dimension is

approximate and maximal because the pieces are filed to fit inside of a stainless steel cylinder. The relative orientation of these pieces is shown in Fig. 5.22, where the stainless steel tube that houses the fins is dark green and the fins are light purple.

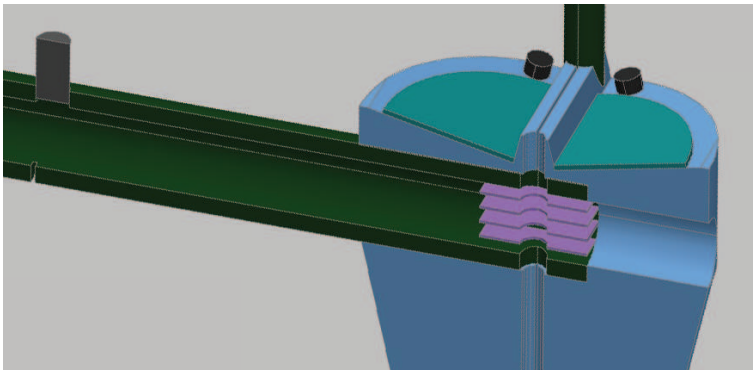

Figure 5.22: A profile view of the stainless steel wire holder, highlighting the stationary portion of the shutter in light purple.

The stationary part of the shutter has two locking mechanisms. The tiny stainless steel piece shown in Fig. 5.19 is a lock for the radial placement of the stationary part of the shutter. It affixes to the outside of the 2MOT casing. Once placed, I rotated this lock into the small slot in the stainless steel tube (visible in Fig. 5.22). The rotational lock is the small peg that is welded into the stainless steel tube (shown in gray in Fig. 5.22) that fits into a slot in the outside of the 2MOT casing (orange piece in Fig. 5.7).

The fins have 0.1" diameter holes in the center. This is the guiding channel for the atoms. These holes in the shutter align perfectly with the hole in the stainless steel wire holder (diameter 0.08") directly between the guide wires. This alignment can be seen in Fig. 5.22.

The relative placement of the shutter is shown in (6) in Fig. 5.1. The moving portion of the shutter (dark blue in Fig. 5.23) has three fins (dark magenta) that fit in between the stationary fins. These moving fins also each have a hole such that, when the shutter is "open", the holes in all 7 fins are aligned and the atoms can pass through on their way into the guide.

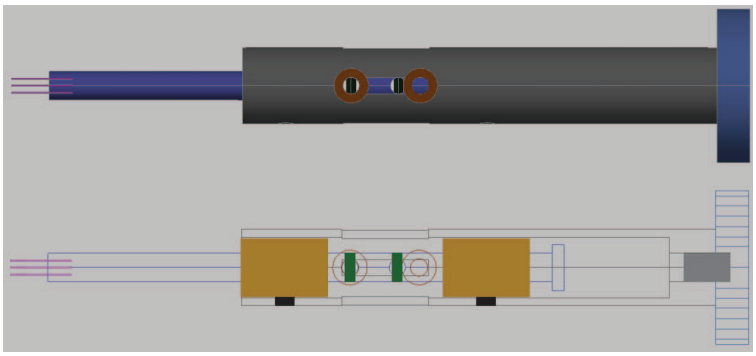

Figure 5.23: An Autocad rendering of the mechanical shutter. The top panel is a solid view, and the bottom panel shows a wireframe view with the bearings, ferromagnetic rods, and set screws highlighted.

The shutter is controlled with a permanent magnet that is mounted on the sliding piece inside the vacuum chamber, shown in green in Fig. 5.23. Coils will be added on the outside of the vacuum chamber (maroon in the top panel), to tune "open" and "closed" with programmable currents. For now, we can manually open and close the shutter by moving a permanent magnet along the outside of the chamber. The shutter slides along two UHV linear bearings (gold) held in place inside the stationary sheath (dark gray) with set screws (black). The stationary sheath is attached to the flange of the vacuum chamber with a set screw (gray). The entire shutter assembly (other than the coils) fits inside the protruding arm of the vacuum chamber (6 in Fig. 5.1).

5.7 Detection of Atoms at the End of the Guide

The detection at the end of guide β is very similar to that of guide α (see Section 2.1.2). An Andor iXon-DU987 camera (nearly identical to the one on guide α) images the space between the guide wires at the very end of the guide. A probe beam is set up with a top-hat imaging scheme. One difference is that with guide β, the probe enters the chamber from the same side as the camera. In guide α, we have to be careful to block the beam after it has passed through the chamber and before it

passes directly into the camera. With such a sensitive camera, it will be good to not have to worry about damaging the camera by accidentally sending the probe beam directly into the camera.

5.8 Guide β Conclusion

There are still many things to do to make guide β operational. The Zeeman slower needs some more optimization, and then we will work on putting together the elements of the Zeeman slower and the pusher to optimize the 2MOT. After we observe both a substantial increase in the 1MOT from the Zeeman slower and a good transfer of atoms from the 1MOT into the 2MOT, we will work to detect the atoms at the end of the guide. As soon as we have any signal at the end of the guide, much effort will be devoted to optimizing the injection coil sequence timing and relative current in each coil.

The ultimate goal is to make a continuous atom laser. This is by far the most promising attempt yet.

CHAPTER VI

Outlook

Many tasks are needed yet before the atom laser will function as expected. In this closing chapter, I will outline several of these.

6.1 Detection of Atoms at the End of Guide β

Though the detection is set up at the end of guide β, we have yet to see atoms at the end of this guide. Many factors have contributed to the delay, but this remains the first priority in the operation of guide β. To have the best chance of detecting atoms, we need to have the Zeeman slower maximizing the atom count of the 1MOT, the pusher beam transferring atoms nicely into the 2MOT, and control of at least one of the injection coils all working at the same time.

The plan, after optimizing the atoms in the 2MOT, is to suddenly turn on either injection coil -1 or -2 (located behind the 2MOT) to give the atoms within the 2MOT a momentum kick. This should send a pulse of atoms into the guide. If we have the probe set up correctly, we should be able to see this pulse of atoms pass by the camera at the end of the guide. Once we see the atoms, we will be able to optimize all parameters on that atomic signal.

6.2 Transverse Cooling

To increase the capture of atoms in the 1MOT, we plan to employ transverse cooling on the Zeeman slower atomic beam [118]. A schematic for transverse cooling is shown in Fig. 6.1. The atomic flow coming out of the oven strongly diverges until it reaches the first transverse cooling stage, TC. The transverse cooling acts almost like a lens, increasing the capture volume (in angle) of the Zeeman slower. The gray areas indicate atoms that would have been lost without the transverse cooling. The main feature of transverse cooling is that by reducing the transverse velocity by some factor, the remaining atoms increase in density by that factor squared. The potential benefit can therefore be quite dramatic.

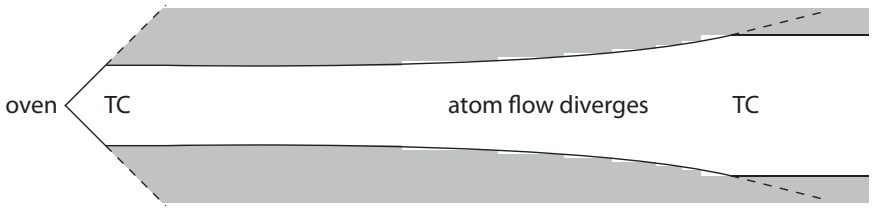

Figure 6.1: Schematic of transverse cooling. The gray areas indicate atoms that would have been lost from the system without the transverse cooling, denoted by TC.

In previous work [114], only one pass of transverse cooling was used at only one point on the Zeeman slower. If we angle the mirrors slightly as sketched in Fig. 6.2, we should be able to get 3 or 4 passes in each direction of transverse cooling light through the chamber. The optimum alignment should be if the beam spots on the mirror are nearly, but not quite, overlapping. We plan to implement this scheme on both transverse axes at both the entrance and the exit of the Zeeman slower.

Transverse cooling like this uses on-resonant light. For our setup, this will involve the use of an additional laser (one currently being used in the experiments in guide α), which is already mostly set up for the transverse cooling. The idea is to reduce the

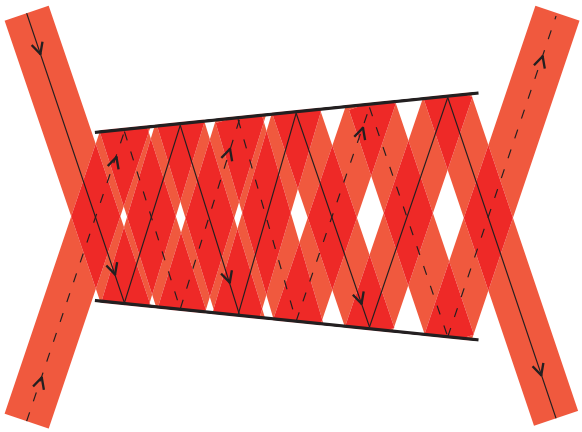

Figure 6.2: Schematic of the beam path for transverse cooling.

transverse velocity of the atomic beam, and the potential benefit is striking. If we would be able to produce a factor of 10 reduction in transverse velocity, we would have a factor of 100 gain in density of the atoms in the beam.

6.3 Replacing Rubidium

The rubidium source within the Zeeman slower's oven has visibly decreased its output relative to what it had been. We can see that the fluorescence coming directly out of the oven is significantly less than it was in the past. When the Zeeman slower was first installed in ∼2006, the oven was loaded with a 5 gram capsule of rubidium. However, it was noted that the construction of the oven needed a minimum amount of about 4 grams to be operational [114]. I think that we are nearing this lower limit.

In order to replace the rubidium, we will have to break vacuum on the Zeeman slower. Thankfully, the gate valves on either side of the 1MOT chamber will allow both guide β and the spiral guide to remain under vacuum even while we have the Zeeman slower open to air. Because we do not know exactly how much rubidium is currently left in the oven, we cannot be sure how we will need to dispose of it. That will be a decision to be made at the time of replacement.

We will need to transport the oven, emptied of the old rubidium sample, to a glove

box. Because rubidium reacts violently with water, we will want to break open the new sample's capsule, which will possibly be as large as 10 g, under an argon flow. We have yet to locate such a facility. The plan is to break the rubidium capsule and heat the rubidium so that it will then cover the inside of the oven, then place a vacuum flange blank over the oven and seal it. We will then remove the newly-filled oven from the glove box, transport it back to the lab, and carefully under a nitrogen backflow remove the blank and reinstall the oven on the Zeeman slower. If a 5 g sample has lasted this long, a 10 g sample should be an ample quantity for the foreseeable future of the Zeeman slower.

6.4 Bias Magnetic Field Control

In order to perform the surface adsorption evaporative cooling discussed in Section 5.5, we need a way to control the distance between the atomic flow and the silicon pieces within the guide. The plan for this is to control the bias magnetic field. The atoms–which are low-field-seeking–will tend closer to magnetic zero. By lowering the bias field, we can drive the magnetic zero closer to the silicon surfaces that are spaced throughout the length of the guide.

6.4.1 Racetrack Coils

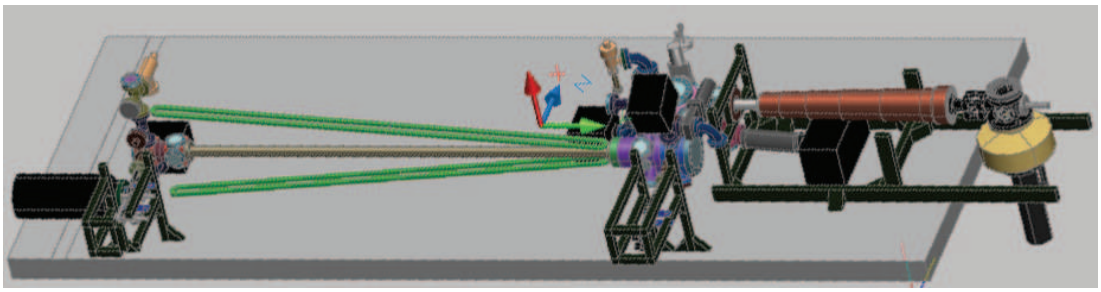

Figure 6.3: Autocad depiction of the entire setup. The proposed racetrack coils are shown in bright green, above and below the guide.

Initially, we planned to alter the bias magnetic field with two very long, racetrack

shaped coils on either side of guide β. An Autocad sketch of this arrangement is shown in Fig. 6.3. The racetrack coils are shown in bright green, above and below the guide. The racetrack coils are angled away from the guide axis, thereby lowering the total bias field that the atoms see as they travel down the guide. This is just a sketch of what they look like; we still need to calculate the field strength that such racetrack coils would produce at the guiding location. The calculation should help determine how many turns we would need on the racetrack, the necessary current, the best angle of inclination relative to the guide, and other such parameters.

6.4.2 Individual Control

A drawback to such a racetrack arrangement is that there is no tunability of the local magnetic field. In much more recent planning session, we discussed the idea of placing individual coil pairs outside the guide, at the z-location of each of the 21 silicon strips. Obviously, this is the ultimate in individual control of the local magnetic field. This may prove difficult to implement, however, in a way that allows for complete individual control of each of the 21 coil pairs. One consideration is the prohibitive cost of 21 power supplies, as well as the lab space that they would take up.

A compromise could be to use 21 small coil pairs, but control them in small groups of perhaps 5-7 coils. Using a relatively simple current divider circuit, we could fairly easily swap out the resistors on each leg of the current divider until reaching the optimum current for each coil. If we implement a scheme such as this, we would want to optimize the atomic flow at the end of the guide for each batch of coils successively, starting closest to the 2MOT. Iteratively tuning the individual magnetic fields should allow for optimum surface adsorption evaporative cooling at all parts of the guide, making the flow of atoms as cold as possible before reaching the end of the guide.

Coil pairs would be significantly easier to design and manufacture than long race-

track coils, so between that and the individual control that coil pairs provide, this looks to be the better option.

6.5 Potential Barrier to Make BEC

Once the atomic density within the guide is sufficient to reach quantum degeneracy, we will need a way to transform the flow of atoms within the guide into a BEC. The somewhat standard way of doing this is by altering the potential that the atoms see, creating a potential barrier to stop the atomic flow. The schematic for this is sketched in Fig. 6.4. The black line represents the total potential that the atoms see. On the left of the figure, this potential has a slight downward slope. This will come from tuning the external magnetic field (see Sec. 6.4), which will bring the atoms closer to the silicon surfaces along the guide.

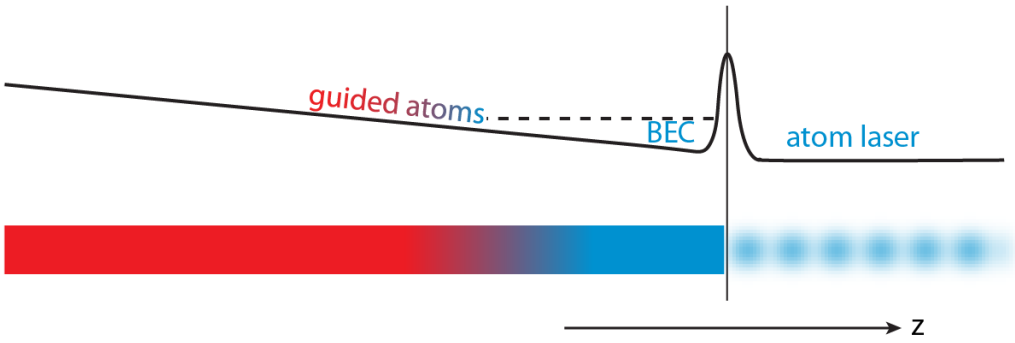

Figure 6.4: Schematic of guided-atoms-to-atom-laser transition. The black line represents the total potential that the atoms see as they travel in the guide.

To stop the atomic flow, we will utilize a potential barrier. On the upstream side of this barrier, the atoms will "bunch up", enabling even more collisions which should finish bring the atoms into the BEC state. Because of the gradual potential decrease leading up to the barrier, atoms flowing in from the guide should not disturb the BEC, but rather experience a cascading effect of joining the atoms within the BEC.

By tuning the exact specifications of the potential barrier, we will allow atoms to tunnel through the barrier. These tunneled atoms will form our atom laser. There

are two ways we can implement this potential barrier at the end of the guide.

6.5.1 Magnetic Potential

The easier solution is to use an extra magnetic field at the end of the guide. While I was assembling guide β, I wrapped a small coil around the guide wires at the end of the guide, as shown in Fig. 6.5. This coil has about 5.5 turns, and the leads of the coil are fed along the guide wires out of the way of the atomic flow, to an electric feed-through of the same type as used with the injection and 2MOT coils.

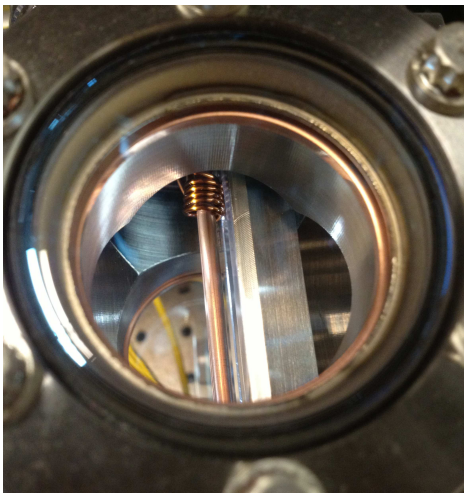

Figure 6.5: Coil just past the detection region at the end of guide β. The light for detection passes through a slit in the support rail visible on the right side of the picture.

By controlling the current in this coil, we could control the height of the magnetic barrier created by this coil. With so many other coils current-controlled as a function of time, it would not be difficult to control this coil in the same way. We could simply use another circuit board, as in Fig. 5.15, to split off a small fraction of the current from our high-current power supply, and control the shape of the current with the same software. If we find that we do not need to change the potential barrier height in time, we could also simply connect this coil to a DC power supply.

The main issue with using such a coil to create a potential barrier is that the

barrier will be incredibly wide. The thinnest barriers possible with a coil are on the order of 1 mm. In order for the rubidium atoms to tunnel through this thick of a barrier, they would have to travel extremely close to the top of the barrier. We would therefore need to be able to control the current in the coil to something on the order of 1 part in 10^6 A, which is experimentally prohibitive.

Therefore, using a coil to make the potential will be a good way to make a continuous BEC with the atoms in our guide, but it will not work to make an atom laser. It will still be the first method that we try though, since there are many important parameters that we will need to investigate with a continuous BEC before we will work on the atom laser outcoupling. These include studying the loading dynamics of the continuous BEC, investigating the number fluctuations (both number change and time dependence) that may arise from possible instabilities in the atomic flux, and analyzing the dynamics of a system that begins as a classical gas and ends as a quantum gas.

6.5.2 Light Shield Barrier

A different method for altering the potential at the end of the guide is to use a light shield barrier. The light barrier is formed by a focused, blue-detuned laser beam. From close to the beginning of BEC studies, such a barrier has been used as a mirror to reflect a BEC [119]. More recently, there has been at least one study of the tunneling transmission through a light barrier as a function of the light's intensity [120].

In our setup, we will make a light barrier from a 12 Watt Coherent Verdi laser, which has a wavelength of 532 nm. This is a frequency doubled Nd:YVO4 (Neodymium doped Yttrium Orthovanadate) laser. With a broad absorption peak, this "vanadate" crystal can be pumped at high efficiency over a wide wavelength range. The laser was purchased with the intent of primarily being a light barrier for the spiral guide, but with the idea that it could also be used for guide β. Since it is likely that guide β

will come online before the spiral guide, it seems that the Verdi could be tested on the linear guide before the spiral guide.

Because 532 nm is far blue-detuned, the potential that the atoms see from this light is repulsive. This can act as the barrier shown in Fig. 6.4, creating a localized 3D potential well along with the magnetic potential from the guide wires in the transverse directions. The BEC will form upstream of the light shield, which is situated transverse to the guiding direction. For optimum performance of the atom laser, we will want this BEC to be as large as possible. Therefore, we will want to optimize the evaporative cooling efficiency, the flux of atoms into the guide, the transfer of guided atoms into the BEC, etc.

We estimate that we will want to use about 1 W of the Verdi light to make a barrier that is on the order of 1 μm thick. To have stable control of the tunneling, we will need to control the intensity of this beam to something on the order of 1 part in 1000, which is experimentally realizable.

By tuning the barrier height of the light shield, we will be able to control the tunneling rate of the atoms through the barrier, forming the coherent matter waves of a continuous atom laser. This is commonly done with the intensity of the light. Alternatively, and possibly as a first step to then be refined by the intensity, is adjusting the width (the extent in the z-direction) of the sheet of light, which would involve adjusting the optics that focus said light into a sheet.

One issue that could arise with the use of the Verdi laser to make a light shield barrier at the end of the guide is that the viewports in the region where it will be used are anti-reflection coated for 780 nm light, but not for 532 nm light. It is unknown if this will be a problem; the viewports on the spiral guide are anti-reflection coated for both wavelengths. We estimate that no damage should occur to the windows if we use a large beam (diameter of 1 cm or so) along with a high numerical aperture lens to focus the beam into the small spot size needed for the light sheet.

6.6 Atom Interferometer?

The current setup of guide β does not have much physical space beyond the location where the atom laser will form. Assuming that forming a BEC works and that we are able to create a flux of coherent atoms tunneling out of the BEC to make an atom laser, we will need a way to utilize the atom laser output. It is almost certain that the vacuum chamber will need to be extended for this purpose.

At present, there are only a couple of inches of space beyond the BEC region before reaching the end of the chamber. A chamber redesign of this end could include space to perform atom interferometry, which is one of the most popular applications of atom lasers. Space on the optics table is slightly limited by the TSP (titanium sublimation pump), but if absolutely necessary it could be moved farther away from the guide with the addition of another vacuum nipple.

If a new section of vacuum chamber is added, I would suggest attempting to fully form its construction before breaking vacuum on guide β, which should hopefully limit the time that the present chamber would be open to air when joining the next section. I think that the functionality of the atom laser should be proven before too much time is spent designing experiments to utilize said atom laser.

6.7 Final Thoughts

As outlined here, there are several tasks left to complete before the atom laser will be fully operational. It is my hope that a new graduate student will be able to finish the work that remains. I would love for the work that I have done to be a contributing factor in the first continuous atom laser.

APPENDICES

APPENDIX A

Number of Rydberg Atoms

In the experiment presented in Chapter III, where Rydberg atom interactions are studied, it is useful to estimate the initial Rydberg atom number and density. Theoretically, the number of Rydberg atoms is calculated as

$$N_{5\mathrm{P}} P_{\mathrm{exc}} V \tag{A.1}$$

The density of 5P atoms, $N_{5\mathrm{P}}$, approximately equals half the incident atomic beam density N_{g} because the lower transition is saturated within the excitation volume V. Using results of an earlier atomic beam density measurement [49], $N_{\mathrm{g}} \sim 10^9$ cm^{-3}. The excitation probability [52] is

$$P_{\mathrm{exc}} = \sigma_{\mathrm{Ryd}} \left(\frac{E_{\mathrm{exc}}}{h\nu A} \right) \tag{A.2}$$

where the photoionization laser has energy $h\nu$, the excitation area is A, the energy of the upper-transition excitation pulse is $E_{\mathrm{exc}} = 2.5$ nJ and the excitation cross section is

$$\sigma_{\mathrm{Ryd}} = \sigma_{\mathrm{PI}} \left(\frac{27.2\mathrm{eV}/n^{*3}}{h\nu_{\mathrm{L}}} \right) \tag{A.3}$$

There,

$$\sigma_{\mathrm{PI}} = 1.2 \times 10^{-17}\ \mathrm{cm}^2 \tag{A.4}$$

is the photoionization cross section of $5P_{3/2}$ [121], $n^* = 57.7$ is the effective principal quantum number (since we have 59D, and the D state quantum defect is 1.34), and $\nu_{\mathrm{L}} = 20$ MHz is the measured excitation bandwidth of the $59D_{5/2}$ Rydberg level. The excitation area A cancels with the volume V leaving only the length of the excitation region, which is equivalent to the diameter of the region filled with 5P atoms. This is on the order of 100 μm. Taking into account the overall Rydberg atom detection efficiency (15% for free ions, as described in the Rydberg atom section), we calculate an expected yield of 100 detected ion counts per experimental cycle.

We detect an initial number of $\sim$30 ions per experimental cycle by integrating over the microwave ionization signal or the field ionization signal for $t_{\mathrm{d}} = 5$ μs (immediate detection). Factoring in the detection efficiency of 15% and estimating that the excitation volume is a cylindrical region of 50 μm radius and 100 μm height, the actual number of Rydberg atoms initially present is $\sim$200 per experimental cycle and the corresponding density is of order 2×10^8 cm^{-3}. This is such a low density that Coulomb repulsion of the extracted ions is neither expected nor observed. Though this density is fairly low, it is sufficient to cause a fraction of the atoms to Penning ionize immediately following excitation and to l-mix due to Rydberg-atom collisions, as was discussed in Section 3.3.

We observe about 30 ions using either field or microwave ionization, and attribute the difference to an overestimation of the ground state atomic beam density. The actual number of Rydberg atoms present in the system is about 200 per experimental cycle, corresponding to a density of 2×10^8 cm^{-3}.

APPENDIX B

Statistical Weighting

The simulation for Rydberg guiding (Section 3.3) uses "proper statistical weighting" to determine the (ℓ, j, m_j)-quantum numbers. Let's explore what is meant by this phrase.

For a given value of n, ℓ can take on values from 0 to $n-1$. There are two different ways to think about the number of quantum states that are possible. One way is to consider the number of different pairs of values that m_ℓ and m_s can take on. For each of the $2\ell+1$ possible values of m_ℓ, there are 2 values of m_s, so that means a total of $4\ell+2$ different quantum states. Alternatively, and more intuitively for our purposes, you can think about the $(2j+1)$ values of possible m_j summed over the two possibilities of j: $j=\ell+1/2$ and $j=\ell-1/2$. So then $\sum_j 2j+1 = 2*(\ell+1/2)+1+2*(\ell-1/2)+1 = 4\ell+2$ as the weighting factor for ℓ. Therefore, in one n-shell, there are

$$\sum_{\ell=0}^{n-1}(4\ell+2) = 4\frac{(n-1)n}{2} + 2n = 2n^2 - 2n + 2n = 2n^2 \tag{B.1}$$

possible quantum states.

So there are $4\ell+2$ possibilities for ℓ out of a total of $2n^2$ states. Thus,

$$P(\ell) = \frac{4\ell + 2}{2n^2} \tag{B.2}$$

Once an ℓ is determined, the next step is j. This uses the values from the above paragraph:

$$P(j = \ell + \frac{1}{2}) = \frac{\ell + 1}{2\ell + 1} \tag{B.3a}$$

$$P(j = \ell - \frac{1}{2}) = \frac{\ell}{2\ell + 1} \tag{B.3b}$$

Technically, $\ell = 0$ needs a slightly modified treatment since $\ell - \frac{1}{2}$ does not exist since j has to be positive.

Once a j is determined, m_j has values from $-j$ to j with equal probability, so

$$P(m_j) = \frac{1}{2j + 1} \tag{B.4}$$

where $2j + 1$ is the total number of allowed j values.

APPENDIX C

Photon Scattering

It can be quite useful to calculate the number of photons that a given atom will scatter. Up to a certain limit, more light means that the atoms will scatter more photons. Here, we will examine number of photons scattered from the R10 and R12 beams during the optical pumping experiments.

Equation 2.24b from [100] defines the saturation parameter as

$$s_0 = I/I_{\text{sat}} \tag{C.1}$$

where $I_{\text{sat}} = 3.577$ mW/cm^2 is the "shell averaged" saturation intensity (listed as "isotropic light polarization" in [122]).

The R10 beam has a FWHM diameter of 380 μm and the R12 is 370 μm. For 80 nW in R10, this gives an intensity of 0.071 mW/cm^2 and $s_0 = 0.0197$. For 9.6 nW in R12, the intensity is 0.0089 mW/cm^2 and $s_0 = 0.0025$.

The scattering rate is calculated with

$$\gamma_p = \frac{s_0\gamma/2}{1 + s_0 + (2\delta/\gamma)^2} \tag{C.2}$$

We will consider just the on-resonant case, so $\delta = 0$. That makes

$$\gamma_p = \frac{s_0\gamma/2}{1+s_0} \tag{C.3}$$

The laser linewidth is $\gamma = 6$ MHz $\times 2\pi$. Plugging these values in gives $\gamma_{p,R10} = 365000$ s^{-1} and $\gamma_{p,R12} = 47000$ s^{-1}.

To determine the number of photons scattered, we have to know the time it takes the atoms to traverse the beam diameters. For a good portion of the optical pumping experiments, we used a launch velocity of 2.4 m/s, meaning that in the horizontal section of the guide the atoms were traveling at $\sim$0.88 m/s (see Table 4.1). Therefore, using the diameters mentioned above, $t_{R10} = 0.00043$ s and $t_{R12} = 0.00042$ s.

Multiplying the time by the scattering rate, we see that we scatter about 93 photons from R10 and 16 photons from R12 at this velocity and beam power. These numbers are quoted in Section 4.1.

APPENDIX D

Labview VIs

The experiments in guide α are all controlled with Labview VIs (virtual instruments). Labview is a curious programming language, in that you program by wiring the different components together in the block diagram. For most people, there is a steep learning curve to certain aspects of programming in Labview, especially as the programs become increasingly complex. A list of the major categories of Labview programs used in the experiments within this thesis is given in Table D.1, though many of these have various versions that each operate in slightly different ways depending on the exact context of the experiment. There are also a very large number of experiment-specific VIs that interact with some of the variables in these through the use of "global variables", which can have a value change from one VI reflected in all other operating VIs with the same variable. A large number of the VIs in use are intertwined in this way. We also have an extremely large library of subVIs that have been developed over the years for a wide range of applications.

When we decided to operate the MMOT in a pulsed manner (see Section 4.2), the analog output control VI needed a major overhaul. To pulse the MMOT, I programmed our analog VI to change the value of the frequency modulation feeds to the acousto-optic (AO) modulators that shift our up-going and down-going MMOT

Category	Description
Analog output control	Controls the 16 analog output channels of the UEI analog card. These are used mainly for the AO frequencies and amplitudes. For different experiments, they have also been used to apply voltages to various electrodes, as well as sending a trigger to the delay generator.
Timing	Controls the 8 output channels of the Adlink timing card. These are used for the majority of the timing applications of the experiment. A particular example is setting t_d, as discussed in Fig. 3.1.
Power supply	Controls the current on the guide wires, slowly incrementing and decrementing the current value as we turn the guide wires on and off of their full value of $\sim$200 A.
Scope download	Downloads traces from the oscilloscope for later analysis. This saves the scope trace as a text file, which is easy to plot.
Gevicam	Controls the Gevicam camera imaging the MCP. This program can be used to average a specified number of images, and is used as a subVI within many experiment-specific VIs.
Device initialization	Many of the devices used (delay generator, multiscaler, arbitrary waveform generator, etc.) need to be initialized before the computer can communicate with them. Each of these has a small, individual VI to run before operating the main programs.

Table D.1: List of the major categories of Labview VIs used in the atom laser project.

beams from the lockpoint of the laser (for more on that, see Chapter II, particularly Fig. 2.6). By changing the frequency on both beams, I can switch the MMOT from "launched" (where the frequency difference between the beams sets up a moving reference frame for the atoms which sends them upward with a certain velocity determined by the frequency difference, given by Equation 2.1) to "unlaunched" (where both beams have the same frequency, placing the atoms in a stationary confinement). Labview has a built-in timing mechanism, so I was able to program the unlaunched and launched time from this VI alone. At the start of this sequence, I sent a trigger from the analog program to the delay generator, which then controlled the rest of the timing for the optical pumping experiments.

The version of the analog control VI used for the optical pumping experiments was already significantly more complex than the one we used to control the Rydberg atom guiding experiments. For the Rydberg guiding, the front panel for the analog control program is indicated in Fig. D.1(a) by the dashed red box, where the entire (a) shows the front panel for the optical pumping. Adding this many different components to the front significantly increased the complexity of the block diagram, where the programming actually takes place, as well. Fig. D.1(b) gives a small sample of the current block diagram. In this particular panel shown, there is a while loop, a for loop, numerous "stacked sequence" panels that each have anywhere from 2 to 9 panels (most of which have sub-panels), several "flat sequence" panels, an "event structure" with 10 different events (which each have their own panels to program), a "case structure", and too many "local variables" to count. The evolution of the Rydberg guiding VI to this one occurred over a period of several months.

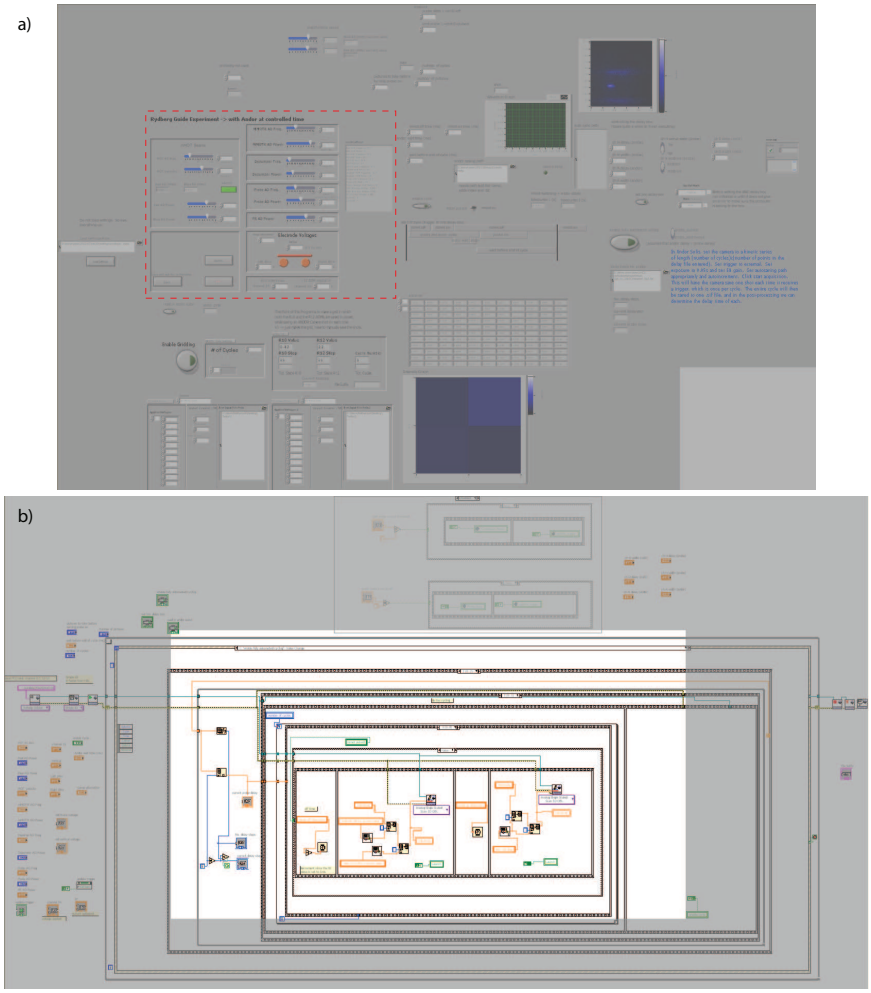

Figure D.1: Example of the Labview programming. (a) shows the front panel and (b) shows the block diagram.

APPENDIX E

Rubidium Cooler: a Fix for Both Guides

One issue that has occurred in both guide α and guide β is flooding the primary chamber with too much rubidium. In both cases, the concentration of rubidium was high enough that it visibly crystalized on the inside of the viewports. A combination of hot and cold was used to correct the situation. Heat tapes were used to bake the rubidium off the glass, but we found that this redistributed it to other parts of the chamber so we needed a more permanent solution.

For guide α, Karl Lundquist (an undergrad in our lab) machined a piece to match the curvature of the outside of the PMOT chamber. To this, we attached a thermo-electric cooler (TEC) and a heat sink. By controlling the current through the TEC, we make the roof of the chamber where this is attached quite cold. The rubidium gathers to the cold spot. Looking up into the PMOT chamber, there is a large deposit of rubidium on the wall directly beneath this cooling apparatus.

We repeated this method in guide β, though guide β was more severely flooded and took longer to bake off. Matt Boguslawski (another undergrad) made a very similar cooling device and attached it to the nipple that holds the rubidium reservoir. With the rubidium collecting there, we should be able to reuse some of it by heating the nipple, should the chamber need additional rubidium added at a later time. For

the cooling device on each guide, a fan helps to cool the heat sink on the hot side of the TEC.

Since the installation of these cooling devices on the respective guides, we have had no recurrent issues with the rubidium pressure in the chambers, nor with recrystallization of the chamber viewports.

BIBLIOGRAPHY

BIBLIOGRAPHY

[1] D. Döring, G.R. Dennis, N.P. Robins, M. Jeppesen, C. Figl, J.J. Hope, and J.D. Close. Pulsed pumping of a bose-einstein condensate. *Phys. Rev. A*, 79:063630, 2009.

[2] H. M. Wiseman. Defining the (atom) laser. *Phys. Rev. A*, 56, 1997.

[3] M. Holland, K. Burnett, C. Gardiner, J. I. Cirac, and P. Zoller. Theory of an atom laser. *Phys. Rev. A*, 54:R1757–R1760, 1996.

[4] M. Kasevich and S. Chu. Measurement of the gravitational acceleration of an atom with a light-pulse atom interferometer. *Appl. Phys. B*, 54:321–332, 1992.

[5] Alexander D. Cronin, Jörg Schmiedmayer, and David E. Pritchard. Optics and interferometry with atoms and molecules. *Rev. Mod. Phys.*, 81:1051, 2009.

[6] Stephan Wildermuth, Sebastian Hofferberth, Igor Lesanovsky, Elmar Haller, L. Mauritz Andersson, Sönke Groth, Israel Bar-Joseph, Peter Krüger, and Jörg Schmiedmayer. Boseeinstein condensates: Microscopic magnetic-field imaging. *Nature*, 435:440, 2005.

[7] J. M. McGuirk, G. T. Foster, J. B. Fixler, M. J. Snadden, and M. A. Kasevich. Sensitive absolute-gravity gradiometry using atom interferometry. *Phys. Rev. A*, 65:033608, 2002.

[8] Mark A. Kasevich. Coherence with atoms. *Science*, 298:1363, 2002.

[9] Y. Shin, C. Sanner, G.-B. Jo, T. A. Pasquini, M. Saba, W. Ketterle, and D. E. Pritchard. Interference of bose-einstein condensates split with an atom chip. *Phys. Rev. A*, 72:021604(R), 2005.

[10] T. L. Gustavson, P. Bouyer, and M. A. Kasevich. Precision rotation measurements with an atom interferometer gyroscope. *Phys. Rev. Lett.*, 78, 1997.

[11] O. Zobay, E. V. Goldstein, and P. Meystre. Atom holography. *Phys. Rev. A*, 60:3999–4005, 1999.

[12] J. H. Thywissen, K. S. Johnson, R. Younkin, N. H. Dekker, K. K. Berggren, A. P. Chu, and M. Prentiss. Nanofabrication using neutral atomic beams. *J. Vac. Sci. Technol. B*, 15:2093–2100, 1997.

[13] M. H. Anderson, J. R. Ensher, M. R. Matthews, C. E. Wieman, and E. A. Cornell. Observation of bose-einstein condensation in a dilute atomic vapor. *Science*, 269:198–201, 1995.

[14] C. C. Bradley, C. A. Sackett, J. J. Tollett, and R. G. Hulet. Evidence of bose-einstein condensation in an atomic gas with attractive interactions. *Phys. Rev. Lett.*, 75:1687–1691, 1995.

[15] K. B. Davis, M.-O. Mewes, M. R. Andrews, N. J. van Druten, D. S. Durfee, D. M. Kurn, and W. Ketterle. Bose-einstein condensation in a gas of sodium atoms. *Phys. Rev. Lett.*, 75:3969–3974, 1995.

[16] Tilman Esslinger, Immanuel Bloch, and Theodor W. Hänsch. Bose-einstein condensation in a quadrupole-ioffe-configuration trap. *Phys. Rev. A*, 58, 1998.

[17] D. M. Stamper-Kurn, M. R. Andrews, A. P. Chikkatur, S. Inouye, H.-J. Miesner, J. Stenger, and W. Ketterle. Optical confinement of a bose-einstein condensate. *Phys. Rev. Lett.*, 80, 1998.

[18] Y. Colombe, E. Knyazchyan, O. Morizot, B. Mercier, V. Lorent, and H. Perrin. Ultracold atoms confined in rf-induced two-dimensional trapping potentials. *Europhys. Lett.*, 67:593–599, 2004.

[19] M. R. Andrews, C. G. Townsend, H.-J. Miesner, D. S. Durfee, D. M. Kurn, and W. Ketterle. Observation of interference between two bose condensates. *Science*, 275:637, 1997.

[20] R. E. Sapiro, R. Zhang, and G. Raithel. Atom interferometry using kapitza-dirac scattering in a magnetic trap. *Phys. Rev. A*, 79:043630, 2009.

[21] M.-O. Mewes, M. R. Andrews, D. M. Kurn, D. S. Durfee, C. G. Townsend, and W. Ketterle. Output coupler for bose-einstein condensed atoms. *Phys. Rev. Lett.*, 78, 1997.

[22] H. Steck, M. Naraschewski, and H. Wallis. Output of a pulsed atom laser. *Phys. Rev. Lett.*, 80, 1998.

[23] Immanuel Bloch, Theodor W. Hänsch, and Tilman Esslinger. Atom laser with a cw output coupler. *Phys. Rev. Lett.*, 82, 1999.

[24] E. W. Hagley, L. Deng, M. Kozuma, J. Wen, K. Helmerson, S. L. Rolston, and W. D. Phillips. A well-collimated quasi-continuous atom laser. *Science*, 283:1706, 1999.

[25] J. E. Debs, D. Döring, N. P. Robins, C. Figl, P. A. Altin, and J. D. Close. A two-state raman coupler for coherent atom optics. *Opt. Expr.*, 17:2319, 2009.

[26] Michael Köhl, Theodor W. Hänsch, and Tilman Esslinger. Measuring the temporal coherence of an atom laser beam. *Phys. Rev. Lett.*, 87:160404, 2001.

[27] Anton Öttl, Stephan Ritter, Michael Köhl, and Tilman Esslinger. Correlations and counting statistics of an atom laser. *Phys. Rev. Lett.*, 95:090404, 2005.

[28] I. Bloch, T. W. Hänsch, and T. Esslinger. Measurement of the spatial coherence of a trapped bose gas at the phase transition. *Nature*, 403:166, 2000.

[29] B. P. Anderson and M. A. Kasevich. Macroscopic quantum interference from atomic tunnel arrays. *Science*, 282:1686, 1998.

[30] J.E. Debs, D. Döring, P.A. Altin, C. Figl, J. Dugué, M. Jeppesen, J.T. Schultz, N.P. Robins, and J.D. Close. Experimental comparison of raman and rf outcouplers for high-flux atom lasers. *Phys. Rev. A*, 81:013618, 2010.

[31] Y. Le Coq, J. H. Thywissen, S. A. Rangwala, F. Gerbier, S. Richard, G. Delannoy, P. Bouyer, and A. Aspect. Atom laser divergence. *Phys. Rev. Lett.*, 87, 2001.

[32] Michael Köhl, Theodor W. Hänsch, and Tilman Esslinger. Continuous detection of an atom laser beam. *Phys. Rev. A*, 65:021606(R), 2002.

[33] R. J. Ballagh, K. Burnett, and T. F. Scott. Theory of an output coupler for bose-einstein condensed atoms. *Phys. Rev. Lett.*, 78:1607, 1997.

[34] Jens Schneider and Axel Schenzle. Output from an atom laser: theory vs. experiment. *Appl. Phys. B*, 69:353, 1999.

[35] P. Cren, C.F. Roos, A. Aclan, J. Dalibard, and D. Guéry-Odelin. Loading of a cold atomic beam into a magnetic guide. *Eur. Phys. J. D*, 20:107–116, 2002.

[36] J. M. Vogels, T. Lahaye, C. Roos, J. Dalibard, and D. Guéry-Odelin. How to reach the collisional regime on a magnetically guided atomic beam. *J. Phys. IV France*, 1, 2003.

[37] T. Lahaye, J.M. Vogels, K.J. Günter, Z. Wang, J. Dalibard, and D. Guéry-Odelin. Realization of a magnetically guided atomic beam in the collisional regime. *Phys. Rev. Lett.*, 93:093003, 2004.

[38] Thierry Lahaye and David Guery-Odelin. Kinetics of the evaporative cooling of an atomic beam. *Phys. Rev. A*, 73:063622, 2006.

[39] M. Key, I. G. Hughes, W. Rooijakkers, B. E. Sauer, and E. A. Hinds. Propagation of cold atoms along a miniature magnetic guide. *Phys. Rev. Lett.*, 84:1371–1373, 2000.

[40] Michael J. Renn, Elizabeth A. Donley, Eric A. Cornell, Carl E. Wieman, and Dana Z. Anderson. Evanescent-wave guiding of atoms in hollow optical fibers. *Phys. Rev. A*, 53:R648–R651, 1996.

[41] W. Guerin, J.-F. Riou, J. P. Gaebler, V. Josse, P. Bouyer, and A. Aspect. Guided quasi-continuous atom laser. *Phys. Rev. Lett.*, 97:200402, 2006.

[42] K. Brugger, P. Krüger, X. Luo, S. Wildermuth, H. Gimpel, M. W. Klein, S. Groth, R. Folman, I. Bar-Joseph, and J. Schmiedmayer. Two-wire guides and traps with vertical bias fields on atom chips. *Phys. Rev. A*, 72:023607, 2005.

[43] Peter D. D. Schwindt, Eric A. Cornell, Tetsuo Kishimoto, Ying-Ju Wang, and Dana Z. Anderson. Efficient loading of a magnetic waveguide on an atom chip. *Phys. Rev. A*, 72:023612, 2005.

[44] Jø'zsef Fortǵh and Claus Zimmermann. Magnetic microtraps for ultracold atoms. *Reviews of Modern Physics*, 79:235–289, 2007.

[45] E. P. Power, L. George, B. Vanderelzen, P. Herrera-Fierro, R. Murphy, S. M. Yalisove, and G. Raithel. Design and fabrication of a chip-based continuous-wave atom laser. *arXiv*, 1202.0479v1, 2012.

[46] A. Couvert, M. Jeppesen, T. Kawalec, G. Reinaudi, R. Mathevet, and D. Guéry-Odelin. A quasi-monomode guided atom laser from an all-optical bose-einstein condensate. *EPL*, 83:50001, 2008.

[47] N.P. Robins, C. Figl, M. Jeppesen, G.R. Dennis, and J.D. Close. A pumped atom laser. *Nature Physics*, 4:731–736, 2008.

[48] Philip Nelson. *Biological Physics: Energy, Information, Life*. W. H. Freeman and Company, 2004.

[49] Spencer E. Olson, Rahul R. Mhaskar, and Georg Raithel. Continuous propagation and energy filtering of a cold atomic beam in a long high-gradient magnetic atom guide. *Phys. Rev. A*, 73:033622, 2006.

[50] R.R. Mhaskar, S.E. Olson, and G. Raithel. Open-channel fluorescence imaging of atoms in high-gradient magnetic fields. *Eur. Phys. Journal D*, 41:221–227, 2007.

[51] Spencer E. Olson. *Long High-Gradient Magnetic Atom Guide and Progress Towards an Atom Laser*. PhD thesis, University of Michigan, 2006.

[52] Thomas F. Gallagher. *Rydberg Atoms*. Cambridge University Press, 1994.

[53] R. F. Stebbings and F. B. Dunning. *Rydberg states of atoms and molecules*. Cambridge University Press, 1983.

[54] J. L. Wiza. Microchannel plate detectors. *Nucl. Instrum. Methods*, 162:587–601, 1979.

[55] V. Vaidya, M. Traxler, C. Hempel, R. Mhaskar, and G. Raithel. Ion imaging in a high-gradient magnetic guide. *Rev. Sci. Ins.*, 81:043109, 2010.

[56] O. Mülken, A. Blumen, T. Amthor, C. Giese, M. Reetz-Lamour, and M. Weidemüller. Survival probabilities in coherent exciton transfer with trapping. *Phys. Rev. Lett.*, 99:090601, 2007.

[57] Markus Müller, Linmei Liang, Igor Lesanovsky, and Peter Zoller. Trapped rydberg ions: from spin chains to fast quantum gates. *New J. Phys.*, 10:093009, 2008.

[58] H. Weimer, R. Löw, T. Pfau, and H. P. Büchler. Quantum critical behavior in strongly interacting rydberg gases. *Phys. Rev. Lett.*, 101:250601, 2008.

[59] T. Pohl, E. Demler, and M. D. Lukin. Dynamical crystallization in the dipole blockade of ultracold atoms. *PRL*, 104:043002, 2010.

[60] M. D. Lukin, M. Fleischhauer, R. Cote, L. M. Duan, D. Jaksch, J. I. Cirac, and P. Zoller. Dipole blockade and quantum information processing in mesoscopic atomic ensembles. *Phys. Rev. Lett.*, 87:037901, 2001.

[61] M. Saffman, T. D. Walker, and K. Mølmer. Quantum information with rydberg atoms. *Rev. Mod. Phys.*, 82:2313, 2010.

[62] J.-H. Choi, J. R. Guest, A. P. Povilus, E. Hansis, and G. Raithel. Magnetic trapping of long-lived cold rydberg atoms. *Phys. Rev. Lett.*, 95:243001, 2005.

[63] S. D. Hogan and F. Merkt. Demonstration of three-dimensional electrostatic trapping of state-selected rydberg atoms. *Phys. Rev. Lett.*, 100:043001, 2008.

[64] S. E. Anderson, K. C. Younge, and G. Raithel. Trapping rydberg atoms in an optical lattice. *Phys. Rev. Lett.*, 107:263001, 2011.

[65] I. Lesanovsky, J. Schmiedmayer, and P. Schmelcher. Rydberg atoms in a magnetic guide. *Phys. Rev. A*, 70:043409, 2004.

[66] I. Lesanovsky, J. Schmiedmayer, and P. Schmelcher. Rydberg atoms in magnetic quadrupole traps. *Europhys. Lett.*, 65:478–484, 2004.

[67] I. Lesanovsky and P. Schmelcher. Magnetic trapping of ultracold rydberg atoms. *Phys. Rev. Lett.*, 95:053001, 2005.

[68] B. Hezel, I. Lesanovsky, and P. Schmelcher. Controlling ultracold rydberg atoms in the quantum regime. *Phys. Rev. Lett.*, 97:223001, 2006.

[69] U. Schmidt, I. Lesanovsky, and P. Schmelcher. Ultracold rydberg atoms in a magneto-electric trap. *J. Phys. B: At. Mol. Opt. Phys.*, 40:1003, 2007.

[70] M. Mayle, I. Lesanovsky, and P. Schmelcher. Magnetic trapping of ultracold rydberg atoms in low angular momentum states. *Phys. Rev. A*, 80:053410, 2009.

[71] M. Mayle, B. Hezel, I. Lesanovsky, and P. Schmelcher. One-dimensional rydberg gas in a magnetoelectric trap. *Phys. Rev. Lett.*, 99:113004, 2007.

[72] D. Jaksch, K. I. Cirac, P. Zoller, S. L. Rolston, R. Côté, and M. D. Lukin. Fast quantum gates for neutral atoms. *Phys. Rev. Lett.*, 85:2208–2211, 2000.

[73] A. Speck, C. H. Storry, E. A. Hessels, and G. Gabrielse. Laser-controlled production of rydberg positronium via charge exchange collisions. *Phys. Lett. B*, 597:257–262, 2004.

[74] F. Robicheaux. Three-body recombination for electrons in a strong magnetic field: Magnetic moment. *Phys. Rev. A*, 73:033401, 2006.

[75] Alpha Collaboration. Confinement of antihydrogen for 1000 seconds. *Nature Physics*, 7:558–564, 2011.

[76] N. H. Dekker, C. S. Lee, V. Lorent, J. H. Thywissen, S. P. Smith, M. Drndic', R. M. Westervelt, and M. Prentiss. Guiding neutral atoms on a chip. *Phys. Rev. Lett.*, 84:1124–1127, 2000.

[77] Ke Min, Li Xiao-Lin, and Wang Yu-Zhu. Guiding neutral atoms with two current-carrying wires and a vertical bias field on the atom chip. *Chinese Phys. Lett.*, 25:907, 2008.

[78] S. D. Hogan, J. A. Agner, F. Merkt, T. Thiele, S. Filipp, and A. Wallraff. Driving rydberg-rydberg transitions from a coplanar microwave waveguide. *Phys. Rev. Lett.*, 108:063004, 2012.

[79] M. Traxler, R.E. Sapiro, C. Hempel, K. Lundquist, E.P. Power, and G. Raithel. Guiding of rydberg atoms in a high-gradient magnetic guide. *Phys. Rev. A*, 86:023414, 2012.

[80] M. R. Flannery and D. Vrinceanu. Quantal and classical radiative cascade in rydberg plasmas. *Phys. Rev. A*, 68:030502, 2003.

[81] A. Walz-Flannigan, J. R. Guest, J.-H Choi, and G. Raithel. Cold-rydberg-gas dynamics. *Phys. Rev. A*, 69:063405, 2004.

[82] J. O. Day, E. Brekke, and T. G. Walker. Dynamics of low-density ultracold rydberg gases. *Phys. Rev. A*, 77:052712, 2008.

[83] S. D. Chao, M. Hayashi, S. H. Lin, and E. W. Schlag. l-mixing dynamics of rydberg states of hydrogen atom in a static electric field. *J. Phys. B: At. Mol. Opt. Phys.*, 31:2007–2021, 1998.

[84] F. Robicheaux. Ionization due to the interaction between two rydberg atoms. *J. Phys. B: At. Mol. Opt. Phys.*, 38:S333–S342, 2005.

[85] J. G. Leopold and I. C. Percival. Microwave ionization and excitation of rydberg atoms. *Phys. Rev. Lett.*, 41, 1978.

[86] R. Stephen Berry. The theory of penning ionization. *Radiation Research*, 59:267–275, 1974.

[87] S.K. Dutta, D. Feldbaum, A. Walz-Flannigan, J. R. Guest, and G. Raithel. High-angular-momentum states in cold rydberg gases. *PRL*, 86, 2001.

[88] C. A. Arango, M. Shapiro, and P. Brumer. Cold atomic collisions: Coherent control of penning and associative ionization. *Phys. Rev. Lett.*, 97:193202, 2006.

[89] A. Reinhard, T. Cubel Liebisch, K. C. Younge, P. R. Berman, and G. Raithel. Rydberg-rydberg collisions: Resonant enhancement of state mixing and penning ionization. *PRL*, 100:123007, 2008.

[90] P. J. Tanner, J. Han, E. S. Shuman, and T. F. Gallagher. Many-body ionization in a frozen rydberg gas. *Phys. Rev. Lett.*, 100:043002, 2008.

[91] E. J. Beiting, G. F. Hildebrandt, F. G. Kellert, G. W. Foltz, K. A. Smith, and et al. The effects of 300 k background radiation on rydberg atoms. *J. Chem. Phys.*, 70:3551, 1979.

[92] T. F. Gallagher and W. E. Cooke. The detection of 300k blackbody radiation with rydberg atoms. *Appl. Phys. Lett.*, 34:369, 1979.

[93] W. E. Cooke and T. F. Gallagher. Effects of blackbody radiation on highly excited atoms. *Phys. Rev. A*, 21, 1980.

[94] A. Nussenzweig, J. Hare, A. M. Steinberg, L. Moi, M. Gross, and S. Haroche. A continuous beam of circular rydberg atoms for fundamental tests and applications in metrology. *Europhys. Lett.*, 14:755, 1991.

[95] D. Delande and J. C. Gay. A new method for producing circular rydberg states. *Europhysics Letters*, 5:303, 1988.

[96] G. Raithel, C. Wagner, H. Walther, L. Narducci, and M. Scully. *Cavity Quantum Electrodynamics*. Academic Press, 1994.

[97] S. Haroche. Cavity quantum electrodynamics: a review of rydberg atom-microwave experiments on entanglement and decoherence. *AIP Conf. Proc.*, 464:45, 1999.

[98] J. Hare, A. Nussenzweig, C. Gabbanini, M. Weidemuller, P. Goy, M. Gross, and S. Haroche. Toward a rydberg constant measurement on circular atoms. *IEEE Transactions on Instrumentation and Measurement*, 42:331–334, 1993.

[99] R. Lutwak, J. Holley, P. P. Chang, S. Paine, D. Kleppner, and T. Ducas. Circular states of atomic hydrogen. *Phys. Rev. A*, 56:1443–1452, 1997.

[100] Harold J. Metcalf and Peter vann der Straten. *Laser Cooling and Trapping*. Springer, 1999.

[101] O. Zobay and B. M. Garraway. Atom trapping and two-dimensional bose-einstein condensates in field-induced adiabatic potentials. *Phys. Rev. A*, 69:023605, 2004.

[102] J. Williams, R. Walser, C. Wieman, J. Cooper, and M. Holland. Achieving steady-state bose-einstein condensation. *Phys. Rev. A*, 57, 1998.

[103] Satyan Bhongale and Murray Holland. Loading a continuous-wave atom laser by optical pumping techniques. *Phys. Rev. A*, 62:043604, 2000.

[104] F. Gerbier, P. Bouyer, and A. Aspect. Quasicontinuous atom laser in the presence of gravity. *Phys. Rev. Lett.*, 86, 2001.

[105] H.M. Wiseman and M.J. Collett. An atom laser based on dark-state cooling. *Physics Letters B*, 202:246–252, 1995.

[106] M. W. Jack, M. Naraschewski, M. J. Collett, and D. F. Walls. Markov approximation for the atomic output coupler. *Phys. Rev. A*, 59:2962, 1999.

[107] G. M. Moy, J. J. Hope, and C. M. Savage. Born and markov approximations for atom lasers. *Phys. Rev. A*, 59, 1999.

[108] J. J. Hope, G. M. Moy, M. J. Collett, and C. M. Savage. Steady-state quantum statistics of a non-markovian atom laser. *Phys. Rev. A*, 61:023603, 2000.

[109] John Jeffers, Peter Horak, Stephen M. Barnett, and Paul M. Radmore. Bound mode of an atom laser. *Phys. Rev. A*, 62:043602, 2000.

[110] M. Naraschewski, A. Schenzle, and H. Wallis. Phase diffusion and the output properties of a cw atom-laser. *Phys. Rev. A*, 56, 1997.

[111] Robert Graham and Dan F. Walls. Theory of strong outcoupling from bose-einstein condensates. *Phys. Rev. A*, 60, 1999.

[112] N. P. Robins, C. M. Savage, J. J. Hope, J. E. Lye, C. S. Fletcher, S. A. Haine, and J. D. Close. Fluctuations and flux: The limits of multistate atom lasers. *Phys. Rev. A*, 69:051602(R), 2004.

[113] N.P. Robins, A. K. Morrison, J.J. Hope, and J. D. Close. Limits to the flux of a continuous atom laser. *Phys. Rev. A*, 72:031606(R), 2005.

[114] Rahul Ramdas Mhaskar. *Toward an Atom Laser: Cold Atoms in a Long, High-gradient Magnetic Guide*. PhD thesis, University of Michigan, 2008.

[115] D. M. Harber, J.M. McGuirk, J. M. Obrecht, and Cornell, E. A. Thermally induced losses in ultra-cold atoms magnetically trapped near room-temperature surfaces. *J. of Low Temp. Phys.*, 133:229–238, 2003.

[116] G. Reinaudi, T. Lahaye, A. Couvert, Z. Wang, and D. Guéry-Odelin. Evaporation of an atomic beam on a material surface. *Phys. Rev. A*, 73:035402, 2006.

[117] G. Reinaudi and D. Guéry-Odelin. Maxwell's demon in the generation of an intense and slow guided beam. *Phys. Rev. A*, 78:015401, 2008.

[118] Christopher Slowe, Laurent Vernac, and Lene Vestergaard Hau. High flux source of cold rubidium atoms. *Rev. Sci. Instrum.*, 76:103101, 2005.

[119] K. Bongs, S. Burger, G. Birkl, K. Sengstock, W. Ertmer, K. Rzążewski, A. Sanpera, and M. Lewenstein. Coherent evolution of bouncing bose-einstein condensates. *Phys. Rev. Lett.*, 83:3577–3580, 1999.

[120] J. Billy, V. Josse, Z. Zuo, W. Guerin, A. Aspect, and P. Bouyer. Guided atom laser: a new tool for guided atom optics. *Ann. Phys. Fr.*, 32:DOI: 10.1051/anphys:2008001, 2007.

[121] C. Gabbanini, S. Gozzini, and A. Lucchesini. Photoionization cross section measurement in a rb vapor cell trap. *Optics Communications*, 141:25–28, 1997.

[122] Daniel A. Steck. Rubidium 87 d line data. *http://steck.us/alkalidata*, revision 2.1.4, 2010.